# HIGH-FIDELITY SIMULATIONS OF A ROTARY BELL ATOMIZER WITH ELECTROHYDRODYNAMIC EFFECTS

by

Venkata Krisshna Pydakula Narayanan

A dissertation submitted in partial fulfillment
of the requirements for the degree

of

Doctor of Philosophy

in

Mechanical Engineering

MONTANA STATE UNIVERSITY
Bozeman, Montana

July 2023

©COPYRIGHT

by

Venkata Krisshna Pydakula Narayanan

2023

All Rights Reserved

DEDICATION




***Knowledge cultivates humility; humility instills worthiness,***
***From worthiness one earns wealth; with wealth one can perform deeds,***

***and so, one finds happiness.***

---

I dedicate this dissertation to
my father, P T Narayanan, who always supports me to pursue my dreams,
my mother, K Kalpana, for all her effort and care to see me succeed,
all the teachers who inspire me to learn and remind me to stay curious,
and all the young minds who teach me to stay spirited, passionate and creative.

# ACKNOWLEDGEMENTS

I am immensely grateful to **Dr. Mark Owkes** for being an amazing mentor. Mark has taken the time to explain complex concepts and guide me through challenging research problems. I have hardly felt that Mark is unreachable even through the pandemic and his year-long sabbatical. In addition to his academic guidance, Mark has cared for my well-being in both personal and professional aspects. I especially thank Mark for providing me with opportunities to attend conferences and present my work. I am grateful to **Ford Motor Company** for their generous funding, which has provided me with the opportunity me to undertake in an industrially driven research project. I would also like to express my gratitude to the **National Science Foundation** for funding my research activity. The material presented in this document is based upon work supported by the under NSF Grant No. 1749779. **Dr. Wanjiao Liu** has been instrumental during my learning phases and had offered me the opportunity to intern at Ford - an experience paramount to my professional growth. I also thank **Dr. Kevin Ellwood** and **Brandon Petrouskie** for their mentorship and guidance. **Dr. Erick Johnson**'s vast knowledge has encouraged me to continue learning. Erick's questions about my research progress are always thought-provoking and have improved the accuracy and applicability of my research activities. Erick does not stop with questions either - he proceeds to provide at least two paths to overcome my challenges. **Dr. Joseph Seymour**'s passion for our understanding of fluids is infectious. Joe has been appreciative and supportive of my work at all stages of research. **Dr. Yaofa Li** has provided valuable feedback on my presentations. He has been instrumental in making

sure that my project serves as a valuable and comprehensive contribution to the scientific community. **Dr. Alan George** taught me fluids in a perspective I had never seen before. I lack sufficient words to thank her **Dr. Sarah Codd** who has genuinely cared for my (and all other students') welfare and academic success. **Dr. Alan George** taught me fluid dynamics in a perspective I had never seen before. I would like to thank my labmates - **Kris, Brian, Ryan, Erin, Clark, Adam, Julian**, and several others. I am grateful for the countless discussions on matters ranging from the best paper clip shape to the rise of artificial intelligence. **Brendan** has been a keystone in my growth as a scientist. Our shared adventures both inside (various technical discussions and outreach events) and outside the lab (rock hunts, fishing, cooking, etc.) have created unforgettable memories that I will cherish for a long time. **Coltran** and **Kenny** from UIT have supported my high-performance computing needs. **Dr. Owkes, Dr. Johnson, George Schaible, Dr. Loribeth Evertz, and Dr. Codd** have helped me grow as a science communicator. **Madhu** and **Toral** have joined me on many adventures. Toral has made me feel safe and loved through many seasons. My two best friends and allies, **Akshay** and **Aravindh**, have been my beacons since we met. My parents and family have supported me and have dedicated so much of their life to me. I have learned to be righteous and sincere in my efforts from my father. I have learned that it is important to be caring and perseverant from my mother. My parents have given nothing short of their best to see me succeed and continue to guide me in making my journey through life a wholesome experience.

TABLE OF CONTENTS

1. INTRODUCTION ..... 1

1.1 Fluid Dynamics and the Use of Computer Simulations ..... 1
1.2 Gas-Liquid Multiphase Flows ..... 2
1.3 Atomization and Breakup ..... 4
1.4 Rotary Bell Atomizers ..... 4
1.5 Electrohydrodynamic Assisted Atomization ..... 6
1.6 Literature Review: Experimental Studies ..... 7
1.7 Literature Review: Numerical Studies ..... 8
1.8 Motivation to Study Electrified Atomization in RBAs ..... 10
1.9 ERBA Problem Setup ..... 12
1.10 Contributions ..... 12
1.11 Dissertation Layout ..... 15

2. MATHEMATICAL FORMULATION ..... 16

2.1 Governing Equations ..... 16
2.1.1 Navier Stokes Equations for Multiphase Flows ..... 16
2.1.2 Electrohydrodynamics ..... 17
2.1.3 Rotating Reference Frame ..... 20
2.1.4 Non-Newtonian Viscosity Relationship ..... 20
2.2 Validation of Physics Modules ..... 22

3. NUMERICAL METHODS ..... 25

3.1 Domain Setup ..... 26
3.2 The Need for e-Mesh ..... 30
3.2.1 e-Mesh Framework ..... 30
3.2.2 e-Mesh Domain Initialization ..... 31
3.2.3 e-Mesh Boundary Conditions ..... 33
3.2.4 Migration Charges to e-Mesh (NS→e Migration) ..... 35
3.2.5 Solving the Electric Poisson Equation on e-Mesh ..... 39
3.2.6 Migrating Electric Potential to NS-Mesh (e→NS Migration) ..... 40
3.2.7 Challenges and Cost With Using E-mesh ..... 43
3.3 Mesh Sensitivity ..... 45
3.3.1 Sensitivity of Droplet Sizes to Mesh Resolution ..... 46
3.3.2 Sensitivity of Droplet Charge Densities to Mesh Resolution ..... 48
3.4 Droplet Ancestry Extraction ..... 49
3.4.1 Insights From Droplet Statistics ..... 49
3.4.2 Method of Extraction ..... 49

TABLE OF CONTENTS – CONTINUED

3.4.3 Storing Statistics in a Database ..... 50
3.4.4 Post-processing the Statistics ..... 51
3.5 Computational Cost ..... 53

4. DEMONSTRATION OF NUMERICAL FRAMEWORK ..... 55

4.1 Liquid Interface ..... 55
4.2 Electric Potential Field ..... 58
4.3 Parameter Study ..... 58
4.4 Examining Non-Dimensional Quantities ..... 61

5. EFFECT OF ELECTRIFYING THE SETUP ..... 63

5.1 Liquid Interface ..... 63
5.2 Spray Characteristics ..... 67
5.3 Atomization Characteristics ..... 68
5.4 Droplet Size and Shape Evolution ..... 71
5.5 Droplet Velocity Statistics ..... 74
5.6 Local Weber Number Analysis ..... 75
5.7 Charge Distribution Statistics ..... 77

6. EFFECT OF SHEAR-THINNING FLOWS ..... 80

6.1 Liquid Interface ..... 80
6.2 Atomization Characteristics ..... 82
6.3 Droplet Size Evolution ..... 84
6.4 Viscosity Characteristics ..... 86

7. CONCLUSIONS AND OUTLOOK ..... 90

7.1 Atomization Characteristics in Rotary Atomization ..... 91
7.2 Impact of Research Work ..... 92
7.3 Future Work ..... 92

REFERENCES CITED ..... 96

APPENDIX ..... 112

APPENDIX A : Appendix ..... 113
A.1 Liquid Surface Profile in a Rotating Tank ..... 113
A.2 Trajectory of an Object in a Rotating Frame ..... 113

# LIST OF TABLES

Table Page

3.1 Standard values of parameters in the ERBA simulations ..... 29

3.2 Simplified *commlist* corresponding to the setup shown in Fig. 3.5 ..... 41

3.3 Mesh sensitivity simulation domain parameters ..... 46

4.1 Non-dimensional numbers used in the ERBA simulations ..... 62

# LIST OF FIGURES

Figure Page

1.1 A rotary bell atomizer in operation. In this image, the shape of the spray cloud is clearly visible above the target surface. Photograph courtesy of RISE Research Institutes of Sweden and Fraunhofer-Chalmers Centre. ..... 6

1.2 A schematic representation of the domain geometry showing the trajectory of the liquid jet (green arrow) and the external body forces acting upon it (not to scale). The device is typically operated at a distance of about 0.25 m from the target surface. ..... 14

2.1 The viscosity-shear rate relationship of automotive paint is approximated well using a modified power law fit. Note the logarithmic scale on the axes. ..... 22

2.2 Validation of centrifugal force: Numerical results of a rotating tank experiment where cases 1, 2, and 3 correspond to rotation rates of 4, 10, and 14 rad/s respectively. The analytical solution of the interface (Eq. 2.18) at various locations is plotted with red circles. The numerically computed liquid interface and liquid bulk are shown as black lines and blue areas respectively. The dashed line represents the axis of rotation for each case. ..... 23

2.3 Validation of Coriolis force: Numerical results of the liquid jet interfaces in a reference frame rotating counter-clockwise about an axis that points out of the 2D plane. The analytical solution (Eq. 2.19) is shown as a superimposed solid line for each case. ..... 24

3.1 A schematic representation of the angle associated with the ejection of liquid from the bell edge, calculated between the axis of rotation and the edge surface. ..... 28

3.2 A schematic representation of e-Mesh and available $\phi$ BCs shown in context with NS-Mesh (not to scale). ..... 31

3.3 A schematic representation of the domain geometry of the numerical problem showing positions and dimensions (not to scale) of NS-Mesh and e-Mesh. ..... 32

LIST OF FIGURES – CONTINUED

Figure Page

3.4 Schematic representation of the grids on NS-Mesh (yellow) and e-Mesh (blue) overlapping. e-Mesh is formulated with a stretched grid to facilitate a higher concentration of cells near the bell edge. The nozzle is shown for reference and is not to scale. ..... 33

3.5 Schematic representation of the overlap of processors between NS-Mesh (green) and e-Mesh (pink). For example, overlapping information exists on processor 3 on the NS-Mesh ($\mathrm{NS}^{\text{ processor } 3}$, highlighted in bright green) and processor 1 on the e-Mesh ($\mathrm{e}^{\text{ processor } 1}$, highlighted in bright pink). The nozzle is shown for reference and is not to scale. ..... 34

3.6 Locations of NS-Mesh boundaries (yellow) with respect to a cell on e-Mesh $\mathrm{e}^{\text{ cell}}$ (blue) ..... 36

3.7 Locations of the boundaries of a cell on NS-Mesh $\mathrm{NS}^{\text{ cell}}$ (yellow) and a cell on e-Mesh $\mathrm{e}^{\text{ cell}}$ (blue) ..... 37

3.8 Electric potential field ($\phi_{\mathrm{e-Mesh}}$) on e-Mesh. The nozzle is shown for reference and is not to scale. ..... 39

3.9 Boundaries of regions occupied by $\mathrm{NS}^{\text{ processor } 3}$ (yellow) and $\mathrm{e}^{\text{ processor } 1}$ (blue). Here, $\text{e-NS}^{\text{ processor } 1-3}_{\text{overlap}} = \textbf{true.}$ ..... 40

3.10 Probability distribution of droplet sizes for varying mesh resolutions. The lines show a log-normal fit of the data. ..... 47

3.11 Volume weighted charge density probability distributions for varying mesh resolutions. Note the logarithmic scale on the y-axis. ..... 48

3.12 Droplet ancestries in the jet shown in Fig. 4.1 represented using the Neo4j graphical database. The colors represent breakup levels 1 (gray), 2 (yellow), 3 (green), 4 (red), 5 (pink) and 6 (blue) breakup events. Lines connect related droplets, i.e., droplets which split from each other. The ligament core (black) is present at the center of the image. Each node contains relevant statistics from the breakup event. ..... 52

LIST OF FIGURES – CONTINUED

Figure Page

3.13 Breakdown of the computational cost of notable modules in the numerical solver. The electric module which handles solutions to the EHD equations presented in Section 2.1.2 is the most expensive part of the solver taking up to 77% of the cost; the transport module which handles multiphase flows and interface tracking accounts for 10% of the cost; the pressure solver accounts for 12% of the cost. ..... 54

4.1 Liquid interface positions of a single jet exiting the edge of the bell at different times as viewed from an $x$-$y$ plane. The nozzle is shown for reference at the top left corner of each image and is not to scale. ..... 56

4.2 Liquid interface positions of six individual jets exiting a serrated bell edge at different times as viewed from an $x$-$z$ plane. The nozzle is rotating clockwise and is shown for reference at the left edge of each image and is not to scale. The simulation domain is outlined by a dashed box. Owing to the periodic boundary conditions along the $z$-axis, an arc along the bell edge spanning six serrations is depicted in this view by stacking the domains in an attempt to vaguely recreate some experimental images [42, 118, 153, 176]..... 57

4.3 The electric potential field and its corresponding contour lines on an $x$-$y$ plane in the domain. The trajectory of the liquid jet is shown graphically as a dashed white line. The electric force vector (blue arrow) that acts on a control volume (blue circle) in this regime is also schematically represented. The bell is shown at the top left corner and is not to scale. ..... 58

4.4 A comparison of snapshots of the liquid interface positions after 200 $\mu$s in the parameter study simulations. The nozzle is shown for reference at the top left corner of each image and is not to scale. ..... 60

5.1 Liquid interface positions in a non-electrified (yellow) and an electrified (violet) jet after exiting the edge of the bell on an $x$-$y$ plane at different times. The nozzle is shown for reference at the top left corner and is not to scale. ..... 65

LIST OF FIGURES – CONTINUED

Figure Page

5.2 Liquid interface positions of six individual non-electrified (yellow) and electrified (violet) jets exiting a clockwise-rotating serrated bell edge (left, not to scale) as viewed at different times from an $x$-$z$ plane. The simulation domain is outlined by a dashed box. Owing to the periodic boundary conditions along the $z$-axis, an arc along the bell edge spanning six serrations is depicted in this view by stacking the domains in an attempt to recreate experimental images available in Shirota et al. [153], Oswald et al. [118], Domnick [42] and Wilson et al. [176]. ..... 66

5.3 Log-normal fit of the near-bell droplet spacing probabilty density. ..... 67

5.4 The total number of droplets in the domain over time. Note the logarithmic scale on the $y$-axis. ..... 69

5.5 The number distribution of droplets that have undergone different breakups levels. ..... 70

5.6 Droplet diameter distribution. Note the logarithmic scale on the $y$-axis. ..... 71

5.7 Mean droplet diameter for each breakup level. ..... 72

5.8 Mean change in droplet diameters for successive breakup levels. Here, breakup level 1 is omitted since it corresponds to breakup from the main ligament core. ..... 73

5.9 Droplet sphericity distribution. ..... 73

5.10 Comparing the mean velocity for different droplet sizes. ..... 74

5.11 Comparing the mean slip velocity for different droplet sizes. ..... 75

5.12 Local Weber number distribution associated with all structures. Note the logarithmic scale on the $y$-axis. ..... 76

5.13 Number distribution of $q$ in liquid structres in the domain. The inital bulk value of $q$ is shown as a dashed line. Note the logarithmic scale on the $y$-axis. ..... 77

5.14 Mean $q$ in liquid structures of different sizes. The inital bulk value of $q$ is shown as a dashed line. ..... 78

LIST OF FIGURES – CONTINUED

Figure Page

5.15 The mean change in $q$ between successive breakup levels. ..... 79

5.16 The mean change in $q$ corresponding to the change in diameter during a breakup event. ..... 79

6.1 Liquid interface positions of a Newtonian (pink) and a non-Newtonian (green) jet at different times as viewed from an $x$-$y$ plane. The nozzle is shown for reference at the top left corner and is not to scale. ..... 81

6.2 The total number of droplets in the domain over time in Newtonian (pink) and non-Newtonian (green) operating conditions in the first 300 $\mu$s of the near-bell atomization simulation. Note the logarithmic scale on the $y$-axis. ..... 82

6.3 The number distribution of droplets that have undergone different breakups levels in Newtonian (pink) and non-Newtonian (green) operating conditions in the first 300 $\mu$s of the near-bell atomization simulation. ..... 83

6.4 Droplet diameter distribution in the simulation. ..... 84

6.5 Mean droplet diameter for each breakup level in the simulation. ..... 85

6.6 Mean change in droplet diameters for successive breakup levels. Here, breakup level 1 is omitted since it corresponds to breakup from the main ligament core. ..... 85

6.7 Liquid viscosity distribution during breakup events in the first 300 $\mu$s of the simulation. ..... 87

6.8 Mean viscosity of the parent droplets for each breakup level. ..... 87

6.9 Mean viscosity of the parent droplets as a function of droplet sizes. ..... 88

6.10 Comparing liquid viscosity for a range of local Weber numbers during breakup events in the first 300 $\mu$s of the simulation. ..... 88

6.11 The mean change in liquid viscosity between successive breakup levels. ..... 89

LIST OF FIGURES – CONTINUED

Figure Page

A.1 Analytical solution of the liquid surface (red) in a tank rotating about the y axis with an angular velocity $\omega$ described mathematically by the function $y$ .....113

# LIST OF ALGORITHMS

Algorithm Page

3.1 NS→e charge density migration algorithm ..... 38

3.2 Calculating index extents for overlap between NS-Mesh and every e $^{\text{processor } n}$ ..... 41

3.3 Calculating index extents for overlap between e-Mesh and every NS $^{\text{processor } n}$ ..... 42

3.4 e→NS electric potential field migration algorithm ..... 44

# NOMENCLATURE

| | |
|---|---|
| $t$ | Time |
| $\mathbf{u}$ | Velocity vector |
| $p$ | Hydrodynamic pressure |
| $g$ | Gravitational acceleration |
| $\rho$ | Density |
| $\gamma$ | Surface tension coefficient |
| $\kappa$ | Local interface curvature |
| $\mu$ | Dynamic viscosity |
| $\varepsilon$ | Electric permittivity |
| $\omega$ | Angular velocity |
| $\mathbf{E}$ | Electric field vector |
| $\mathbf{f}$ | Force vector |
| $\mathbf{n}$ | Interfacial normal vector |
| $\mathbf{r}$ | Radial distance from rotation axis |
| $\phi$ | Electric potential |
| $q$ | Volumetric charge density |
| $\mathbf{J}$ | Current density |
| $\mathcal{D}$ | Diffusion constant |
| $\psi$ | Charge mobility |
| $\mathbb{I}$ | Identity tensor |
| $\Upsilon$ | Viscosity coefficients |
| $\eta$ | Local shear rate |
| $\mathrm{D_{jet}}$ | Jet diameter |
| $\mathrm{Re}_e$ | Electric Reynolds number |
| $\mathrm{Pe}_e$ | Electric Péclet number |
| $\boldsymbol{\sigma}_i^{\mathrm{f}}$ | Viscous stress tensor |
| $\boldsymbol{\sigma}_i^{\mathrm{e}}$ | Maxwell stress tensor |
| $\delta_s$ | Interfacial Dirac-delta function |
| $\tau_q$ | Charge relaxation timescale |
| $\tau_f$ | Fluid advection timescale |
| VF | Liquid volume fraction |
| $\mathcal{S}$ | Structure identification number |
| $\mathcal{L}$ | Liquid identification number |
| $We_{\,\mathrm{local}}$ | Local Weber number |

NOMENCLATURE – CONTINUED

| | |
|---|---|
| BC | Boundary condition |
| CFD | Computational fluid dynamics |
| CPD | Cells per diameter |
| EHD | Electrohydrodynamics |
| ERBA | Electrostatic rotary bell atomizer |
| MPI | Message passing interface |
| PDE | Partial differential equation |
| RBA | Rotary bell atomizer |
| TE | Transfer efficiency |
| VOF | Volume of fluid |
| ACES | Adjustable Curvature Evaluation Scale |
| RPM | Rotations per minute |

# ABSTRACT

Atomizing flows involve the breakup of a liquid into a spray of droplets. These flows play a vital role in various industrial applications such as spray painting and fuel injection. In particular, these processes can have severe impacts especially in automotive paint shops - which can account for up to 50% of the total costs and 80% of the environmental concerns in an automobile manufacturing facility. A device commonly used for painting vehicles is called an electrostatic rotary bell atomizer (ERBA). ERBAs rotate at high speeds while electrically charging the liquid and operating in a background electric field to direct atomized charged droplets towards the target surface. The atomization process directly influences the transfer efficiency (TE) and surface finish quality. Optimal spray parameters used in industry are often obtained from expensive trial-and-error methods.

To overcome these limitations, a computational tool has been developed to simulate three-dimensional near-bell ERBA atomization using a high-fidelity volume-of-fluid transport scheme. Additionally, the solver is equipped with physics modules including centrifugal, Coriolis, electrohydrodynamic (EHD), and shear-thinning viscous force models. The primary objective of this research is to investigate the influence of EHD parameters on near-bell atomization of paint and subsequently improve TE in ERBAs in a cost-effective manner. Using the tools developed, numerical simulations are performed to understand the physics of electrically assisted atomization.

The influence of various operating parameters, such as liquid flow rate, bell rotation rate, liquid charge density, and bell electric potential, on atomization is examined. Results from a comparative study indicate that the electric field accelerates breakup processes and enhances secondary atomization. The droplet velocity, local Weber number and charge density statistics are also analyzed to understand the complex physics in electrically assisted breakup. Additionally, the effect of shear-thinning behavior of the liquid on atomization is also explored. High-fidelity simulations allow for the extraction of breakup statistics which are otherwise challenging to obtain experimentally.

These findings have the potential to drive improvements in the design and operation of ERBAs, leading to enhanced TE and surface finish quality while reducing costs and environmental concerns in automotive paint shops.

# CHAPTER ONE

# INTRODUCTION

## 1.1 Fluid Dynamics and the Use of Computer Simulations

Fluid dynamics is the science describing liquids and gases in motion. This field of science helps us understand a wide range of common and complex scientific phenomena. Some of the pioneering descriptions of how liquids behave can be traced back to ancient Greece around the 3rd century BCE when Archimedes formulated principles related to fluid buoyancy and the displacement of fluids. For centuries, we have described and continually explored the principles governing fluid flow, including the conservation of mass, momentum, and energy, as well as the effects of viscosity and turbulence. Over the past few decades, we have seen a rise in the usage of computers in exploring fluid physics through the development of computational fluid dynamics (CFD) [5, 11]. CFD utilizes the power of modern computers to investigate fluid flow problems. CFD is a powerful tool that can accurately model physical processes using suitable numerical methods and algorithms to solve the corresponding set of equations governing the phenomenon. CFD has allowed us to simulate and analyze complex fluid flows that would otherwise be challenging or impossible to study through traditional experimental methods. In fact, the findings of this dissertation are arguably impossible to obtain using current state-of-the-art experimental techniques. I have personally seen the application of CFD tools in a wide range of scientific and industrial fields including aerospace, chemical, agricultural, energy, medical, environmental, and automotive [99, 108, 142, 150, 178] sectors.

In computer simulations, we have the facility to model difficult geometries, impose

complex boundary conditions, test various fluid properties, and play with a wide range of operating conditions. One of the many strengths of a CFD engineer lies in the process of discretizing the complicated partial differential equations (PDEs) that provide a mathematical description of the physics. Discretization of the PDEs is a procedure that yields a set of (somewhat) simple algebraic equations consisting only of the basic math operations (addition, subtraction, multiplication and division). Another interesting step in CFD is the decomposition of the continuous flow domain into smaller discrete control volumes called computational cells. All properties of the fluid, i.e., scalar quantities such as pressure, charge, and temperature and vector quantities such as velocity, vorticity, and electric field, and tensor quantities, such as the stress tensor are represented as discrete values at either the center or faces of these computational cells.

The process of discretizing the governing equations and the continuous flow domain to yield a set of algebraic equations that can be solved iteratively in each computational cell using numerical methods is the core essence of every CFD algorithm. CFD enables obtaining impeccable insights into the behavior of fluids while, most crucially, reducing costs and time involved with expensive experimental approaches to studying the science of fluid dynamics.

## 1.2 Gas-Liquid Multiphase Flows

Any fluid flow consisting of more than one phase, such as solid-liquid, gas-liquid, and solid-gas flows, within a system is what characterizes multiphase flows - a field of fluid dynamics that has been well studied in the past [17, 19, 26]. Multiphase flows are ubiquitous in our natural world with examples ranging from sediment transport (solid-liquid) [93], bubbly flows (gas-liquid) [98], and dust suspension (solid-gas) [103]. CFD algorithms have also seen continued development towards modeling complex multiphase flows [29, 85, 132, 169, 177]. For example, gas-liquid multiphase CFD models, much like the one used in this project, account for the presence of two or more immiscible fluids, such

as a gas and a liquid, within the computational domain [4]. Each phase can be modeled separately, with their individual properties and interactions considered. Some features of such multiphase solvers include the ability to track the interface to accurately simulate interface dynamics and estimate the local interface curvature to compute the surface tension force. Some multiphase models might also include framework for mass transfer and phase interactions [21, 38]. Several interface tracking methods have been developed [28, 83].

The Volume of Fluid (VOF) method, which has been employed in the project detailed in this dissertation, is based on a Marker-and-cell method, tracks interface motion by storing the volume fraction of each fluid within computational cells [72, 113]. Although this method is mass-conserving, the interface is not readily available and must be computed using appropriate reconstruction methods, which can be complex. In a more fundamental aspect, the modeling of a sharp interface can be challenging and erroneous if its geometric and topological characteristics are not treated carefully [138].

The level set method represents the interface between fluids as an iso-surface of a scalar function that evolves over time to track interface motion [116, 149]. This method is popular due to its simplicity compared to other methods. However, scientists the method has accrued complexities introduced by researchers aiming to address its problems with mass conservation [117].

The front-tracking method explicitly represents interfaces using marker particles and maintains the topology of the interface during the simulation [130, 170]. While the interface normal and curvature are well predicted by the method, the process of fluid coalescence or breakup, which are crucial to some applications of multiphase flows, are not modeled elegantly [25].

## 1.3 Atomization and Breakup

The process of disintegration of bulk liquid into a cloud of droplets/particles, i.e., sprays, in a gaseous medium is termed as atomization. We observe a wide range of sprays in our daily lives including rain, garden sprinklers, shower-heads, hair sprays, and household cleaner sprays. Atomization is a key area of research and development, aimed at improving process efficiency, environmental impact, and enhancing product quality in various industries. Sprays are commonly seen in agricultural [70], healthcare [168], automotive [47], painting [35], food processing [13], cooling [10], fire suppression [136], power generation [15], consumer sprays [173], snowmaking [95], and several other industrial applications [111].

The atomization process is influenced by a wide range of factors - fluid properties (viscosity, surface tension, density), nozzle geometry and design, and operating conditions (ambient temperature, pressure, electric field). Understanding and controlling these factors is essential for achieving the desired droplet size distribution and spray characteristics. CFD models have been developed to simulate atomizing flows [94, 147]. These models aim to provide insights into the breakup and dispersion of liquid jets or films into droplets, which is crucial for the various applications listed above.

## 1.4 Rotary Bell Atomizers

Sprays can be produced in various ways. The breakup of a liquid jet or sheet during the atomization process is often achieved by the impartation of kinetic energy to the liquid. An atomizer is a device used to convert a liquid into a spray of droplets. In general, most atomizers utilize the high relative velocity between the liquid and the ambient gas to induce breakup activity. Liquid is either

1. discharged at a high velocity into a relatively slow-moving stream of gas (pressure [91] or rotary [41] atomizers) or

2. discharged at a low velocity into a relatively fast-moving stream of gas (air-blast atomizers [1]) or

3. disrupted using bubbles (effervescent atomization [158]) or mechanical (ultrasonic atomizers [89]) means to disintegrate the bulk into smaller fragments or

4. manipulated using electric fields in a technique that I will discuss in the next section.

Rotary atomizers are popular in industrial applications due to their simplicity and ease of operation and the desirable atomization characteristics [36, 100, 124] . One such device is called the rotary bell atomizer (RBA) (Fig. 1.1) which is characterized by a bell shaped nozzle [114]. Liquid is injected into the center of a rotating bell. Centrifugal forces cause the liquid to accelerate and form a film that flows radially outward along the inner surface of the bell [45, 88, 164]. The liquid film then exits the edge of the nozzle at a high velocity to form ligaments or sheets which eventually undergo atomization to form a cloud of uniformly sized droplets [58]. Notable desirable features in RBAs are the uniformity in droplet sizes and the ease of control over spray pattern.

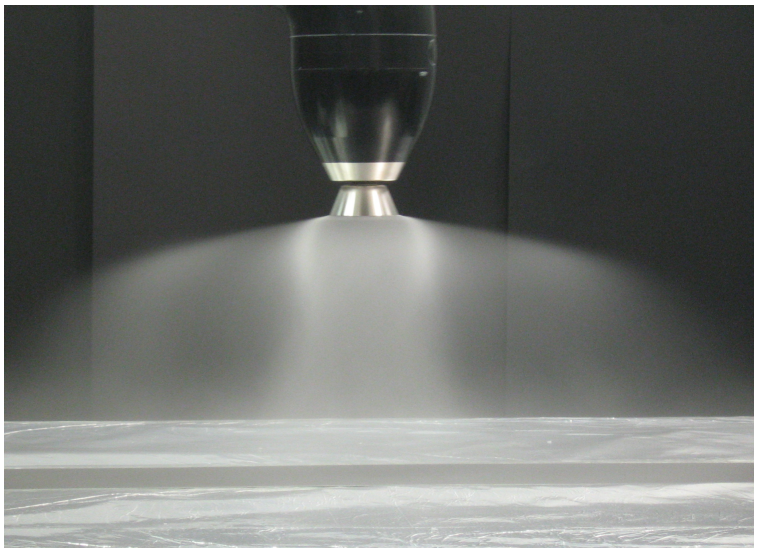


Figure 1.1: A rotary bell atomizer in operation. In this image, the shape of the spray cloud is clearly visible above the target surface. Photograph courtesy of RISE Research Institutes of Sweden and Fraunhofer-Chalmers Centre.

## 1.5 Electrohydrodynamic Assisted Atomization

The fourth method of achieving atomization that I mentioned in the previous section is called electrospraying, where an electric field is used to disintegrate a liquid into charged droplets [27]. These charged droplets can be controlled and manipulated using the electric field [57, 154].

The science behind electrosprays is called electrohydrodynamics (EHD). EHD provides a mathematical description of systems with a significant interaction of fluid dynamics and electrostatics. EHD-assisted atomization has been an increasingly important means of producing liquid droplets that is well-established to offer advantages over other industrial spraying processes [18, 62, 66]. It is commonly used in applications such as inkjet printing [133], mass spectrometry [56], biochemistry [161], microfluidics [16], food technology [6, 14, 61, 82], electrostatic precipitation [179], powder coating [80], fuel injection [155, 182], and biomedicine [46, 50, 54].

Numerical methods that model EHD flows have been developed and improved over the past few decades for various application by several research groups [97, 167]. In EHD simulations, charges can be modeled in the liquid phase on the interface as a fully relaxed surface charge [63, 73, 74, 107] or in the liquid volume as a uniform volumetric charge [154, 172]. Charges can also be modeled in high-fidelity and allowed to relax and redistribute in the liquid phase using appropriate models for charge the migration process [151].

In industrial applications of RBAs, it is common practice to electrically charge the liquid and apply a background electric field to enhance the transfer efficiency of the device [43, 77]. The transfer efficiency, which is an important metric for spraying devices, is the ratio of the mass of the liquid injected into the nozzle to the mass of the liquid that is coated onto the target surface. Atomized droplets, which also carry electric charge, move toward the grounded target surface under the influence of the electric field. An RBA operating in an electrified setup is called an electrostatic rotary bell atomizer (ERBA).

## 1.6 Literature Review: Experimental Studies

The process of atomization in RBAs has been well studied in the past. The following is a summary of a few notable experimental studies that have characterized RBA operation.

A study conducted by Hinze and Milborn [71] have found that the droplet size distribution can be controlled by the rotation rate, nozzle geometry, and the liquid properties. Studies conducted by Corbeels et al. [35] and Rezayat and Farshchi [137] found similar results and included the effects of flow rate, nozzle size and spray angle. Another study presented in Sidawi et al. [156] measured the fraction of area covered by spray droplets for various rotation rates. Mahmoud and Youssef [101] used the phase Doppler particle analyzer method to study the influence of the spinning cup and disk configurations on atomization characteristics. The effect of shaping air, which is the use of a high-speed air stream to shape the spray, on RBAs and ERBAs was investigated by Stevenin et al. [160] and Balachandran

and Bailey [20], respectively. The effect of bell geometry on droplet sizes was examined by Domnick [42]. Sidawi et al. [157] investigated the effect of the size and shape of serrations at the bell edge on atomization quality. Shen et al. [152] investigated the effect of the shear-thinning viscosity of paint on the initial wetting, film formation, and film thickness distribution on the bell. A study conducted by Loch et al. [96] identified the importance of rotation rate and the background electric field to achieve the desired coating properties. A simple computer model was developed from experimental measurements and observations by Yao et al. [181] to predict droplet movement in the spray cloud of rotary atomizers. Fan et al. [53] describes experimental and mathematical methods to measure and calculate paint droplet size, velocity, and charge-to-mass ratio distributions in ERBAs. Several other notable studies have provided valuable insights into the physics of atomization in RBAs [7, 81].

In general, most prior studies have given little or no attention to electric effects on multiphase transport phenomena driving atomization. High-speed cameras and imaging equipment are seldom placed in ERBA setups to prevent electric arcing [65]. For these reasons, experimental studies of the atomization process in ERBAs are limited in detail. Additionally, there is currently no experimental data on the charge distribution in atomized droplets in ERBAs. Although some research has been conducted on the effect of charge density on the surface finish quality [166] and charge distribution in atomized droplets [104] in electrostatic sprays, they have not been studied extensively for charged rotary atomizers.

## 1.7 Literature Review: Numerical Studies

Numerical research studies have been conducted on ERBAs to investigate and optimize their performance in various spray coating applications [33, 102, 174]. The studies focus on understanding the complex fluid dynamics, droplet formation, and electrostatic interactions involved in the atomization process. In Yang [180], an Euler approach is used to simulate the paint flow in the atomizer to determine the paint droplet size and velocities at the

edge. This is followed by an Euler-Lagrange approach to investigate the droplet transfer process, which was the main focus of the work. Recent numerical efforts have characterized the effects of various parameters on droplet trajectories, droplet size distribution, spray pattern, evaporation, and deposition in ERBAs. Pendar and Páscoa [126] implemented a comprehensive three-dimensional Eulerian-Lagrangian model to investigate the electrostatic spray transfer processes in the ERBAs to provide a thorough understanding of the complex airflows around the nozzle and the motion of droplets toward the target surface. Zhu et al. [183] showed that the gas flow greatly influences droplet trajectories near the substrate. While larger droplets are guided towards the target surface by their momentum and electrostatic forces, small droplets continue to be carried away by the air stream. Naoki et al. [110] found that the presence of serrations improve the atomization quality and also that small droplets are likely to be generated when serrations are deeper and more in number. Colbert [34] developed a mathematical model of droplet trajectories generated by ERBAs to predict the deposition rate. In Ellwood et al. [49], the authors present a simplified analysis method for correlating RBA performance on droplet size and coating appearance. In Ray and Henshaw [134], the rate of evaporation of the solvent for a wide range of operating conditions was examined. An interesting approach to modeling the paint application process was conducted by Guettler et al. [64] where they proposed a framework that combines experimental input data, an injection model, and a metamodel-based optimization. Im et al. [78] made a crucial discovery that the spray shape is critically sensitive to the liquid charge density and electric field strength. Pendar and Páscoa [128] observed that electrification significantly impacts the droplet size distribution and the deposition rate.

The studies listed above have shed light on the performance of RBAs and helped optimize the spray characteristics by examining the macroscopic processes of spray cloud formation and paint deposition. However, very little work has been done towards understanding the microscopic phenomena that drive the atomization process to create the

droplets in the spray cloud. The importance of atomization to the performance of this device will be discussed in the next section. Moreover, since the device is often operated in an electric field, it is crucial to investigate the effect of the electric field on the atomization process.

Saye et al. [146] performed high-fidelity numerical simulations of near-bell atomization in RBAs using a hybrid finite difference level-set method and adaptive mesh-refinement while accounting for the non-Newtonian behavior of the fluid. The solver was also equipped with droplet tracking to extract some atomization statistics. Using their tool, several critical statistics which are inaccessible to experimental approaches have provided insight into rotary atomization. The study however lacks the investigation of electrified operation which is commonly seen in industrial applications.

In a different study conducted by Pendar and Páscoa [127], breakup models are employed to predict the atomization process and the droplet size in ERBAs. The models aim to capture the mechanisms responsible for droplet formation and predict the droplet size distribution among other statistics. Pendar and Páscoa [127] have examined the Reitz-Diwakar [135], the Pilch-Erdman [129], and the modified Taylor Analogy Breakup [12] models in their study. While it is not relevant to discuss the details of each model, it is notable that each of these models makes assumptions regarding the underlying physics to form empirical correlations between aerodynamic drag, surface tension, and viscous dissipation on breakup lengths and time scales. While the approximations provided by such models are informative, they may not accurately capture all the complexities of the atomization process.

## 1.8 Motivation to Study Electrified Atomization in RBAs

An important application of ERBAs is in the automotive industry. Almost every car today drives out of a manufacturing facility after being painted by an ERBA in the paint shop. With the world becoming increasingly dependent on automotive means of

transportation and motor vehicle production approaching 100 million units per year [115], automobile manufacturers are looking for ways to minimize production costs. The process of painting vehicles is one of the most expensive aspects of automobile manufacturing, accounting for up to 50% of its total costs [8, 32]. These costs are associated with the energy used in operating and maintaining the HVAC equipment of the painting booth, paint drying, and control of pollutants like volatile organic compounds generated by paint overspray [59]. The overspray leads to significant material waste causing environmental and cost concerns. This makes the paint shop responsible for over 80% of the environmental concerns in a manufacturing facility [60]. Moreover, the global automotive paints and coatings market size was valued at $17.34 bn in 2019 and is expected to be about $26.8 bn by 2027 [131]. Small improvements can result in significant cost savings and waste reduction.

The optimal performance of ERBAs can be improved in the automotive painting industry. Currently, painting with ERBAs often requires over-coating to ensure sufficient finish quality [141]. This has an effective reduction in its overall TE. The operation of ERBAs can be improved to prevent using excess paint to achieve desirable characteristics [141].

Advancing our understanding of the breakup mechanisms in ERBAs can improve the financial and environmental impact of the device in the automotive, agricultural, and pharmaceutical industries. Crucial metrics such as the droplet size uniformity, surface finish quality, TE, deposition thickness, and environmental impact are directly dependent on the atomization process of ERBAs [9, 35, 43]. Currently, expensive trial-and-error experimentation is used to find optimal operating conditions in industrial applications of ERBAs. The physical processes leading to the spray characteristics can be studied computationally using an appropriate CFD solver.

Previous numerical efforts using CFD to simulate ERBA atomizing flows have employed breakup models that limit the accuracy of the droplet size distributions. Moreover, it is crucial to understand the charge distribution in the resulting droplet cloud and its effect on

atomization and surface finish quality. The goal of this work is to address the unanswered questions regarding the effect of the electric field on droplet characteristics in industrial applications of ERBAs.

## 1.9 ERBA Problem Setup

To provide some context, the goal of this research work is to understand the effect of electrified operation on the near-bell atomization characteristics in ERBAs. Since the breakup activity occurs very close to the bell edge, the region of interest in this work extends only a few millimeters from the edge (Fig. 1.2). More details on the domain setup are presented in Chapter 3. I present the following overview of the simulation problem with the intention to guide readers through the layout of the following sections. The mathematical framework presented in the next chapter is motivated by the need to accurately model the relevant physical processes, i.e., multiphase gas-liquid atomizing flows with a focus on the electrohydrodynamics. It is worth noting that the liquid flow is affected by centrifugal and Coriolis (due to the rotating nozzle), electric (due to the charged liquid and the background electric field) and gravity forces after being ejected from the rotating bell cup.

## 1.10 Contributions

Most prior studies have not considered the electric effects on multiphase transport phenomena driving atomization in ERBAs. Experimental studies on ERBA atomization are limited in detail due to the complexities in measuring the atomization characteristics especially pertaining to charge densities in droplets. The numerical studies performed on ERBA atomization have explored the overall spray pattern and deposition rate as a macroscopic phenomenon [96]. Although they include microscopic droplets, they are often inserted as droplets into the domain and do not form after the typical atomization processes.

In this work, high-fidelity simulations of primary and secondary atomization processes with electrohydrodynamic effects are performed. Some of my key contributions include the development of a novel method to compute an accurate electric potential field in the flow domain called e-Mesh (Section 3.2), the implementation of a non-Newtonian viscosity model in the liquid phase (Section 2.1.4) and the implementation of a rotating reference frame into the preexisting framework (Section 2.1.3). Additionally, I have incorporated a droplet ancestry extraction tool to obtain crucial statistics relevant to atomization characteristics which are inaccessible to experimental techniques to provide an in-depth analysis into the physics of atomization in ERBAs (Section 3.4). Using these tools, high-fidelity simulations of the near-bell atomization process is conducted with a focus on understanding the effect of electrified operation on the breakup processes and droplet formation. The details of my work have been documented in a series of published articles [86, 87]. In addition, an article on atomization statistics in ERBAs has been submitted and another article detailing the effect of the shear-thinning behavior of paint on atomization is in preparation.

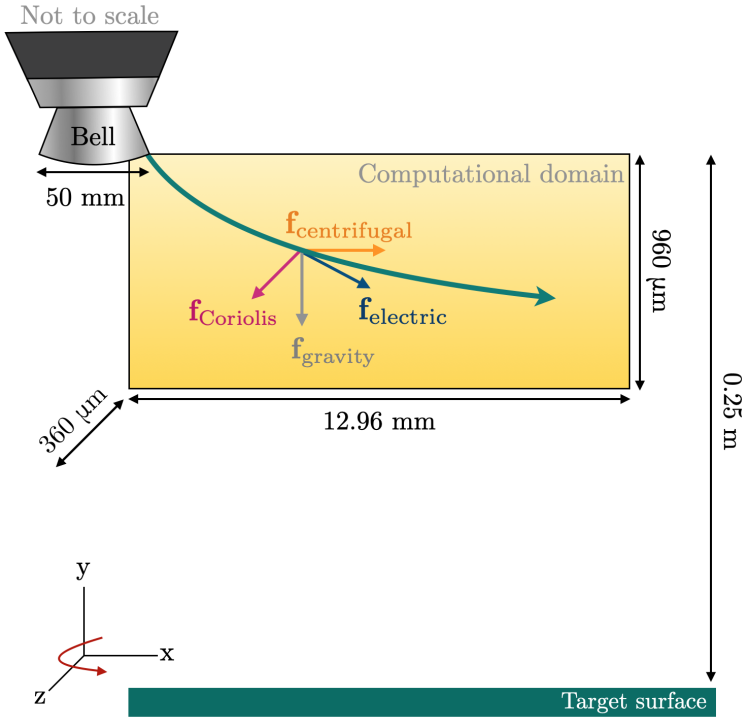



Figure 1.2: A schematic representation of the domain geometry showing the trajectory of the liquid jet (green arrow) and the external body forces acting upon it (not to scale). The device is typically operated at a distance of about 0.25 m from the target surface.

## 1.11 Dissertation Layout

This thesis dissertation is laid out as follows: In Chapter 2, the equations governing all the multiphysics processes relevant to near-bell atomization in ERBAs are reviewed and a mathematical formulation is laid out for the numerical model. In Chapter 3, the numerical methods employed when solving the governing equations are presented. The discussion includes an addition to the flow solver that is essential in computing an accurate electric field in the computational domain, a mesh sensitivity study, and the application of a droplet ancestry statistics extraction tool to obtain previously inaccessible information that will help us understand the physics of atomization. In Chapter 4, the tool built to simulate high-fidelity ERBA flows is demonstrated by presenting some results and conducting a parameter study. Chapter 5 highlights the findings of a comparative study between a non-electrified and an electrified jet and draws inferences regarding the effect of electrification on atomization statistics. Chapter 6 contains a similar comparative study between a Newtonian and a non-Newtonian jet to help isolate and understand the effects of atomization of a shear-thinning fluid. The dissertation is summarized and concluded in Chapter 7 which also contains a comprehensive description of several potential improvements to the setup and methods used in this work.

# CHAPTER TWO

# MATHEMATICAL FORMULATION

This section contains mathematical descriptions of the relevant physical process that are considered to simulate atomization in ERBAs. This section is laid out with particular consideration to the setup described in Section 1.9.

## 2.1 Governing Equations

### 2.1.1 Navier Stokes Equations for Multiphase Flows

For low-Mach number, variable density, multiphase flows, the mass and momentum conservation laws in both phases can be written as

$$\frac{\partial \rho_i}{\partial t} + \nabla \cdot (\rho_i \mathbf{u}_i) = 0, \tag{2.1}$$

$$\frac{\partial \rho_i \mathbf{u}_i}{\partial t} + \nabla \cdot (\rho_i \mathbf{u}_i \otimes \mathbf{u}_i) = -\nabla p_i + \nabla \cdot (\boldsymbol{\sigma}_i^{\mathrm{f}} + \boldsymbol{\sigma}_i^{\mathrm{e}}) + \gamma \kappa \mathbf{n} \delta_s + \mathbf{f}_{\mathrm{external}} \tag{2.2}$$

where $\rho$ is the density, $\mathbf{u}$ is the velocity field vector, $t$ is time, and $p$ is the hydrodynamic pressure. The subscript $i$ denotes the fluid phase (gas or liquid). The term $\gamma \kappa \mathbf{n} \delta_s$ denotes surface tension force, where $\gamma$ is the surface tension coefficient, $\kappa$ is the local curvature of the interface computed using the ACES technique [123], $\mathbf{n}$ is the normal vector to the interface, and $\delta_s$ is a Dirac-delta function that is nonzero only on the interface [120]. The viscous stress tensor $\boldsymbol{\sigma}_i^{\mathrm{f}}$ in Eq. 2.2 is given by

$$\boldsymbol{\sigma}_i^{\mathrm{f}} = \mu_i (\nabla \mathbf{u}_i + \nabla \mathbf{u}_i^{\mathrm{T}}) - \frac{2}{3} \mu_i (\nabla \cdot \mathbf{u}_i) \mathbb{I} \tag{2.3}$$

where $\mu$ is the dynamic viscosity and $\mathbb{I}$ is the identity tensor. These equations form the basis of the fluid dynamics module in this work and further details can be found in Owkes and Desjardins [119, 122] and Desjardins et al. [39, 40]. $\boldsymbol{\sigma}_i^{\mathrm{e}}$ is the Maxwell stress tensor which will be described in the next section. $\mathbf{f}_{\mathrm{external}}$ is a combination of the forces experienced by a fluid element in the system.

$$\mathbf{f}_{\mathrm{external}} = \mathbf{f}_{\mathrm{centrifugal}} + \mathbf{f}_{\mathrm{Coriolis}} + \mathbf{f}_{\mathrm{gravity}} \tag{2.4}$$

### 2.1.2 Electrohydrodynamics

The Maxwell stress tensor $\boldsymbol{\sigma}_i^{\mathrm{e}}$ in Eq. 2.2 is given by

$$\boldsymbol{\sigma}_i^{\mathrm{e}} = \varepsilon_i \mathbf{E}_i \otimes \mathbf{E}_i - \frac{\varepsilon_i}{2}\mathbf{E}_i \cdot \mathbf{E}_i \left(1 - \frac{\rho_i}{\varepsilon_i}\frac{\partial \varepsilon_i}{\partial \rho_i}\right)\mathbb{I} \tag{2.5}$$

where $\mathbf{E}$ is the electric field vector and $\varepsilon$ is the electric permittivity equal to the product of the relative permittivity $\kappa_i$ and the vacuum permittivity space $\varepsilon_0$. Magnetic effects have been ignored since the EHD time scale is several orders of magnitude larger than the magnetic time scale [145] in the atomization process that is of interest here. This electrostatic assumption eliminates the effect of the velocity of the charges (i.e., current) on the electric field thus dictating that the electric field is only influenced by the instantaneous electric charge distribution. The electric force can be expressed as the divergence of the Maxwell stress tensor,

$$\nabla \cdot \boldsymbol{\sigma}_i^{\mathrm{e}} = q_i \mathbf{E}_i - \frac{1}{2}\mathbf{E}_i^2 \nabla \varepsilon_i + \nabla\left(\frac{1}{2}\rho_i \frac{\partial \varepsilon_i}{\partial \rho_i}\mathbf{E}_i^2\right) \tag{2.6}$$

where $q$ is the volumetric electric charge density. The first term on the right-hand side of Eq. 2.6 is the Coulomb (or Lorentz) force. The second and third terms denote the dielectric and the electrostrictive forces respectively, which are only significant in a transient electric field with time scales several orders of magnitude larger than what is encountered in atomization

problems [84].

As the electric field vector is irrotational it can be expressed in terms of the scalar electric potential $\phi$ as

$$\mathbf{E}_i = -\nabla\phi. \tag{2.7}$$

The electric potential Poisson equation describes the relationship between charge density $q_i$ and $\phi$ as

$$-\nabla \cdot (\varepsilon_i \nabla\phi) = q_i. \tag{2.8}$$

The electric Poisson equation is solved using the hypre library of routines for scalable parallel solutions of linear systems [51, 52].

The accumulation of bulk volumetric charge as a surface charge in a thin electric boundary layer much smaller than the hydrodynamic boundary layer is a commonly made assumption in charged jet simulations [171, 175]. The electric charge has previously been modeled in two ways: either a constant bulk volumetric charge or a fully relaxed surface charge. According to the classic leaky dielectric model [105, 145, 165] that is commonly used to describe the effects of electric charge in dielectric liquids, the fundamental underlying assumption is that bulk volumetric electric charge has sufficient time to fully relax to a surface charge. However, for atomizing flows the advection time scale is similar to the charge relaxation time scale and a fully relaxed charge assumption is invalid. The charge relaxation time $\tau_q$ represents the time required for volumetric charge $q_l$ to relax to the surface [37, 84]. The fluid advection timescale $\tau_f$ is a characteristic time for a fluid element to move across a relevant length scale $L_0$. The ratio of the two time scales called the electric Reynolds number $\mathrm{Re}_e$ was formulated in Stuetzer [162] as

$$\tau_q = \frac{\varepsilon_l}{\psi_l \; q_l}, \tag{2.9}$$

$$\tau_f = \frac{L_0}{\mathbf{u}}, \tag{2.10}$$

$$\mathrm{Re}_e = \frac{\tau_q}{\tau_f} \tag{2.11}$$

where values of the quantities that correspond to typical automotive paints and RBA operations listed in Table 3.1 yield a value of $\mathrm{Re}_e$ approximately equal to 8.93. This suggests that the advection and charge relaxation timescales are comparable in this application. The above time scale analysis highlights the necessity to model the process of charge relaxation by migration and diffusion in addition to advection with the fluid velocity. The common assumption of charges to be accumulated on the surface disallows the charge migration dynamics and limits the accuracy of the droplet charge distribution after atomization. In this work, we assume a constant bulk volumetric charge at the injector and allow charges to relax as the jet propagates through the domain. Charge transport is described by the conservation equation

$$\frac{\partial q_i}{\partial t} + \nabla \cdot \mathbf{J}_i = 0 \tag{2.12}$$

where the current density $\mathbf{J}_i$ is formulated as [106, 172]

$$\mathbf{J}_i = q_i \mathbf{u}_i + q_i \psi_i \mathbf{E}_i - \mathcal{D}_i \nabla q_i \tag{2.13}$$

where $\psi_i$ is the charge mobility coefficient and $\mathcal{D}_i$ is the molecular diffusivity. The three terms that contribute to the current density can be described as advection due to the velocity field, advection due to the electrical velocity, and diffusion.

In summary, the charge density field ($q$) and boundary conditions (BCs) in electric potential are used to obtain the electric potential field ($\phi$) using Eq. 2.8. The electric field

($\mathbf{E}$) is then obtained using Eq. 2.7 after which Eq. 2.6 allows for the calculation of the Coulomb/electric force ($\mathbf{f}_{\text{electric}}$) on the charged fluid. More details on the equations involved in the formulation of the EHD module can be found in Sheehy and Owkes [151].

### 2.1.3 Rotating Reference Frame

In an ERBA undergoing ligament breakup mode, each ligament exiting the serrated bell edge behaves similarly with statistically similar droplet size distribution and charge transport behavior. Therefore, a single ligament ejected from the bell edge is the focus of the numerical simulations. The reference frame is attached to the rotating nozzle and ligament.

To account for the rotating nozzle and the consequent forces, equations that describe the rotating reference frame are included in the model. This subjects the liquid to centrifugal and Coriolis forces which can be formulated as

$$\mathbf{f}_{\text{centrifugal}} = -\rho_i \boldsymbol{\omega} \times (\boldsymbol{\omega} \times \mathbf{r}) \tag{2.14}$$

$$\mathbf{f}_{\text{Coriolis}} = -2\rho_i \boldsymbol{\omega} \times \mathbf{u}_i \tag{2.15}$$

where $\boldsymbol{\omega}$ is the angular velocity and $\mathbf{r}$ is the radial distance from the axis of rotation.

### 2.1.4 Non-Newtonian Viscosity Relationship

Most modern automotive paints are non-Newtonian in nature. In particular, they exhibit shear-thinning or pseudoplastic behavior. There are a number of well-established shear-thinning viscosity models. The power law fluid model predicts a boundless shear-thinning viscosity for high shear rates. The Carreau model first proposed by Pierre Carreau and the Cross fluid model both predict the viscosity in a liquid that has both a low and high viscosity limit at high and low shear rates, respectively. The Herschel-Bulkley fluid model limits the lowest viscosity attainable by the liquid at infinitely high shear rates [69]. In this work, however, the dynamic viscosity of a liquid ($\mu_l$) subject to a local shear rate

($\eta$) is formulated using a modified power law. The modified power law model is a suitable approximation for automotive paints as the empirical viscosity-shear rate data provided by PPG Industries shows a similar behavior (Figure 2.1). Although a Herschel-Bulkley model would have also been suitable, the unavailability of the yield stress of the liquid would have required making an arbitrary assumption for the purpose of a fit. According to the modified power law, liquid viscosity is related to the local shear rate as

$$\mu_l = \Upsilon_1 \cdot \eta^{\,(\Upsilon_2 - 1)} + \Upsilon_0 \tag{2.16}$$

where $\Upsilon_0$, $\Upsilon_1$, and $\Upsilon_2$ are viscosity coefficients pertaining to the power law. The modification lies in the addition of the term $\Upsilon_0$ which is absent in a traditional power law equation. The coefficients are obtained by applying a fitting function on empirical viscosity-shear rate data. Using empirical data, the set of values of the viscosity coefficients that models its shear-thinning behavior appropriately have been determined and are listed in Table 3.1.

Figure 2.1 shows the viscosity-shear rate relationship of the automotive paint modeled in this study and compares it with the modified power law fit which is shown to be an acceptable approximation for this work. For clarity, the value of viscosity in interfacial cells ($\mu_{\text{avg}}$) is harmonically averaged as

$$\mu_{\text{avg}} = \frac{\mu_l \cdot \mu_g}{\mu_g \cdot \text{VF} + \mu_l \cdot (1 - \text{VF})} \tag{2.17}$$

where $\mu_g$ is the dynamic viscosity of the gas phase and VF is the liquid volume fraction in the cell. The harmonic averaging method was provided in Patankar [125] and has been accepted as a reasonable approximation for several decades [4].

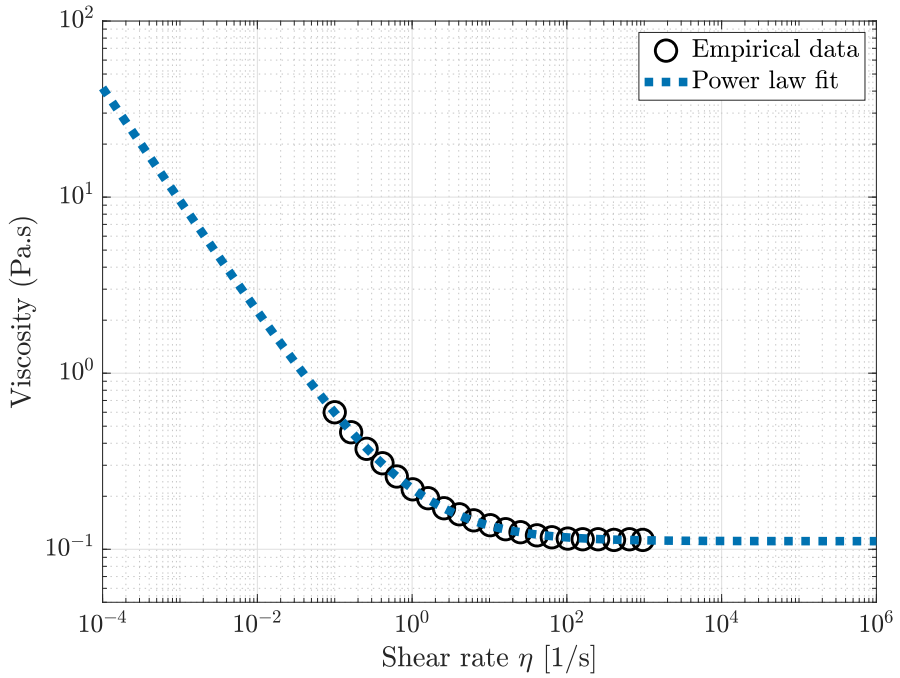



Figure 2.1: The viscosity-shear rate relationship of automotive paint is approximated well using a modified power law fit. Note the logarithmic scale on the axes.

## 2.2 Validation of Physics Modules

The EHD module has seen continued development and validation efforts have been presented in [151]. To validate the implementation of centrifugal force (described in Section 2.1.3), numerical experiments of a rotating tank configuration are conducted. The solution for the steady-state interface profile $h(x)$ of a liquid in a rotating tank is analytically derived as

$$h(x) = h_0 + \frac{1}{2g}\left(\boldsymbol{\omega} x\right)^2 \tag{2.18}$$

where $h_0$ is the height of the liquid at the axis of rotation and $g$ is the gravitational acceleration [90]. The derivation of this analytical solution is provided in Section A.1. Numerical results show excellent agreement with the analytical solution for varying rotation

rates (Fig. 2.2).

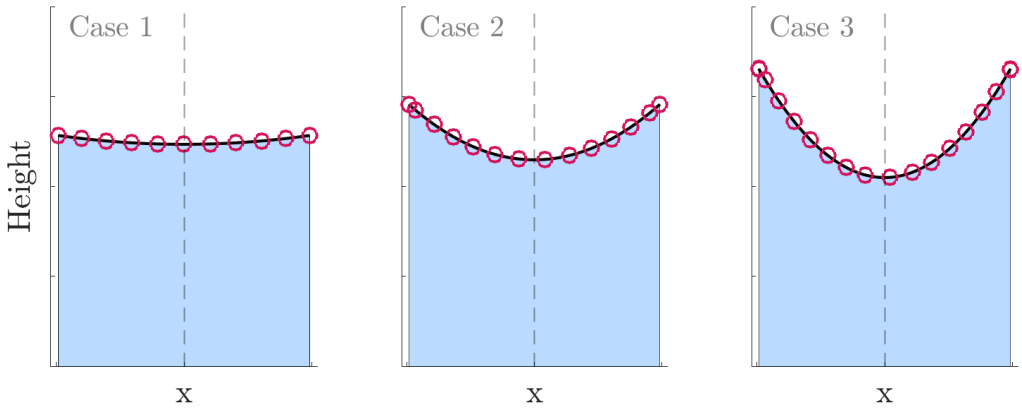



Figure 2.2: Validation of centrifugal force: Numerical results of a rotating tank experiment where cases 1, 2, and 3 correspond to rotation rates of 4, 10, and 14 rad/s respectively. The analytical solution of the interface (Eq. 2.18) at various locations is plotted with red circles. The numerically computed liquid interface and liquid bulk are shown as black lines and blue areas respectively. The dashed line represents the axis of rotation for each case.

The numerical implementation of the Coriolis force is tested by simulating a liquid jet in a rotating frame. The path of an object experiencing the centrifugal and Coriolis forces follows a circle with a growing radius, i.e., a spiral. The analytical solution for the position of the object $(x, y)$ at a given time $t$ is obtained as

$$\begin{aligned} x(t) &= (x_0 + v_{x0}t)\cos(\boldsymbol{\omega} t) + t\,(v_{y0} + \boldsymbol{\omega} x_0)\sin(\boldsymbol{\omega} t) \\ y(t) &= -(x_0 + v_{x0}t)\sin(\boldsymbol{\omega} t) + t\,(v_{y0} + \boldsymbol{\omega} x_0)\cos(\boldsymbol{\omega} t) \end{aligned} \tag{2.19}$$

where $v_{x0}$ and $v_{y0}$ are the $x$ and $y$ components of the initial velocity of the jet and $x_0$ is the position of the jet at $t = 0$. The derivation of this solution is also provided in Section A.2. This solution is derived for a rigid point-like object with its all mass concentrated at its center. Liquid jets, however, are not point-like approximations and include effects of viscosity and surface tension. Despite these challenges, satisfactory results are obtained for the the effect of the Coriolis force on liquid jets in a rotating reference frame. Numerically simulated liquid

jets follow the analytically predicted trajectory for varying rotation rates (Fig. 2.3).

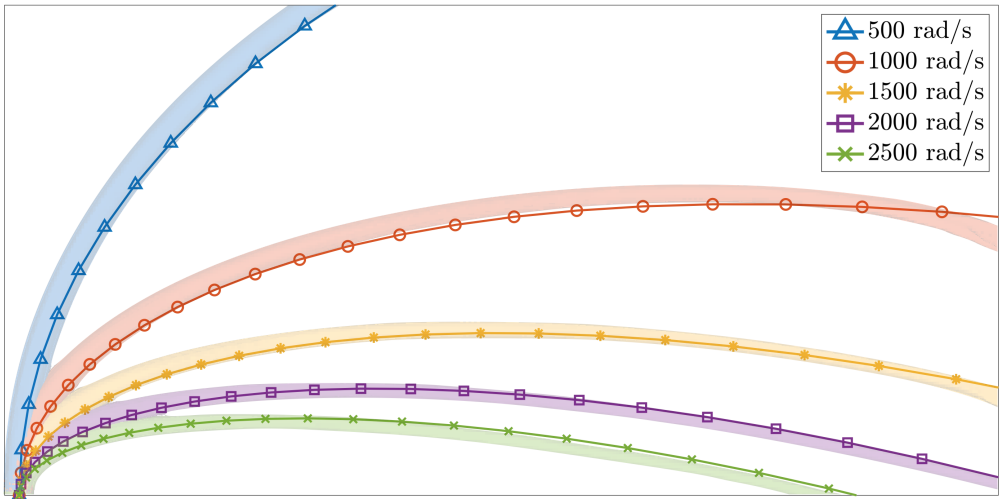



Figure 2.3: Validation of Coriolis force: Numerical results of the liquid jet interfaces in a reference frame rotating counter-clockwise about an axis that points out of the 2D plane. The analytical solution (Eq. 2.19) is shown as a superimposed solid line for each case.

# CHAPTER THREE

# NUMERICAL METHODS

The numerical setup is designed based on the various physics modules discussed in Section 2.1. The modules have been implemented within a code called NGA - a high-order, fully conservative, variable density, low Mach number Navier-Stokes solver that contains various multi-physics modules implemented in parallel using message passing interface (MPI). The formulation discretely conserves mass and momentum in a periodic domain. NGA uses a conservative unsplit geometric volume-of-fluid (VOF) scheme as described in the works of Blanquart et al. [24], Desjardins et al. [39, 40] and Owkes and Desjardins [119, 120, 121, 122]. NGA has been developed by several groups to solve multiphase EHD flows, details of which can be found in Van Poppel et al. [172], Sheehy and Owkes [151].

The finite difference operators arising from discretizing the governing equations (Section 2.1) are formulated using a conservative finite difference scheme [39, 119]. Consistent and conservative transport near the interface is performed using the unsplit geometric VOF scheme [122]. The interface curvature ($\kappa$) used in the surface tension computation (Eqn. 2.2) is calculated using the Adjustable Curvature Evaluation Scale (ACES) scheme described in [123]. The pressure Poisson equation is solved using the ghost fluid method [55] and the blackbox multigrid technique [79]. The electric Poisson equation (Eq. 2.8) is solved using the LGMRES method [140] included in the HYPRE library of linear algebra solvers and preconditioners [76].

In this chapter, the domain setup is described in Section **??**. A method to obtain accurate electric potential fields on the flow domain is presented in Section 3.2. Section 3.3 contains the details of a mesh sensitivity study that was performed to identify a suitable mesh resolution to capture the relevant physical processes. The implementation of a novel tool that

extracts droplet ancestry statistics to gain more insights into the physics of atomization is presented in Section 3.4. Finally, the computational cost of the simulation is briefly discussed in Section 3.5.

## 3.1 Domain Setup

The domain is sized in such a way that it is large enough to capture most of the breakup activity occurring near the bell edge. It has dimensions of 12.96 mm $\times$ 960 $\mu$m $\times$ 360 $\mu$m. It is represented schematically in Fig. 1.2. In this work, a bell of radius 25 mm is studied. Some ERBAs are equipped with serrations present at the edge of the bell which causes the fluid to be ejected as thin jets. In the absence of these serrations, the fluid forms liquid sheets on the inner surface of the bell. These liquid sheets may be subject to interfacial instability and form periodic ligaments at the edge of the bell or break up in sheet mode depending on the operating conditions. In this work, a single liquid jet exiting one of the serrations is simulated. Appropriate boundary conditions are imposed to inform every jet of neighboring flows from adjacent serrations which will be discussed in the following paragraphs.

The bell simulated in this work is equipped with 418 serrations along its edge, each of which is 375 $\mu$m wide. While the liquid profile in a serration does not have a circular cross-section, a 60 $\mu$m diameter jet that exits the bell edge is approximated for a bell operating at 40 kRPM [44]. For a nozzle flow rate of 200 mL/min, the flow rate through each serration is $7.96\times10^{-9}$ m$^3$/s. In the numerical setup, the jet is injected into the domain from the top wall with initial velocity components that correspond to an edge angle of 25° through an elliptical cross section. Breakup is induced by imparting velocity modulations to the inflow. The inflow velocity ($\mathbf{u}_{\text{inflow}}$) is modulated by adding sinusoidal perturbations at a superposition of three (40, 50, and 60 kHz) frequencies ($\boldsymbol{\omega}$) at an amplitude $\tilde{A}$ which is 9% of its original velocity ($\mathbf{u}$) (Eq. 3.1). Several combinations of frequencies were tested and the particular combination chosen produces a perturbation in the jet that is small enough in magnitude

that it does not largely affect the trajectory near the inflow. The goal of imparting these velocity modulations is to replicate natural perturbations that would appear in experimental setups due to instrument vibrations or fluctuations in film thickness that act as sources of minor modifications to the flow [148, 159].

$$\mathbf{u}_{\text{inflow}} = \mathbf{u} + \sum_{n=1}^{3} \tilde{A} \ \sin\left(2\pi\boldsymbol{\omega}_n t\right). \tag{3.1}$$

In ERBAs, the bell edge plane is angled away from the plane perpendicular to the axis of rotation (Fig. 3.1). The axis of rotation, which is the center of the bell, is located one radial length away (in the $-x$ direction) from the inflow.

A magnitude of 2.879 C/m$^3$ for liquid charging is applicable to ERBAs used in industrial paint shops [48, 128]. While the charging mode in practice does not typically yield a uniform bulk initial charge distribution, such a case is assumed for simplicity. Improvements towards more accurate modeling of liquid charging are discussed in the future works section in Section 7.3. It is worth noting that the charges are still free to redistribute by the processes of advection, diffusion, and migration as dictated by Eqn. 2.12 once the liquid is in the flow domain.

The top boundary is a wall that allows slip velocity and the left boundary is a no-flux wall. The bottom and right boundaries are convective outflows. Periodic BCs are imposed on the front and back walls. In addition to mass, momentum, and charge being transported across the periodic $z$ boundaries, the electric field is also computed with the effect of the periodicity. This means that at any instance, the single jet simulated in the computational domain is solved with full consideration of its nearest neighboring jets.

It is worth noting that a Cartesian grid is employed in this work for the following reason - despite the serrations lying along the perimeter of a bell cup which is curved, the focus of this simulation is a thin slice (360 $\mu$m wide) while the domain length along the radial

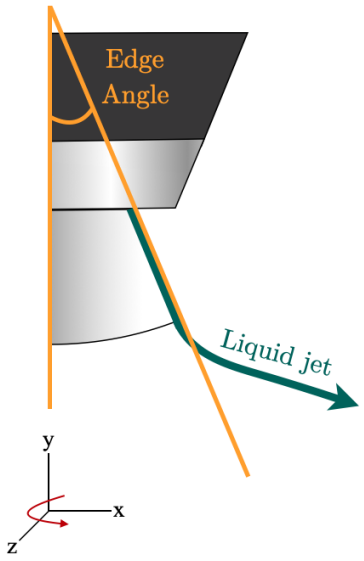



Figure 3.1: A schematic representation of the angle associated with the ejection of liquid from the bell edge, calculated between the axis of rotation and the edge surface.

direction (12.96 mm) which is about half the diameter of the bell cup. This means that the curvature of the bell is significant enough to consider using a cylindrical coordinate system and grid. An implication of using a Cartesian grid and applying periodic BCs along the $z$ boundaries means that the jets (and the resulting liquid structures) interact more then they should at the downstream part of the domain. This is a shortcoming in the current formulation and has been addressed in Section 7.3.

Table 3.1 contains a list of parameter values used in simulations.

Table 3.1: Standard values of parameters in the ERBA simulations

| **Property** | **Symbol** | **Value** | **Unit** |
|---|---|---|---|
| Bell rotation rate | $\omega$ | $40\times10^{3}$ | RPM |
| Bell radius | $R_{bell}$ | 0.025 | m |
| Edge angle | - | 25 | deg |
| Inlet jet diameter | $D_{jet}$ | $60\times10^{-6}$ | m |
| Liq. flow rate | - | $7.96\times10^{-9}$ | $m^3/s$ |
| Liq. viscosity (Newtonian) | $\mu_l$ | 0.1 | Pa.s |
| Liq. density | $\rho_l$ | 1000 | $kg/m^3$ |
| Surface tension | $\gamma$ | 0.03 | N/m |
| Bell electric potential | $V_{bell}$ | $80\times10^{3}$ | V |
| Liq. charge density | $q_l$ | 2.879 | $C/m^3$ |
| Liq. rel. permittivity | $\kappa_l$ | 50 | - |
| Liq. diffusion constant | $\mathcal{D}_l$ | $2\times10^{-6}$ | $m^2/s$ |
| Liq. charge mobility | $\psi_l$ | $1.79\times10^{-8}$ | $m^2/V.s$ |
| Liq. viscosity coefficients | $\gamma_0$ | 0.11 | Pa.s |
| | $\gamma_1$ | 0.11 | Pa.s |
| | $\gamma_2$ | 0.36 | - |

## 3.2 The Need for e-Mesh

An addition to the EHD module of flow solver was developed for this project and mainly involves using a domain called e-Mesh. e-Mesh is much larger than the flow-solver domain, henceforth called the NS-Mesh, where the Navier-Stokes equations described in Section 2.1.1 are solved. Since our interest lies in primary and secondary atomization, NS-Mesh lies at the edge of the bell and extends only a few millimeters outside of it. NS-Mesh requires a well-defined electric potential field ($\phi$) to obtain the electric field ($\mathbf{E}$) and solve the EHD equations. $\phi$ is solved using appropriate boundary conditions (BCs) on NS-Mesh. However, Fig. 3.2 highlights that $\phi$ is well defined (labeled Dirichlet) with values readily available only at the nozzle (bell electric potential) and at the target surface (grounded) but unavailable at the boundaries of NS-Mesh. Instead of assuming values of $\phi$ BCs on NS-Mesh, a new domain called e-Mesh that spans between regions of well-defined $\phi$ is initialized and used to obtain accurate $\phi$ BCs on NS-Mesh. e-Mesh is about 4000 times larger than NS-Mesh, i.e., the region of interest in this project lies in about 0.0125% of the volume of e-Mesh. Making NS-Mesh this large would require significantly more computational resources to solve the fluid dynamics far from the bell edge. Such an approach would impractical and unfeasible. The breakup activity and charge transport within the liquid, which are the processes of interest in this work, are already completed within the NS-Mesh domain. In this way, e-Mesh is used exclusively as an electric potential solver.

### 3.2.1 e-Mesh Framework

There are several steps involved in the employment of e-Mesh to obtain an electric potential field. A well defined charge density field ($q$) is required to solve for $\phi$ on e-Mesh ($\phi_{\mathrm{e-Mesh}}$). After obtaining $\phi_{\mathrm{e-Mesh}}$, the values need to be interpolated from e-Mesh to cells that lie on the boundaries of NS-Mesh to be applied as BCs to compute $\phi$ on NS-Mesh. The

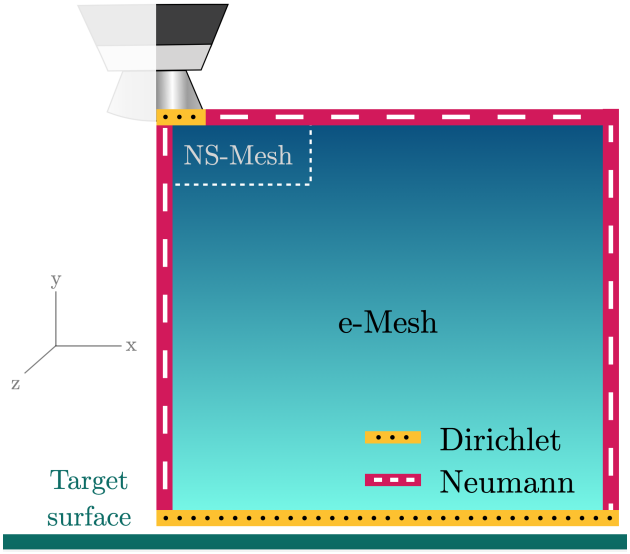



Figure 3.2: A schematic representation of e-Mesh and available $\phi$ BCs shown in context with NS-Mesh (not to scale).

step-wise process can be listed as follows -

1. Initialize the e-Mesh domain geometry.
2. Impose boundary conditions on e-Mesh.
3. Migrate charge density $q$ from NS-Mesh to e-Mesh.
4. Solve the electric Poisson equation on e-Mesh.
5. Migrate electric potential from e-Mesh to NS-Mesh.

Steps 1 - 2 are performed once at the beginning of the simulation and steps 3 - 5 are performed every time the electric potential BCs are updated in NS-Mesh. Details of each step are provided below.

### 3.2.2 e-Mesh Domain Initialization

When operating in industrial applications, the bell is typically about 0.25 m away from the surface. This makes e-Mesh 0.25 m long in the $y$-direction. e-Mesh extends to a distance of about 0.2 m away from the axis along the $x$-direction, $\phi$ contour lines are measured to be parallel to the surface. This distance would allow for Neumann BCs on the right wall.

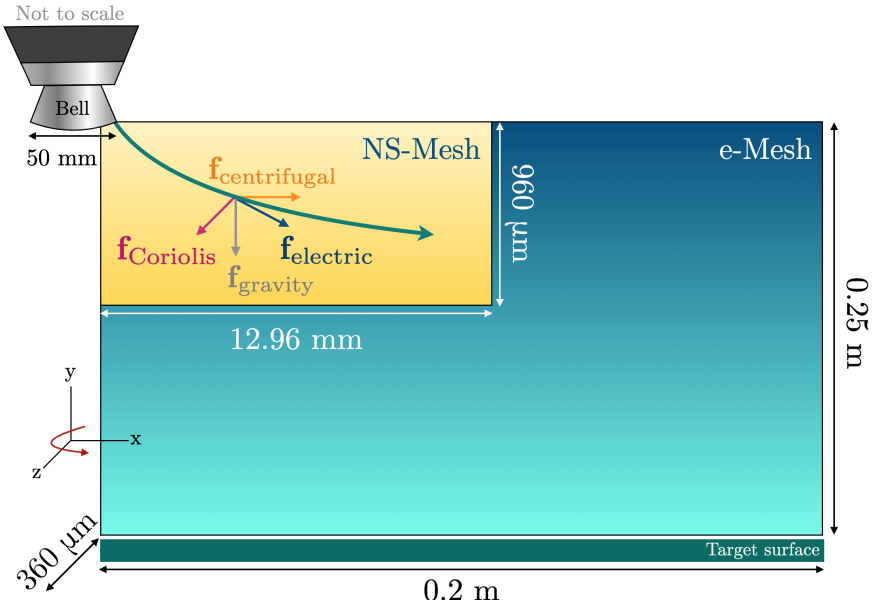



Figure 3.3: A schematic representation of the domain geometry of the numerical problem showing positions and dimensions (not to scale) of NS-Mesh and e-Mesh.

e-Mesh and NS-Mesh are equal in length in the $z$-direction, allowing for periodic BCs on the $z+$ and $z-$ walls. Therefore, e-Mesh, which spans from the bell edge to the target surface, has dimensions of 0.2 m $\times$ 0.25 m $\times$ 360 $\mu$m (Fig. 3.3).

e-Mesh has a stretched grid along the $x$ and $y$ directions to facilitate a higher concentration of cells where it coincides with NS-Mesh near the bell edge. Grid points along $x$ and $y$ directions on e-Mesh are placed according to a Gaussian function such that they are stretched around the bell edge. Grid points along $z$ are coincident in both meshes. As a result, nodes and cells on both the meshes are not coincident. A schematic representation of the stretched grid is shown in Fig. 3.4. NS-Mesh has a uniform grid consisting of cubic cells and e-Mesh has a non-uniform grid made up of cuboidal cells. NGA, which is the code that performs numerical calculations, is a code written with the ability to be run on multiple processors using message passing interface (MPI). It is common practice to distribute the computational load by allowing each processor to solve only a part of the entire domain. As a

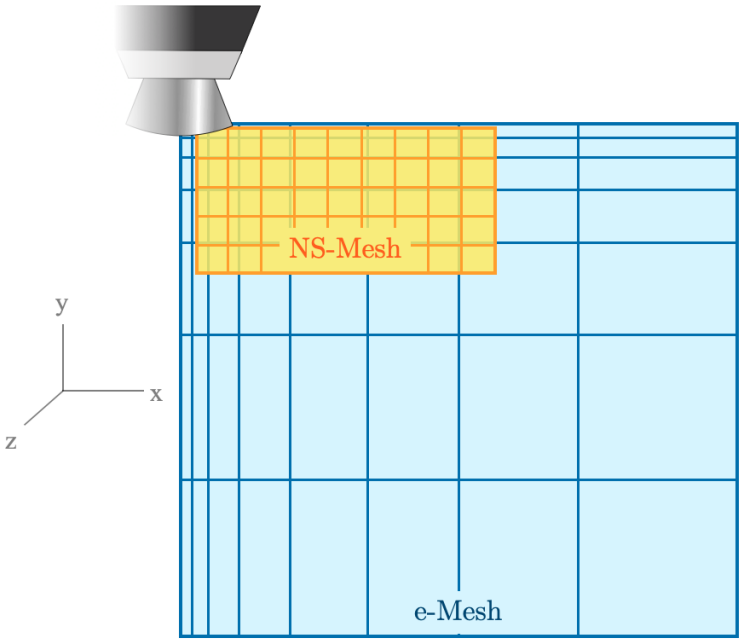



Figure 3.4: Schematic representation of the grids on NS-Mesh (yellow) and e-Mesh (blue) overlapping. e-Mesh is formulated with a stretched grid to facilitate a higher concentration of cells near the bell edge. The nozzle is shown for reference and is not to scale.

result, NS-Mesh and e-Mesh are both split into smaller sub-domains, one for each processor. The processor domains on e-Mesh are decomposed in such a way that the number of cells handled by each processor is balanced. This yields a domain decomposition that also looks non-uniform as shown in Fig. 3.5.

The discretization of the governing equations describing EHD flows (Section 2.1.2) yield a set of several finite different operations. It is somewhat straight-forward to perform the operations on the uniform grid on NS-Mesh. However, the finite difference operations on e-Mesh, which has a non-uniform grid with non-constant intervals, are obtained as described in Sundqvist and Veronis [163].

### 3.2.3 e-Mesh Boundary Conditions

A Dirichlet BC corresponding to the value of the bell electric potential is imposed on the section of the top boundary of e-Mesh that overlaps the nozzle. A zero potential boundary

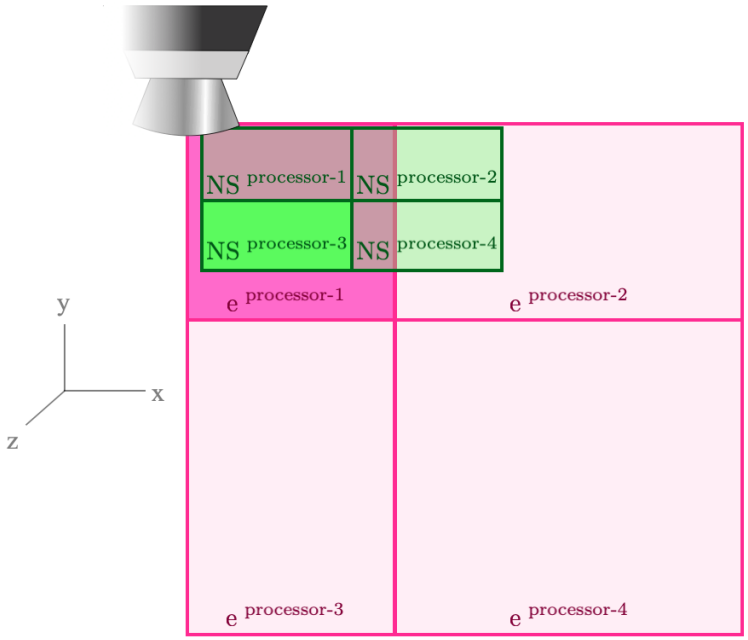



Figure 3.5: Schematic representation of the overlap of processors between NS-Mesh (green) and e-Mesh (pink). For example, overlapping information exists on processor 3 on the NS-Mesh (NS $^{\text{processor 3}}$, highlighted in bright green) and processor 1 on the e-Mesh (e $^{\text{processor 1}}$, highlighted in bright pink). The nozzle is shown for reference and is not to scale.

condition is imposed on the bottom boundary which represents the grounded target surface. Periodic BCs for potential are imposed on the $z^+$ and $z^-$ boundaries of e-Mesh and Neumann BCs for potential are imposed on all its remaining boundaries. The right boundary ($x^+$) has been chosen in such a way that it is far enough away from the axis of rotation that the electric potential field lines are parallel to the target surface, allowing for a Neumann BC to be imposed. A schematic representation of the BCs applied on each boundary is shown in Fig. 3.2.

### 3.2.4 Migration Charges to e-Mesh (NS→e Migration)

As mentioned, the goal of e-Mesh is to obtain an electric potential field that can be used to impose well-informed BCs on the boundaries of NS-Mesh. In order to obtain an electric potential field on e-Mesh, the charge density field is required to be migrated from NS-Mesh. There are two steps involved in the migration of charge density values from NS-Mesh to e-Mesh (NS-e migration) - 1) conservative interpolation and 2) inter-processor communication. Interpolation of information is necessary due to the non-coincidence of cells between NS-Mesh and e-Mesh, outlined schematically in Fig. 3.4.

For interpolation, every cell on e-Mesh ($\mathrm{e}^{\,\mathrm{cell}}$) is flagged by whether it shares volume with NS-Mesh and requires to participate in the migration process by comparing its spatial extents to the spatial extents of NS-Mesh -

$$\begin{aligned}
&\textbf{if } [(\mathrm{e}^{\,\mathrm{cell}}_{\mathrm{x-}} \geq \mathrm{NS}^{\,\mathrm{mesh}}_{\mathrm{x-}} \textbf{ and } \mathrm{e}^{\,\mathrm{cell}}_{\mathrm{x-}} \leq \mathrm{NS}^{\,\mathrm{mesh}}_{\mathrm{x+}}) \textbf{ or } (\mathrm{e}^{\,\mathrm{cell}}_{\mathrm{x+}} \leq \mathrm{NS}^{\,\mathrm{mesh}}_{\mathrm{x+}} \textbf{ and } \mathrm{e}^{\,\mathrm{cell}}_{\mathrm{x+}} \geq \mathrm{NS}^{\,\mathrm{mesh}}_{\mathrm{x-}})] \\
&\textbf{and } [(\mathrm{e}^{\,\mathrm{cell}}_{\mathrm{y-}} \geq \mathrm{NS}^{\,\mathrm{mesh}}_{\mathrm{y-}} \textbf{ and } \mathrm{e}^{\,\mathrm{cell}}_{\mathrm{y-}} \leq \mathrm{NS}^{\,\mathrm{mesh}}_{\mathrm{y+}}) \textbf{ or } (\mathrm{e}^{\,\mathrm{cell}}_{\mathrm{y+}} \leq \mathrm{NS}^{\,\mathrm{mesh}}_{\mathrm{y+}} \textbf{ and } \mathrm{e}^{\,\mathrm{cell}}_{\mathrm{y+}} \geq \mathrm{NS}^{\,\mathrm{mesh}}_{\mathrm{y-}})] \\
&\textbf{and } [(\mathrm{e}^{\,\mathrm{cell}}_{\mathrm{z-}} \geq \mathrm{NS}^{\,\mathrm{mesh}}_{\mathrm{z-}} \textbf{ and } \mathrm{e}^{\,\mathrm{cell}}_{\mathrm{z-}} \leq \mathrm{NS}^{\,\mathrm{mesh}}_{\mathrm{z+}}) \textbf{ or } (\mathrm{e}^{\,\mathrm{cell}}_{\mathrm{z+}} \leq \mathrm{NS}^{\,\mathrm{mesh}}_{\mathrm{z+}} \textbf{ and } \mathrm{e}^{\,\mathrm{cell}}_{\mathrm{z+}} \geq \mathrm{NS}^{\,\mathrm{mesh}}_{\mathrm{z-}})] \\
&\textbf{then } \mathrm{NS\text{-}e}^{\,\mathrm{cell}}_{\mathrm{overlap}} = \textbf{true},
\end{aligned} \tag{3.2}$$

where each term represents a location outlined in Fig. 3.6. In a cell on e-Mesh ($\mathrm{e}^{\,\mathrm{cell}}$) that

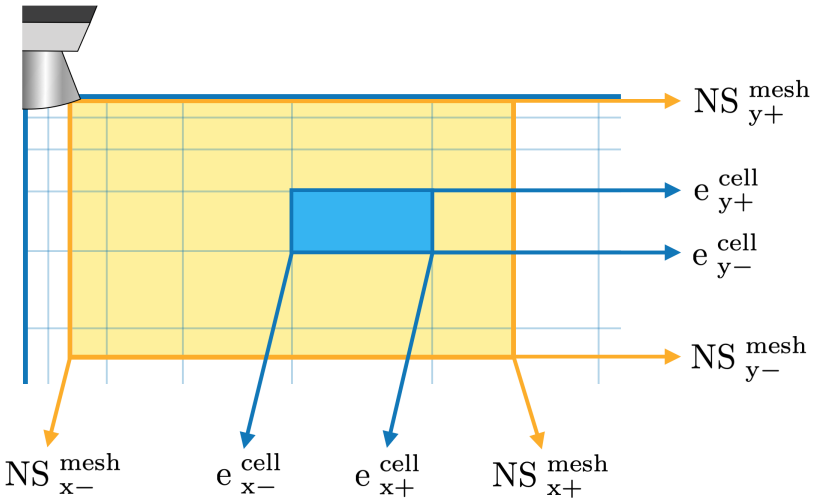



Figure 3.6: Locations of NS-Mesh boundaries (yellow) with respect to a cell on e-Mesh $\mathrm{e}^{\mathrm{cell}}$ (blue)

needs to receive charge density, i.e., if $\text{NS-e}^{\mathrm{cell}}_{\mathrm{overlap}}$ = **true**, overlapping volume fractions in the $x$, $y$ and $z$ directions ($\mathrm{VF}_x$, $\mathrm{VF}_y$ and $\mathrm{VF}_z$ respectively) are calculated in every cell on NS-Mesh ($\mathrm{NS}^{\mathrm{cell}}$) by comparing the locations outlined in Fig. 3.7. These quantities are used to calculate the charge to be migrated ($Q_{\mathrm{migration}}$) from every $\mathrm{NS}^{\mathrm{cell}}$ (Eq. group 3.3).

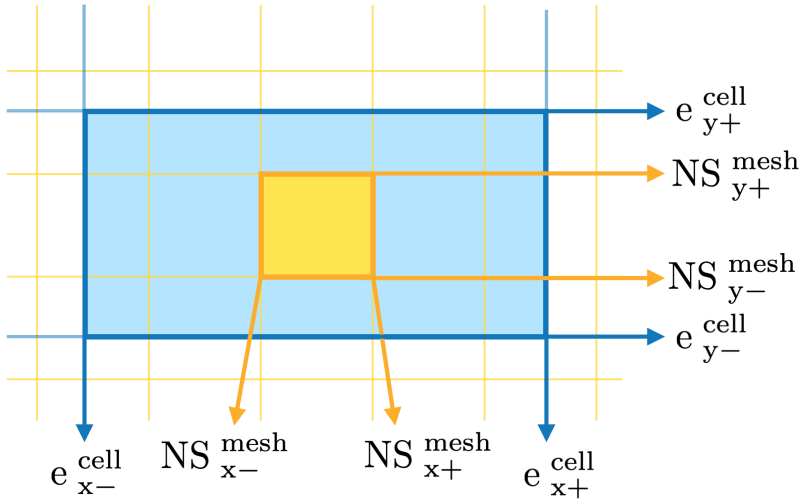



Figure 3.7: Locations of the boundaries of a cell on NS-Mesh $\mathrm{NS}^{\mathrm{cell}}$ (yellow) and a cell on e-Mesh $\mathrm{e}^{\mathrm{cell}}$ (blue)

$$
\begin{aligned}
\mathrm{VF}_x &= \min\left(1.0, \max\left(0.0, \frac{\mathrm{NS}^{\mathrm{cell}}_{\mathrm{x+}} - \mathrm{e}^{\mathrm{cell}}_{\mathrm{x-}}}{\mathrm{NS}^{\mathrm{cell}}_{\mathrm{x+}} - \mathrm{NS}^{\mathrm{cell}}_{\mathrm{x-}}}\right)\right) \\
&\quad - \min\left(1.0, \max\left(0.0, \frac{\mathrm{NS}^{\mathrm{cell}}_{\mathrm{x+}} - \mathrm{e}^{\mathrm{cell}}_{\mathrm{x+}}}{\mathrm{NS}^{\mathrm{cell}}_{\mathrm{x+}} - \mathrm{NS}^{\mathrm{cell}}_{\mathrm{x-}}}\right)\right) \\
\mathrm{VF}_y &= \min\left(1.0, \max\left(0.0, \frac{\mathrm{NS}^{\mathrm{cell}}_{\mathrm{y+}} - \mathrm{e}^{\mathrm{cell}}_{\mathrm{y-}}}{\mathrm{NS}^{\mathrm{cell}}_{\mathrm{y+}} - \mathrm{NS}^{\mathrm{cell}}_{\mathrm{y-}}}\right)\right) \\
&\quad - \min\left(1.0, \max\left(0.0, \frac{\mathrm{NS}^{\mathrm{cell}}_{\mathrm{y+}} - \mathrm{e}^{\mathrm{cell}}_{\mathrm{y+}}}{\mathrm{NS}^{\mathrm{cell}}_{\mathrm{y+}} - \mathrm{NS}^{\mathrm{cell}}_{\mathrm{y-}}}\right)\right) \\
\mathrm{VF}_z &= \min\left(1.0, \max\left(0.0, \frac{\mathrm{NS}^{\mathrm{cell}}_{\mathrm{z+}} - \mathrm{e}^{\mathrm{cell}}_{\mathrm{z-}}}{\mathrm{NS}^{\mathrm{cell}}_{\mathrm{z+}} - \mathrm{NS}^{\mathrm{cell}}_{\mathrm{z-}}}\right)\right) \\
&\quad - \min\left(1.0, \max\left(0.0, \frac{\mathrm{NS}^{\mathrm{cell}}_{\mathrm{z+}} - \mathrm{e}^{\mathrm{cell}}_{\mathrm{z+}}}{\mathrm{NS}^{\mathrm{cell}}_{\mathrm{z+}} - \mathrm{NS}^{\mathrm{cell}}_{\mathrm{z-}}}\right)\right) \\
Q_{\mathrm{migration}} &= \sum \left(\mathrm{VF}_x \times \mathrm{VF}_y \times \mathrm{VF}_z \times \mathrm{NS}_q^{\mathrm{cell}} \times \mathrm{NS}^{\mathrm{cell}}_{\mathrm{volume}} \times \mathrm{NS}^{\mathrm{cell}}_{\mathrm{VF}}\right).
\end{aligned}
\tag{3.3}
$$

Here, the summation on the left hand size operates over all the cells in the domain. $\mathrm{NS}_q^{\mathrm{cell}}$ and $\mathrm{NS}^{\mathrm{cell}}_{\mathrm{VF}}$ are the charge density and liquid fraction in the $\mathrm{NS}^{\mathrm{cell}}$ respectively. The term $\mathrm{NS}_q^{\mathrm{cell}} \times \mathrm{NS}^{\mathrm{cell}}_{\mathrm{volume}} \times \mathrm{NS}^{\mathrm{cell}}_{\mathrm{VF}}$ represents the amount of charge in the $\mathrm{NS}^{\mathrm{cell}}$ and the term

$\mathrm{VF}_x \times \mathrm{VF}_y \times \mathrm{VF}_z$ can be interpreted as its unit volumetric contribution towards migration. The scalar charge field ($Q_{\text{migration}}$) can be divided by the corresponding cell volume ($\mathrm{e}^{\text{cell}}_{\text{volume}}$) to obtain the charge density field in e-Mesh ($q_{\text{e-Mesh}}$). This way, the scalar electric charge density field $q$ is conservatively interpolated from NS-Mesh to overlapping cells on e-Mesh.

It is evident from Fig. 3.5 that there are regions handled by different processors on each mesh. A necessity for inter-processor communication of values during migration thus arises. The figure shows that processors 2, 3 and 4 ($\mathrm{NS}^{\text{processor 2}}$, $\mathrm{NS}^{\text{processor 3}}$, $\mathrm{NS}^{\text{processor 4}}$) will communicate the charge density field that exists on NS-Mesh to the overlapping region on e-Mesh that is handled by processor 1 ($\mathrm{e}^{\text{processor 1}}$).

NS-e migration is outlined in Algorithm 3.1. Here, $Q_{\text{global migration}}$ is the total charge to be migrated into an $\mathrm{e}^{\text{cell}}$ from all overlapping $\mathrm{NS}^{\text{cells}}$ and $\mathrm{e}^{\text{cell}}_q$ is the charge density in the $\mathrm{e}^{\text{cell}}$.

**Algorithm 3.1**
NS→e charge density migration algorithm

**for every** $\mathrm{e}^{\text{cell}}$
  **for every** $\mathrm{NS}^{\text{cell}}$ in each processor
    **if** $\text{NS-e}^{\text{cell}}_{\text{overlap}} =$ **true**, **then**
      compute volume fractions and $Q_{\text{migration}}$ from Eq. 3.3
    **end for**
    sum $Q_{\text{migration}}$ from all processors to get $Q_{\text{global migration}}$
    identify the processor, *my_proc*, that contains current $\mathrm{e}^{\text{cell}}$
    **if** currently at *my_proc* **then**
      **set** charge density, $\mathrm{e}^{\text{cell}}_q = Q_{\text{global migration}}/\mathrm{e}^{\text{cell}}_{\text{volume}}$
    **end if**
  **end for**
**end for**

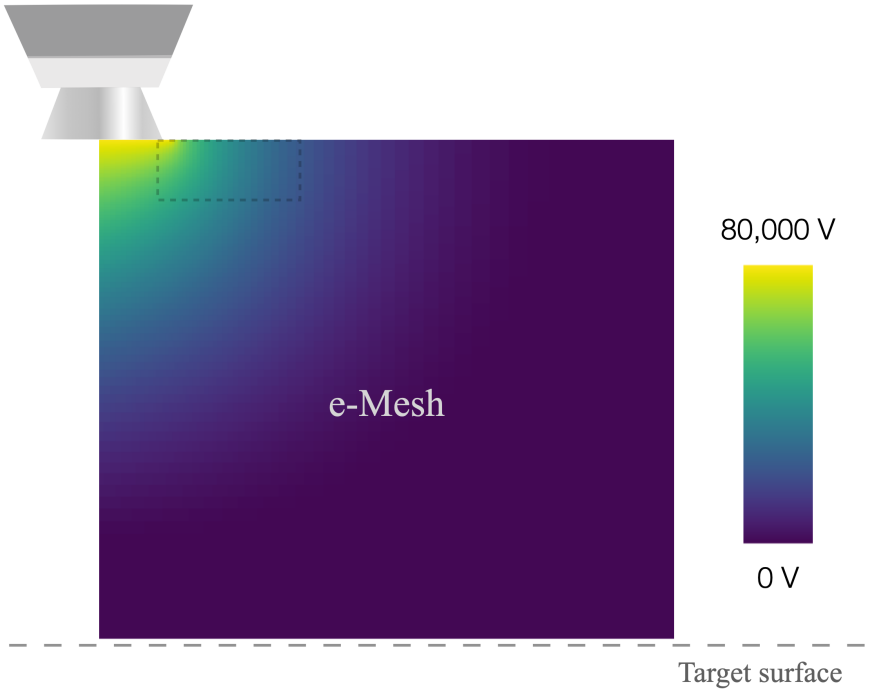



Figure 3.8: Electric potential field ($\phi_{e-Mesh}$) on e-Mesh. The nozzle is shown for reference and is not to scale.

### 3.2.5 Solving the Electric Poisson Equation on e-Mesh

The electric Poisson equation on e-Mesh (Eq. 2.8) is solved using the LGMRES method [140] included in the HYPRE library of linear algebra solvers and preconditioners [76]. In the previous sections, we presented how e-Mesh is 1) informed with the appropriate boundary conditions of potential and 2) assigned a charge density field by conservatively interpolating and communicating values from NS-Mesh. Since the spatial distribution of liquid volume is insignificant compared to the size of e-Mesh, the permittivity term ($\varepsilon$) is neglected when solving the electric Poisson equation on e-Mesh. It is important to note that $\phi$ on NS-Mesh is recomputed with the consideration of the liquid configuration. The electric potential field ($\phi_{e-Mesh}$) on e-Mesh is shown in Fig. 3.8 and spans from the bell potential (80 kV in this case) to the grounded voltage at the target surface.

### 3.2.6 Migrating Electric Potential to NS-Mesh (e→NS Migration)

Once the potential field $\phi_{\text{e-Mesh}}$ is computed , its values are migrated to the boundaries of NS-Mesh (e-NS migration) so that they can be used as BCs to solve for electric potential on NS-Mesh. This process involves similar previously discussed steps of interpolation and inter-processor communication. For a processor on NS-Mesh, every overlapping processor on e-Mesh is identified by comparing their spatial extents -

$$\begin{aligned}
&\textbf{if } [(\text{e}^{\text{ processor } i}_{\text{x}-} \leq \text{NS}^{\text{ processor } j}_{\text{x}+} \textbf{ and } \text{e}^{\text{ processor } i}_{\text{x}+} \geq \text{NS}^{\text{ processor } j}_{\text{x}-})] \\
&\textbf{and } [(\text{e}^{\text{ processor } i}_{\text{y}-} \leq \text{NS}^{\text{ processor } j}_{\text{y}+} \textbf{ and } \text{e}^{\text{ processor } i}_{\text{y}+} \geq \text{NS}^{\text{ processor } j}_{\text{y}-})] \\
&\textbf{and } [(\text{e}^{\text{ processor } i}_{\text{z}-} \leq \text{NS}^{\text{ processor } j}_{\text{z}+} \textbf{ and } \text{e}^{\text{ processor } i}_{\text{z}+} \geq \text{NS}^{\text{ processor } j}_{\text{z}-})] \\
&\textbf{then } \text{e-NS}^{\text{ processor } i-j}_{\text{overlap}} = \textbf{true.}
\end{aligned} \tag{3.4}$$

where $i$ and $j$ are processor IDs. For example, Fig. 3.9 shows a schematic representation of this comparison for $\text{NS}^{\text{ processor } 3}$ and $\text{e}^{\text{ processor } 1}$.

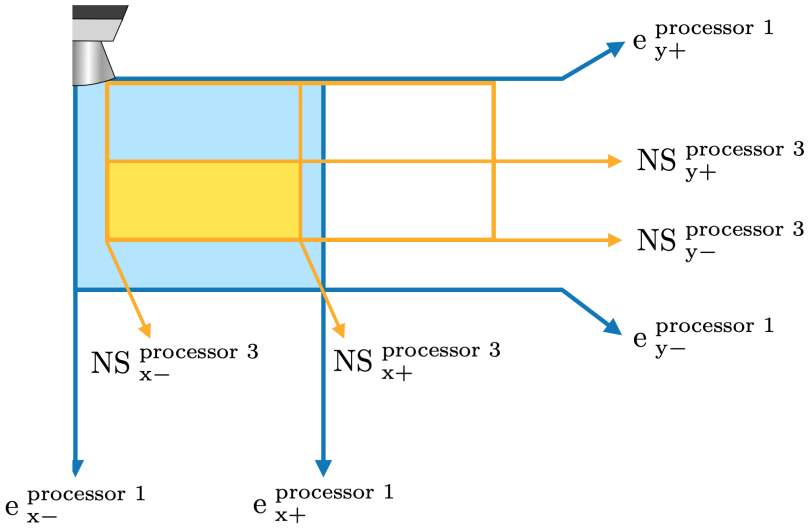



Figure 3.9: Boundaries of regions occupied by $\text{NS}^{\text{ processor } 3}$ (yellow) and $\text{e}^{\text{ processor } 1}$ (blue). Here, $\text{e-NS}^{\text{ processor } 1-3}_{\text{overlap}} = \textbf{true.}$

At the beginning of the simulation, a comprehensive communications list called

**Algorithm 3.2**
Calculating index extents for overlap between NS-Mesh and every $\mathrm{e}^{\text{ processor } n}$

**for** $n = 1, \mathrm{nproc}$

**for all** grid points along $x$ on NS-Mesh, $i = \mathrm{imin}, \mathrm{imax}$

**if** $\mathrm{NS}^{\text{cell}}_{\text{center}} \geq \mathrm{e}^{\text{processor n}}_{\text{x}-}$ **then**

**set** $\mathrm{NS}^{\text{left index}}_{\text{overlap}} = i$; **exit**

**end if**

**end for**

**for all** grid points along $x$ on NS-Mesh, $i = \mathrm{imax}, \mathrm{imin}, -1$

**if** $\mathrm{NS}^{\text{cell}}_{\text{center}} \leq \mathrm{e}^{\text{processor n}}_{\text{x}+}$ **then**

**set** $\mathrm{NS}^{\text{right index}}_{\text{overlap}} = i$; **exit**

**end if**

**end for**

**repeat** in other two dimensions

**end for**

Table 3.2: Simplified *commlist* corresponding to the setup shown in Fig. 3.5

| *receiver* \ *sender* | $\mathrm{e}^{\text{ processor 1}}$ | $\mathrm{e}^{\text{ processor 2}}$ | $\mathrm{e}^{\text{ processor 3}}$ | $\mathrm{e}^{\text{ processor 4}}$ |
|---|---|---|---|---|
| $\mathrm{NS}^{\text{ processor 1}}$ | true | false | false | false |
| $\mathrm{NS}^{\text{ processor 2}}$ | true | true | false | false |
| $\mathrm{NS}^{\text{ processor 3}}$ | true | false | false | false |
| $\mathrm{NS}^{\text{ processor 4}}$ | true | true | false | false |

**Algorithm 3.3**
Calculating index extents for overlap between e-Mesh and every NS $^{\text{processor } n}$

**for** $n = 1, \text{nproc}$

**for all** grid points along $x$ on e-Mesh, $i =$ e_imin, e_imax

**if** $\text{e}\,^{\text{cell}}_{\text{center}} \geq \text{NS}\,^{\text{processor } n}_{\text{x}-}$ **then**

**set** $\text{e}\,^{\text{left index}}_{\text{overlap}} = i$; **exit**

**end if**

**end for**

**for all** grid points along $x$ on e-Mesh, $i =$ e_imax, e_imin, $-1$

**if** $\text{e}\,^{\text{cell}}_{\text{center}} \leq \text{NS}\,^{\text{processor } n}_{\text{x}+}$ **then**

**set** $\text{e}\,^{\text{right index}}_{\text{overlap}} = i$; **exit**

**end if**

**end for**

**repeat** in other two dimensions

**end for**

*commlist* is created using e-NS $^{\text{processor } i-j}_{\text{overlap}}$. The flag values in *commlist* corresponding to the schematic shown in Fig. 3.5 is tabulated in Table 3.2. In addition to the overlap flags, the index extents of e $^{\text{cells}}$ that send data to each NS $^{\text{processor}}$ and the index extents of NS $^{\text{cells}}$ that receive data from each e $^{\text{processor}}$ are identified and stored as outlined in Algorithms 3.2 and 3.3 respectively. e-NS $^{\text{processor } i-j}$ communication is then performed as dictated by *commlist*.

For a cell lying on the boundary of NS-mesh, say NS $^{\text{boundary cell}}$, and belonging to processor NS $^{\text{processor p}}$, the nearest cell on e-Mesh is identified and an appropriate 12-point stencil from e-Mesh is communicated to NS $^{\text{processor p}}$. The 12 points comprise of two upstream and downstream points each in $x, y$ and $z$ directions. Using the electric potential values ($\phi_{\text{e-Mesh}}$) at each point in the stencil, the electric potential value ($\phi$) at the center of every NS $^{\text{boundary cell}}_{\text{center}}$ is computed using a tricubic interpolation scheme described in Lekien and Marsden [92]. Algorithm 3.4 outlines the process of e→NS migration.

### 3.2.7 Challenges and Cost With Using E-mesh

The e-Mesh module has a significant impact on the overall cost of the simulation. The electric Poisson solver on e-Mesh is much more expensive than that on NS-Mesh perhaps due to complexities introduced by the non-uniform grid. The migration of charge densities and electric potential stencils involves repeated communication between multiple sets of processors, making the process expensive. On average, solving the electric Poisson equation (Eq. 2.8) on e-Mesh accounts for up-to 74% of a timestep. For this reason, the potential field on e-Mesh is solved every 50 timesteps. The interval between two consecutive electric potential field solutions on e-Mesh has an non-significant impact on the accuracy of the electric potential boundary conditions on NS-Mesh. This is because the timestep is extremely small (about 0.01 $\mu$s) and the fluid displacement between two consecutive e-Mesh solutions is a fraction of the cell width.

In this way, e-Mesh is used exclusively as an electric potential solver. e-Mesh spans

**Algorithm 3.4**
e→NS electric potential field migration algorithm

**for** $n = 1, \text{length}(commlist)$

read *sender*, *receiver* and $\text{e}\,^{\text{index}}_{\text{overlap}}$ index range to be communicated

**if** currently at *sender* **then**

send $\phi_{\text{e-Mesh}}$ data to *receiver*

send $\text{NS}\,^{\text{index}}_{\text{overlap}}$ range to *receiver*

**end if**

**if** currently at *receiver* **then**

receive $\phi_{\text{e-Mesh}}$ data and $\text{NS}\,^{\text{index}}_{\text{overlap}}$

**for** $i = \text{NS}\,^{\text{left index}}_{\text{overlap}}$ , $\text{NS}\,^{\text{right index}}_{\text{overlap}}$

**for** $ii = \text{e}\,^{\text{left index}}_{\text{overlap}}$ , $\text{e}\,^{\text{right index}}_{\text{overlap}}$

**if** $\text{e}\,^{\text{cell } ii}_{\text{center}} \geq \text{NS}\,^{\text{cell } i}_{\text{center}}$ **exit**

repeat in other two dimensions to identify nearest $\text{e}\,^{\text{cell}}_{\text{center}}$

compute tricubic interpolated value

set $\phi\,^{\text{cell}}_{\text{NS-Mesh}}$

**end for**

**end for**

**end if**

**end for**

between regions of well-defined electric potential values that serve as boundary conditions. Making the flow domain (NS-Mesh) this large would be uneconomical. The charge density field is made available on e-Mesh by migrating (interpolating and communicating) the data from NS-Mesh. Using the available electric potential boundary conditions and the scalar charge density field, the electric potential field is solved on e-Mesh. The values of electric potential are migrated (interpolated and communicated) back to the boundaries of NS-Mesh so that the electric potential field can be recomputed accurately on the flow domain.

## 3.3 Mesh Sensitivity

To determine the effect of mesh resolution on atomization and to help choose an optimal numerical setup, three simulations of an electrified RBA jet (Table 3.1) are performed with varying mesh resolutions (Table 3.3). Fig. 3.10 shows that droplets larger than 10 $\mu$m are resolved in a 5 cells-per-diameter (CPD) mesh while the 10 CPD mesh captures droplets smaller than 10 $\mu$m. Additionally, the 15 CPD mesh captures the droplets even smaller than 5 $\mu$m. Larger droplets are similarly resolved for all meshes. Between the two finer meshes the smaller droplets are increasingly well resolved.

The necessity for a mesh finer than 5 CPD is apparent since the coarseness of the mesh does not allow for charge migration to be captured. All liquid structures in the 5 CPD mesh contain the injected charge density value of 2.879 C/m$^3$. Using 10 and 15 CPD meshes, we are able to resolve the charge migration process and investigate the resulting droplet charge distribution. Most droplets contain a charge density close to the initial bulk charge density value. Compared to the initial charge density, it is more probable to find a droplet with a lower charge density. Fig. 3.11 highlights that charge migration is more resolved in a 15 CPD mesh and is consistent in its trend with the 10 CPD mesh. Although there is uncertainty with the smallest scales of droplet sizes, the number of droplets larger than 20 $\mu$m does not vary on increasing the mesh resolution, suggesting that the larger droplets are well resolved

Table 3.3: Mesh sensitivity simulation domain parameters

| **Mesh ID** | **Cells per diameter** | **Cell width** | **Processor count** | **No. of structures** |
|---|---|---|---|---|
| 05 CPD | 5 | 12 $\mu$m | 16 | 74 |
| 10 CPD | 10 | 6 $\mu$m | 96 | 121 |
| 15 CPD | 15 | 4 $\mu$m | 256 | 705 |

in a 15 CPD mesh. The relevant physical processes are sufficiently captured on a 15 CPD mesh.

### 3.3.1 Sensitivity of Droplet Sizes to Mesh Resolution

Fig. 3.10 shows that droplets larger than 10 $\mu$m are resolved in a 5 cells-per-diameter (CPD) mesh while the 10 CPD mesh captures droplets smaller than 10 $\mu$m. Additionally, the 15 CPD mesh captures the droplets even smaller than 5 $\mu$m. Larger droplets are similarly resolved for all meshes. Between the two finer meshes the smaller droplets are increasingly well resolved. Although there is uncertainty with the smallest scales of droplet sizes, the number of droplets larger than 20 $\mu$m does not vary on increasing the mesh resolution, suggesting that the larger droplets are well resolved in a 15 CPD mesh. Since this project is driven by an industrially relevant process, it was decided that a 15 CPD mesh is able to capture the physics of atomization associated with the smallest droplets commonly seen in the paint shop which are about 10 $\mu$m in diameter [7, 49]. Therefore, all subsequent results presented in Chapters 4, 5 and 6 are obtained from simulations performed on a 15 CPD mesh.

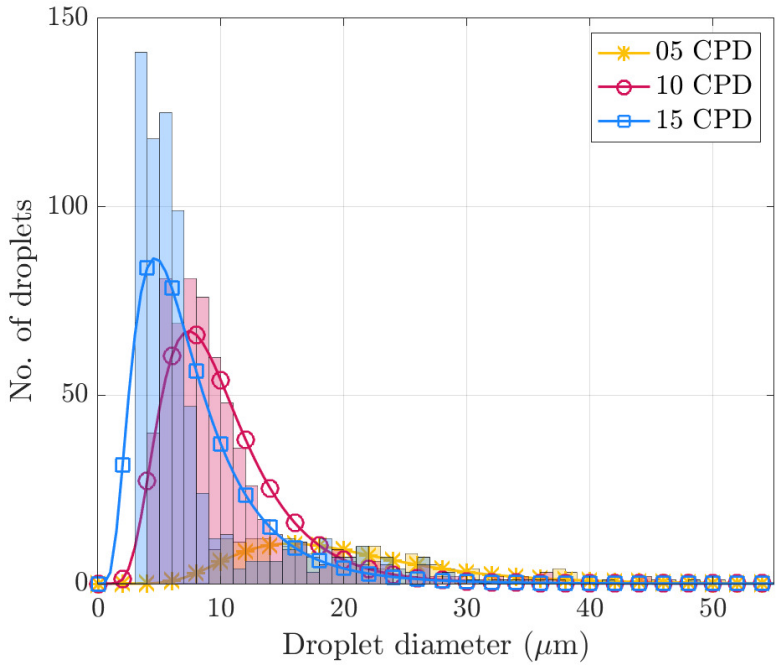
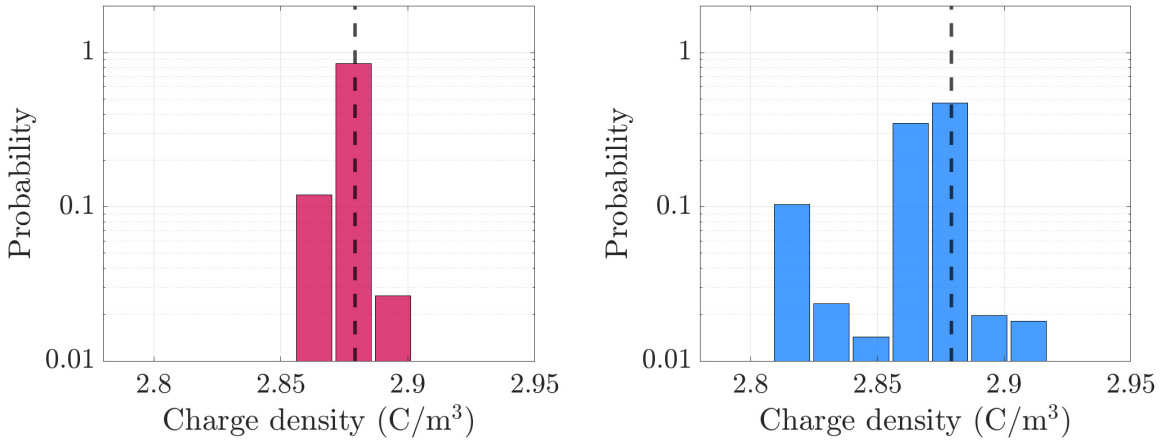



Figure 3.10: Probability distribution of droplet sizes for varying mesh resolutions. The lines show a log-normal fit of the data.




(a) 10 CPD

(b) 15 CPD

Figure 3.11: Volume weighted charge density probability distributions for varying mesh resolutions. Note the logarithmic scale on the y-axis.

### 3.3.2 Sensitivity of Droplet Charge Densities to Mesh Resolution

The coarseness of a 5 CPD mesh does not allow for charge migration to be captured. All liquid structures in the 5 CPD mesh contain the injected charge density value of 2.879 C/m$^3$. Using 10 and 15 CPD meshes, the charge migration process can be resolved to investigate the resulting droplet charge distribution. Most of the droplets contain a charge density close to the initial bulk charge density value. Compared to the initial charge density, it is more probable to find a droplet with a lower charge density. Fig. 3.11 highlights that charge migration is more resolved in a 15 CPD mesh and is consistent in its trend with the 10 CPD mesh.

## 3.4 Droplet Ancestry Extraction

### 3.4.1 Insights From Droplet Statistics

High-fidelity simulations of complex systems can resolve the relevant time and length scales required to extract droplet ancestry statistics as a valuable means of understanding the physics of atomization. In this work, a droplet ancestry extraction tool first introduced by Rubel and Owkes [139] and further developed by Christensen and Owkes [31] is employed to extract and store droplet and local flow field statistics during each breakup and coalescence event in simulations of near-bell atomization in ERBAs.

The information is stored in a Neo4j graphical database and analyzed to track the evolution of the liquid as it moves from the liquid core to small droplets in an atomizing flow. Graph databases are frequently used in the business industry to identify relationships between products and consumers through links that can reveal patterns in consumer behavior. A similar approach is used to create paths that connect droplets through breakup and coalescence events in atomization simulations.

The analysis allows us to compute breakup and coalescence statistics, which characterize the drop size distributions and help us understand the processes driving breakup. Such insights into complex atomizing flows are challenging to obtain using experimental methods. The tool allows for the analysis of droplet behavior in regions that are not easily observable or measurable, such as near the bell edge or within the dense droplet cloud. It also enables the study of the behavior of charged droplets under the influence of a background electric field.

### 3.4.2 Method of Extraction

The droplet ancestry extraction algorithm was developed and demonstrated on atomizing flows by Rubel and Owkes [139] and Christensen and Owkes [31]. It is incorporated

into the ERBA simulation tool to track, collect, and store statistics of droplet breakup and coalescence events throughout the simulation. The droplet ancestry algorithm identifies breakup and coalescence events at every time-step. The algorithm operates through the implementation of two identification numbers, namely the structure ($\mathcal{S}$) and liquid ($\mathcal{L}$) identification numbers. $\mathcal{S}$ is a unique integer computed for each liquid structure using a connected component labeling algorithm [67, 68, 75] and provides information of the current state of all the structures. $\mathcal{L}$ is a unique integer that is transported with the liquid providing a time history of the fluid. Together, the numbers allow for breakup and coalescence events to be identified [31]. Coalescence events occur when structures occupy the same computational cell and breakup events occur when a gap of one computational cell forms between structures containing the same $\mathcal{S}$ value. This formulation prevents the occurrence of fictitious, repetitive coalescence and breakup events [31].

### 3.4.3 Storing Statistics in a Database

Once these key events are identified, the information listed below regarding parent and child droplets are extracted and stored in a CSV file for convenient analysis and post-processing.

1. Breakup/coalescence event identifier
2. Event time
3. Liquid identification numbers of the parent and child structures
4. Structure identification numbers of the parent and child structures
5. Volumes of the parent and child structures
6. Principal axes lengths of the parent and child structures
7. Position vector of the structure
8. Velocity vector of the structure
9. Velocity vector of the surrounding gas phase

10. Vorticity vector of the structure
11. Viscosity values in the parent and child structures
12. Charge density values in the parent and child structures

### 3.4.4 Post-processing the Statistics

The droplet ancestry statistics extraction tool operates throughout the simulation and connects successive breakup/coalescence events to create an ancestry or family tree describing the evolution of the spray cloud. Fig. 3.12 displays the ancestry as interpreted by a Neo4j graphical database for the simulation of a non-electrified 15 CPD jet. The nodes represent individual droplets and the lines connecting them represent the associated breakup events. The ligament core is in the center of the image. To maintain the visibility of the nodes and lines, only droplets which broke up up-to six times and their "ancestors" are displayed in the image. The statistics associated with each node are also stored in the database and can be processed to provide insights on the breakup mechanisms in ERBAs. Results and insights from such analyses are presented in Chapters 5 and 6 where extracted statistics are compared to quantify the effects of different flow conditions on atomization.

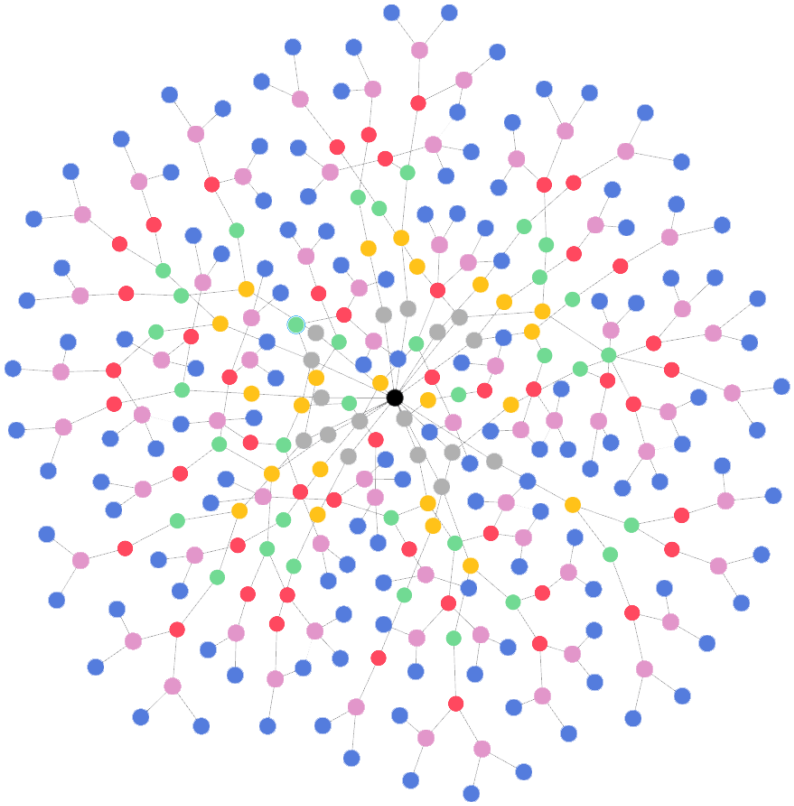


Figure 3.12: Droplet ancestries in the jet shown in Fig. 4.1 represented using the Neo4j graphical database. The colors represent breakup levels 1 (gray), 2 (yellow), 3 (green), 4 (red), 5 (pink) and 6 (blue) breakup events. Lines connect related droplets, i.e., droplets which split from each other. The ligament core (black) is present at the center of the image. Each node contains relevant statistics from the breakup event.

## 3.5 Computational Cost

Fig. 3.13 shows the computational cost associated with each module in the solver during a timestep in which e-Mesh does not participate. As mentioned, e-Mesh is used to update the electric potential boundary conditions on the flow domain (NS-Mesh) once every 50 timesteps. In a timestep where e-Mesh is active, it takes up upto 74% of the cost, which is significant.

A closer look at Fig. 3.13 shows that the two most expensive modules are the ones that handle pressure and the electric field. Interestingly, both modules contain a step where a Poisson equation is solved. The Poisson solver is often computationally expensive in numerical methods. In this setup, the electric Poisson equation is solved using the LGMRES iterative method which is available in the HYPRE library of linear algebra solvers and preconditioners [76]. The pressure Poisson equation is solved using a multigrid technique which employs a coarse grid to accelerate the convergence of the solution. By leveraging the grid hierarchy and adapting the solution at multiple levels, the multigrid method can converge to an accurate solution more quickly than a single-level LGMRES iterative solver.

The transport module handles multiphase flows, interface tracking and surface tension computations. The 1% sector comprises of writing simulation metrics to log files, generating outputs for post-processing, liquid and structure identifications associated with the droplet ancestry tool, and rest periods. Each 15 CPD simulation contains 69,984,000 computational cells on NS-Mesh and 5,400,000 computational cells on e-Mesh. The wall time for 300 $\mu$s of simulation time was about 650 hours without electrification on 128 processors and about 1500 hours for a simulation that included EHD effects on 256 processors. The computational efforts were performed on the Hyalite High Performance Computing System and the Tempest High Performance Computing System, operated and supported by University Information Technology Research Cyberinfrastructure at Montana State University.

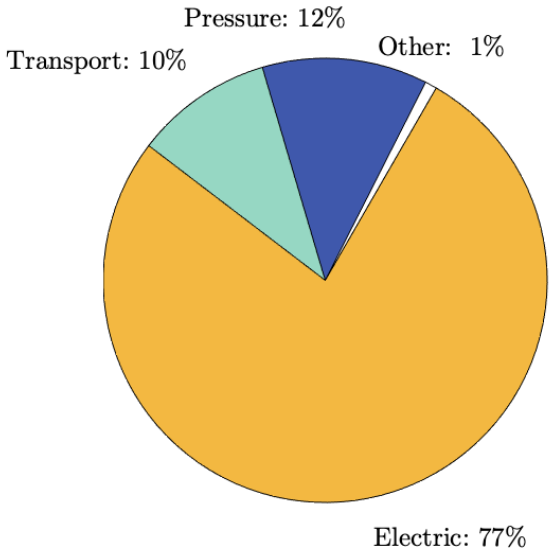



Figure 3.13: Breakdown of the computational cost of notable modules in the numerical solver. The electric module which handles solutions to the EHD equations presented in Section 2.1.2 is the most expensive part of the solver taking up to 77% of the cost; the transport module which handles multiphase flows and interface tracking accounts for 10% of the cost; the pressure solver accounts for 12% of the cost.

# CHAPTER FOUR

# DEMONSTRATION OF NUMERICAL FRAMEWORK

In this chapter, the tool developed to simulate near-bell atomizing flows in ERBAs is demonstrated to be well-posed. A parameter study is conducted to understand the effects of different operating conditions on the flow profile. Finally, a non-dimensional analysis of the setup is briefly presented to understand the importance of different physical processes.

## 4.1 Liquid Interface

Figs. 4.1 and 4.2 show the positions of the liquid interface of the jet at different instances in time as viewed from different viewing planes. These simulations are performed on a 15 CPD mesh with parameters Table 3.1. Complex and chaotic breakup activity comprising primary and secondary atomization that begins approximately 6 mm away from the bell edge is observed. The breakup processes leading to primary atomization consist of ligament thinning, Rayleigh-Plateau instabilities and aerodynamic breakup due to interaction with quiescent air. A more detailed analysis of the breakup mechanisms is presented in the next chapter.

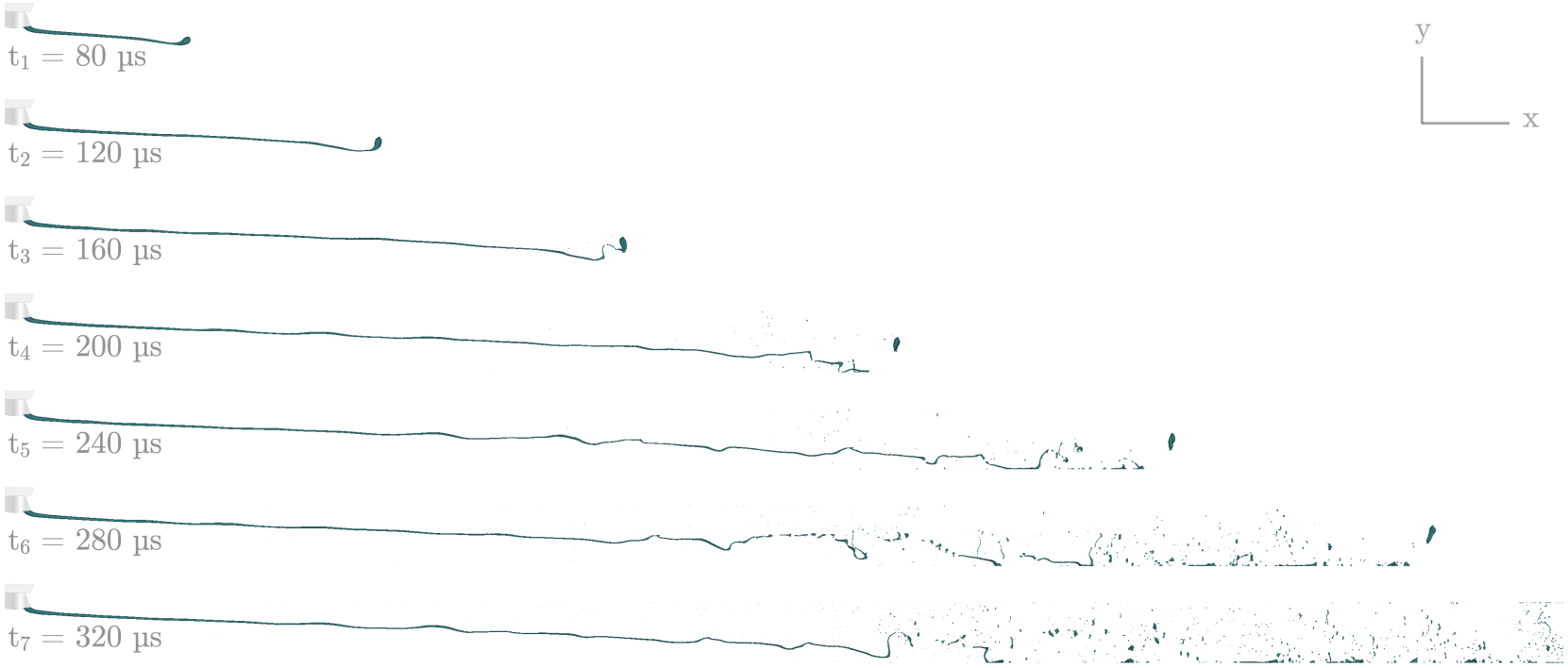
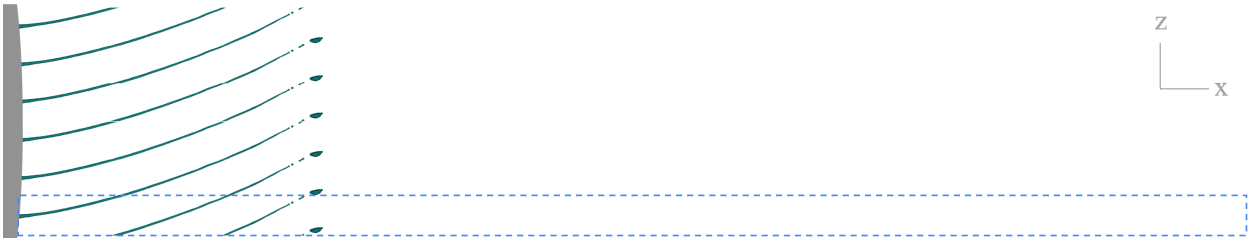
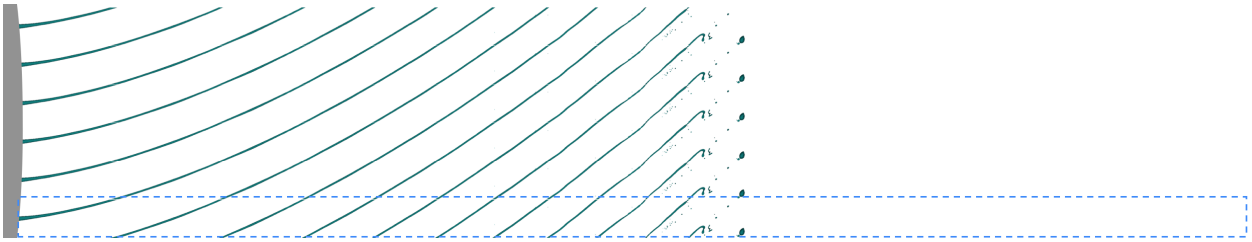


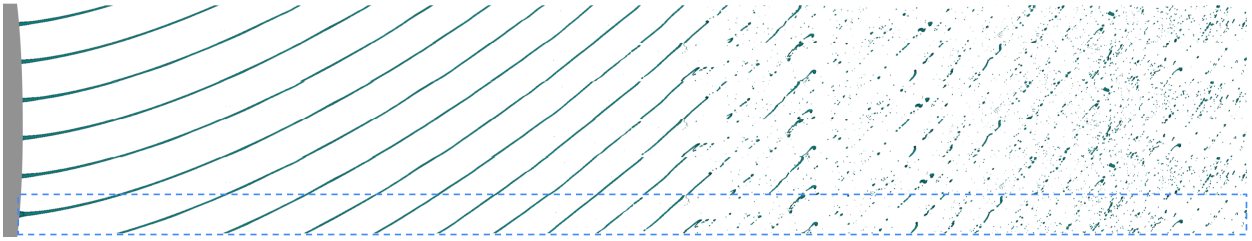

Figure 4.1: Liquid interface positions of a single jet exiting the edge of the bell at different times as viewed from an $x$-$y$ plane. The nozzle is shown for reference at the top left corner of each image and is not to scale.




(a) t = 120 $\mu$s



(b) t = 200 $\mu$s



(c) t = 320 $\mu$s

Figure 4.2: Liquid interface positions of six individual jets exiting a serrated bell edge at different times as viewed from an $x$-$z$ plane. The nozzle is rotating clockwise and is shown for reference at the left edge of each image and is not to scale. The simulation domain is outlined by a dashed box. Owing to the periodic boundary conditions along the $z$-axis, an arc along the bell edge spanning six serrations is depicted in this view by stacking the domains in an attempt to vaguely recreate some experimental images [42, 118, 153, 176].

## 4.2 Electric Potential Field

The electric potential field (Fig. 4.3) in the domain (NS-Mesh) ranges from the bell potential (80 kV) to about 20 kV. In the figure, the trajectory of the liquid jet is graphically shown as a dashed white line. The contour lines of electric potential, shown as solid lines, are almost parallel to the $y$-axis in this regime. This indicates that the electric field and the electric force vectors are oriented perpendicular to the $y$-axis, i.e., in the direction of lower potential. A schematic representation of the direction of the electric force (blue line) acting on a control volume (blue circle) is shown for clarity. It is important to note that the electric force acts along the radially outward direction of the liquid jet in this regime as this has significant effects on the flow development which will be discussed in the following sections.

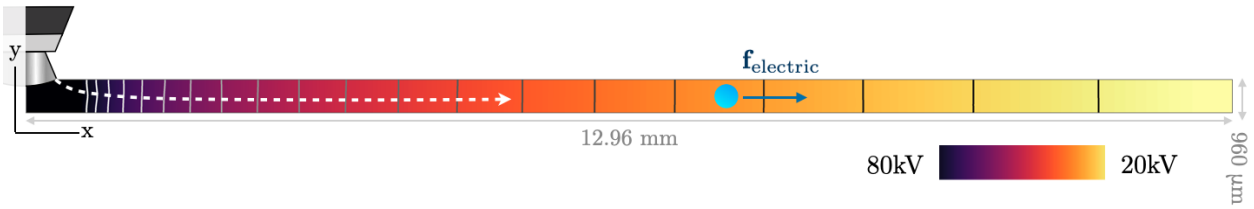



Figure 4.3: The electric potential field and its corresponding contour lines on an $x$-$y$ plane in the domain. The trajectory of the liquid jet is shown graphically as a dashed white line. The electric force vector (blue arrow) that acts on a control volume (blue circle) in this regime is also schematically represented. The bell is shown at the top left corner and is not to scale.

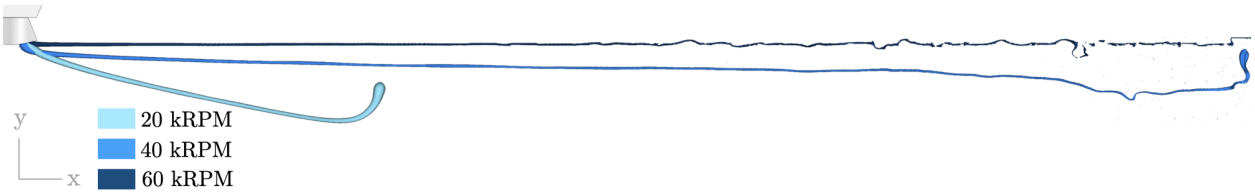
## 4.3 Parameter Study

A parameter study is performed on a 15 CPD mesh to understand the effects of changing four parameters - nozzle rotation rate, liquid flow rate, liquid charge density, and bell electric potential. 9 separate simulations were performed totaling to a wall time of about 14,000 hours. Results of the parameter study are shown in Fig. 4.4 as snapshots of the liquid interface after 200 $\mu$s. The standard values of all varied properties are listed in Table 3.1

unless otherwise stated in the figure.

As the nozzle rotation rate increases, centrifugal forces are stronger on the jet and stretch it out faster leading to early elongation and breakup (Fig. 4.4(a)). Slower rotation rates do not stretch the jet out as much in the same duration. A higher flow rate through the same jet diameter acts in the same way as increasing jet velocity, which initially pushes the jet out further before centrifugal forces take over (Fig. 4.4(b)). These results are in agreement with experimental observations conducted by [35].

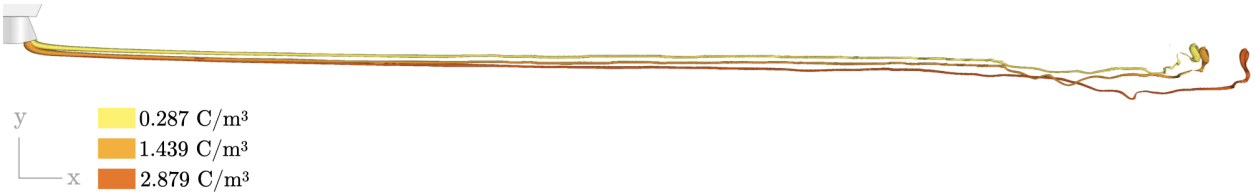
An increase in either $q_{\text{in}}$ or $\phi_{\text{bell}}$ stretches the jet along its downstream direction (Figs. 4.4(c), 4.4(d)). This is because the Coulomb force vectors point towards the direction of propagation of the liquid jet, i.e., the electric potential field contour lines are approximately perpendicular to the liquid velocity at that location as explained in Fig. 4.3.



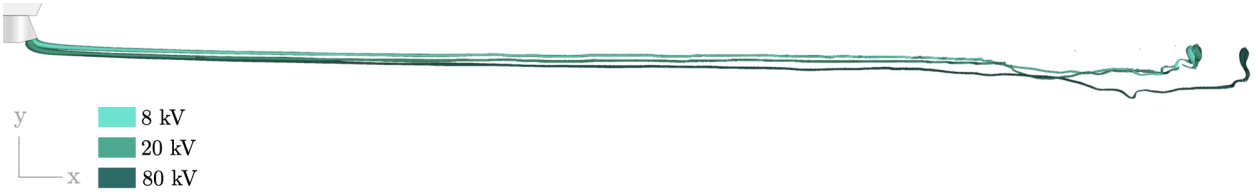

(a) Varying rotation rate




(b) Varying flow rate




(c) Varying liquid charge density




(d) Varying bell electric potential

Figure 4.4: A comparison of snapshots of the liquid interface positions after 200 $\mu$s in the parameter study simulations. The nozzle is shown for reference at the top left corner of each image and is not to scale.

## 4.4 Examining Non-Dimensional Quantities

The non-dimensional numbers corresponding to the simulations are listed in Table 4.1. In the interest of understanding the effect of EHD on the flow, the relevant non-dimensional numbers are briefly discussed. The electric Reynolds number ($\mathrm{Re}_e$) [162] is the ratio of the charge advection timescale to the charge mobility timescale while the electric Péclet number ($\mathrm{Pe}_e$) [151] is a measure of the charge mobility timescale to the charge diffusion timescale. For high values of $\mathrm{Re}_e$, charge migration is insignificant and the initial charge distribution will prevail in the liquid jet. For low values of $\mathrm{Re}_e$, charge migration acts quickly to relax the charges to the surface allowing for surface charge models to be appropriate. For high values of $\mathrm{Pe}_e$, charge migration dominates the charge diffusion process and vice versa. Based on the values of $\mathrm{Re}_e$ and $\mathrm{Pe}_e$ for this setup, it is reasonable to model all three charge dynamics processes, i.e., advection, diffusion, and migration, since their timescales are comparable to one another. The electric Bond number [22] quantifies the importance of the deforming electrical force compared to the restoring surface tension force. A low value signifies the dominance of surface tension-driven breakup activity. The electro-inertial number [151] denotes the importance of EHD forces compared to inertial advective forces. A low value implies that inertial forces predominantly drive the hydrodynamics of the flow in this setup.

In order to better understand the effect of electrification on atomization, a more in depth comparative study between an electrified and a non-electrified jet was conducted. The findings are presented in the next chapter.

Table 4.1: Non-dimensional numbers used in the ERBA simulations

| **Number** | **Definition** | **Value** |
|---|---|---|
| Density ratio | $\rho_l/\rho_g$ | 830.56 |
| CFL | $\lvert\mathbf{u}_{\max}\rvert\Delta t/\Delta x$ | 0.30 |
| Bulk Weber | $\rho_l\lvert\mathbf{u}_{\text{jet}}\rvert^2\mathrm{D}_{\text{jet}}/\gamma$ | 77.87 |
| Permittivity ratio | $\varepsilon_l/\varepsilon_g$ | 50.00 |
| Electric Reynolds ($\mathrm{Re}_e$) | $\varepsilon_l\lvert\mathbf{u}_{\text{jet}}\rvert/(Lq_l\psi_l)$ | 8.93 |
| Electric Péclet ($\mathrm{Pe}_e$) | $q_l\psi_l L^2/\left(\mathcal{D}_l\varepsilon_l\right)$ | 0.21 |
| Electric Bond | $\varepsilon_l\lvert\mathbf{E}\rvert^2 L/\gamma$ | 0.091 |
| Electro-inertial | $q_l^2L^2/\left(\varepsilon_l\rho_l\lvert\mathbf{u}_{\text{jet}}\rvert^2\right)$ | 0.0017 |

# CHAPTER FIVE

# EFFECT OF ELECTRIFYING THE SETUP

An overarching question among engineers operating ERBAs in industrial applications (particularly in automotive paint shops) is - "*What is the effect of the electrification on atomization and how can it be used to improve the performance of the device?*". Crucial metrics such as the droplet size uniformity, surface finish quality, TE, deposition thickness, and environmental impact are directly dependent on the atomization process of ERBAs [9, 35, 43].

Two simulations are performed - one in a non-electrified setup and one in an electrified setup - in a domain as described in Chapter 3 with parameter values listed in Table 3.1. The two simulations are identical except that there is no background electric potential and no liquid charge density in the former. The two cases are simulated to help understand the effect of charges and the background electric field on the breakup mechanisms driving atomization. The rest of this chapter is organized as follows - a qualitative comparison between the liquid interfaces of the two simulated cases is followed by a quantitative comparison between the two simulated cases where inferences are drawn based on the overall spray characteristics and droplet statistics including size, shape, velocity, and charge density.

## 5.1 Liquid Interface

Figs. 5.1 and 5.2 show the positions of the liquid interface of the jet at different instances in time as viewed from different viewing planes. Long ligaments, irregular droplet structures, and chaotic breakup activity comprising primary and secondary atomization that begins approximately 6 mm away from the bell edge is observed. Primary atomization is characterized by the processes of ligament thinning, Rayleigh-Plateau instability growth

and aerodynamic breakup due to interaction with quiescent air. Sinuous instabilities are observed in both cases but seem suppressed in the electrified jet. The reason for suppressed instability growth will be discussed in the following sections. As seen in Fig. 4.3, the electric force, which points radially outward, elongates the electrified jet along the $x-$direction and enhances breakup activity.

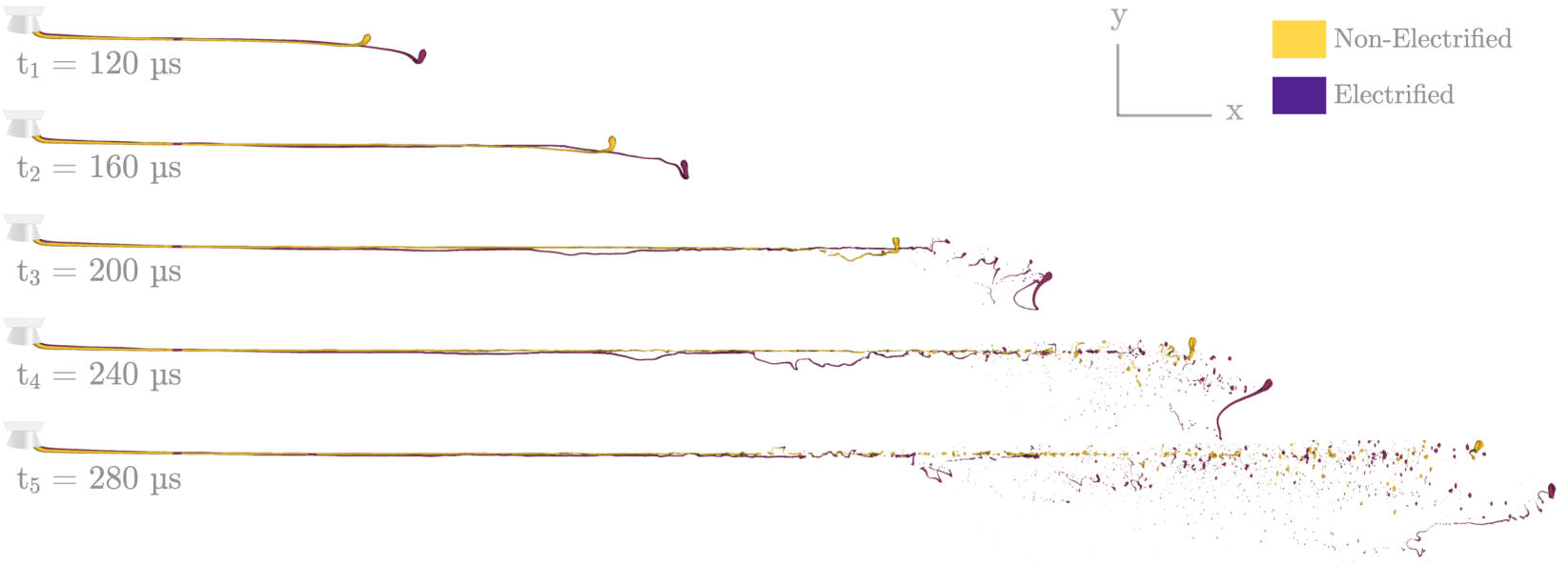
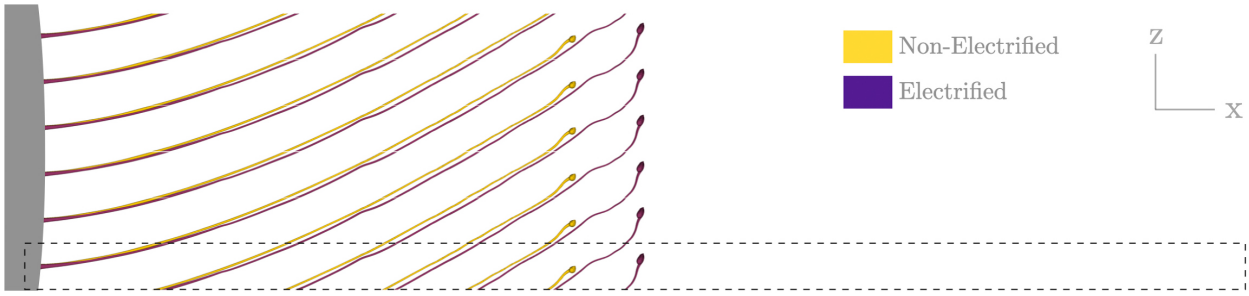
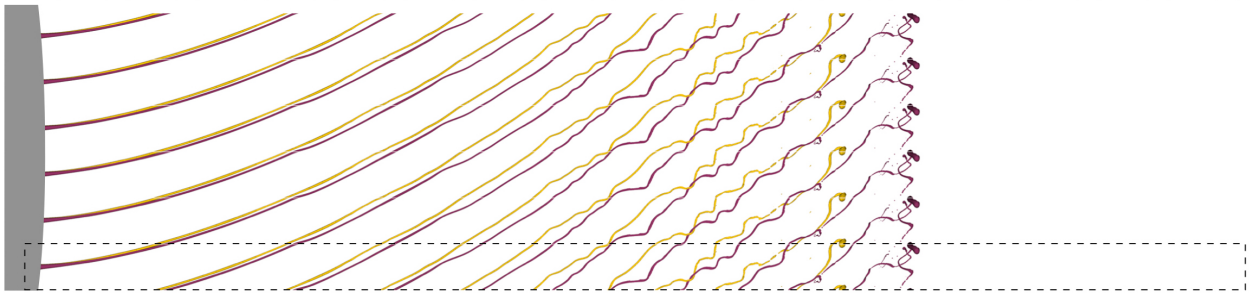


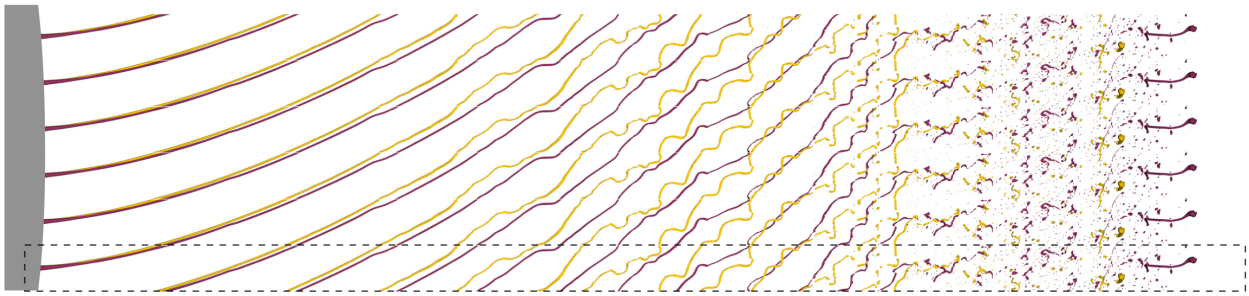

Figure 5.1: Liquid interface positions in a non-electrified (yellow) and an electrified (violet) jet after exiting the edge of the bell on an $x$-$y$ plane at different times. The nozzle is shown for reference at the top left corner and is not to scale.




(a) t = 160 $\mu$s



(b) t = 200 $\mu$s



(c) t = 240 $\mu$s

Figure 5.2: Liquid interface positions of six individual non-electrified (yellow) and electrified (violet) jets exiting a clockwise-rotating serrated bell edge (left, not to scale) as viewed at different times from an $x$-$z$ plane. The simulation domain is outlined by a dashed box. Owing to the periodic boundary conditions along the $z$-axis, an arc along the bell edge spanning six serrations is depicted in this view by stacking the domains in an attempt to recreate experimental images available in Shirota et al. [153], Oswald et al. [118], Domnick [42] and Wilson et al. [176].

## 5.2 Spray Characteristics

The spray statistics point to the observation that electrification enhances breakup activity. The radial liquid penetration after 300 $\mu$s is 5% more for the electrified jet. The spray angle characterizes the dispersion of the spray and is computed as the angle about the $z$ axis on the $x$-$y$ plane out of the bell edge such that 90% of the liquid is within the prescribed region created by that angle. The spray angle is about 3.4 times greater for the electrified jet. The distribution of droplet spacing (Fig. 5.3), which can be quantified as the distance between every droplet pair in the spray, further reflects the larger spray coverage in the electrified jet where the mean droplet spacing which is 12% more than the non-electrified case. All these metrics suggest that atomization and breakup activity is enhanced by the electric field. As seen in Fig. 4.3, the electric force points radially outward and increases penetration and spray coverage in electrified flows. Droplet spacing is an important metric in rotary sprays and the electric field has a significant impact on it. The optimal operating conditions of the electrified atomizer have to be carefully selected.

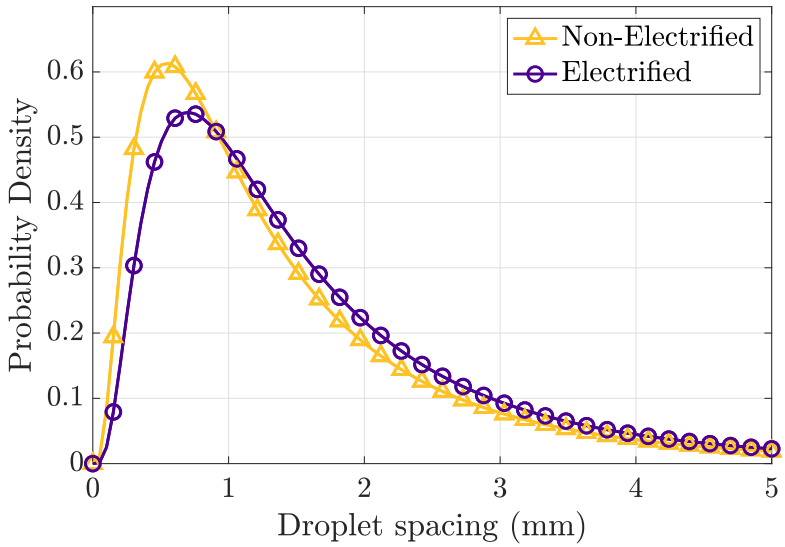



Figure 5.3: Log-normal fit of the near-bell droplet spacing probabilty density.

In contrast, the breakup length, i.e., the length of the main ligament core, is 4% longer for the electrified jet. Moreover, the first instance of breakup occurs 6% later in the electrified jet. This can be attributed to the stabilizing force provided by the electric field on the charged liquid core [107, 112, 144]. Saville [143] found that under certain conditions, electrical shearing forces can stabilize the cylindrical interface to axisymmetric deformations. In another study conducted by Bhuptani and Sathian [23], the axial electric field has been quantitatively shown to have a stabilizing effect on nanoscale liquid threads. However, the next section contains evidence that once breakup begins, the electric field accelerates the processes leading to secondary atomization.

## 5.3 Atomization Characteristics

The droplet ancestry statistics extraction tool described in Section 3.4 operates throughout the simulation and connects successive breakup/coalescence events to create an ancestry or family tree describing the evolution of the spray cloud. Using this tool, several atomization statistics related to the droplet size, shape, velocity, and charge density are extracted and analyzed to gain insights into the atomization process in ERBAs. The results are compiled after analyzing 837 liquid structures in the non-electrified setup and 1119 liquid structures in the electrified setup.

According to Pendar and Páscoa [128], the presence of electric charges within liquid structures causes a net reduction in the effective surface tension in large droplets and ligaments and therefore an increase in their effective local Weber number. This leads to enhanced breakup activity. After 300 $\mu$s, the electrified jet contains about 25% more droplets than the non-electrified jet. Fig. 5.4 shows the time evolution of the number of liquid structures in the domain. The delay in the first instance of breakup (discussed in the previous section) and the accelerated breakup in the electrified jet are evident from the plot. A closer look at the droplet statistics, which will be presented in the following sections,

provides more evidence for the enhanced atomization in an electrified jet.

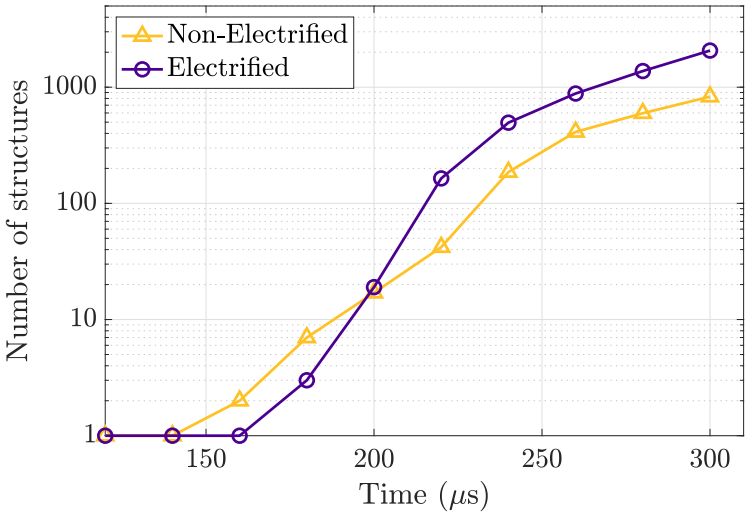



Figure 5.4: The total number of droplets in the domain over time. Note the logarithmic scale on the $y$-axis.

Two major types of atomization are identified in this system - primary and secondary. Primary atomization occurs when droplets split from the main ligament core. Secondary atomization comprises all breakup following primary atomization which includes second, third, fourth, etc. breakup events of the same structure. These subsequent breakup events are also called breakup levels in the following discussion. For clarity, breakup level 1 corresponds to liquid structures that are formed due to primary atomization, i.e., breakup from the main ligament core; breakup levels 2 onward correspond to liquid structures created from secondary atomization events. In a non-electrified jet, 1.64% of the total number of droplets formed in the simulation are from primary atomization (broke up once) and 98.36% are from secondary atomization (broke up two or more times). The prevalence of secondary atomizing events indicates that the droplet cloud is heavily dependent on mechanisms within this regime. The dominance is more pronounced in an electrified jet where the ratio of secondary to primary droplets is 30% more than that in the non-electrified jet. This follows

the idea that the electric field accelerates secondary breakup activity. Various parameters including the rotation rate, surface tension coefficient, and liquid viscosity affect the distance and time at which primary atomization begins.

It is interesting to analyze the number of droplets for each breakup level. While the final time chosen is arbitrary, it confirms the trend of atomization activity in the domain. Fig. 5.5 shows the number distribution of the droplets for each breakup level in the simulation. Although the dominant breakup level for both cases is the same (level 4), the electrified jet, which contains more droplets overall, also contains more droplets in deeper breakup levels.

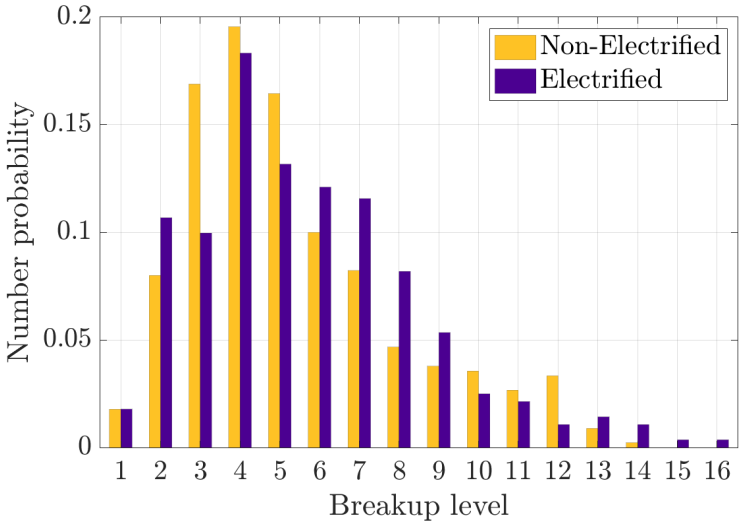



Figure 5.5: The number distribution of droplets that have undergone different breakups levels.

Droplet coalescence is a crucial process in atomizing flows. After 300 $\mu$s, the ratio of coalescence to breakup events in electrified operation (0.27) is 41% more than that in a non-electrified setup (0.19). It makes intuitive sense that more coalescence is observed in electrified setups because although the droplets are more spread out, the spray cloud contains more structures which in turn leads to more droplet collisions.

## 5.4 Droplet Size and Shape Evolution

The enhanced breakup activity in an electrified jet produces smaller droplets. The mean diameter of droplets in the spray cloud near the nozzle is about 4.5% smaller when operating in an electric field. Fig. 5.6 shows a comparison of the diameter distribution of droplets in the domain. A higher number of smaller liquid structures are created in an electrified jet due to the net reduction in effective surface tension in charged droplets.

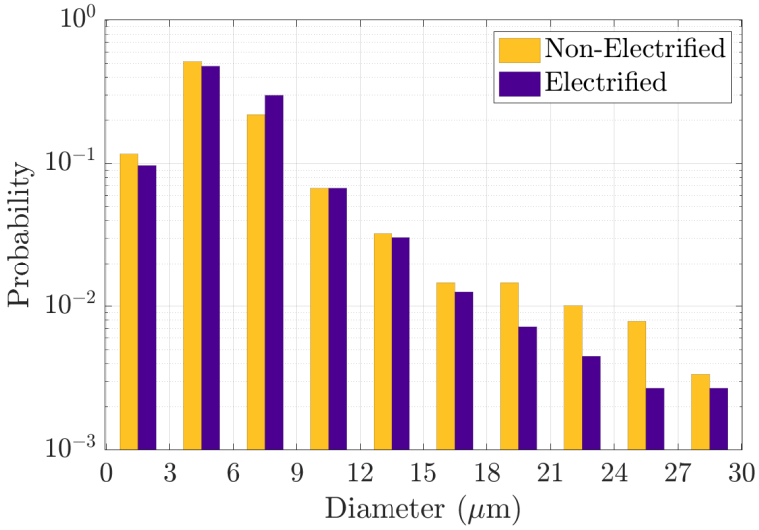



Figure 5.6: Droplet diameter distribution. Note the logarithmic scale on the $y$-axis.

Fig. 5.7 shows the comparison of the mean droplet diameters for each breakup level. A trend towards decreasing droplet sizes for deeper breakup levels is generally observed. Due to coalescence events, the droplet sizes may not strictly decrease between successive breakup levels.

Fig. 5.8 shows the mean change in diameter of droplets between successive breakup levels. The change in the size of droplets, which is the difference between the new and parent droplet diameters, decreases for deeper breakup levels due to the small sizes of the droplets themselves. The mean change in diameters across all breakup levels is about 18%

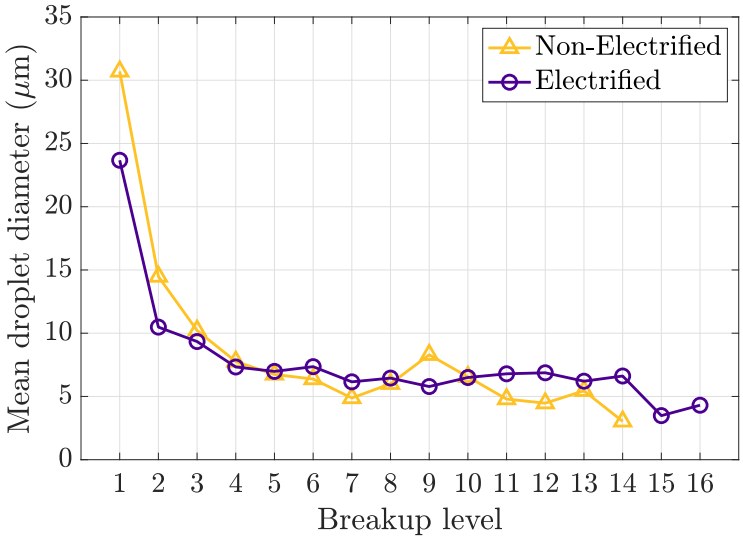



Figure 5.7: Mean droplet diameter for each breakup level.

lower in electrified jets. There are some instances where the change in diameter during a breakup event is a positive number. This is due to a coalescence event that occurred between two breakup events leading to an increase in its size. After breakup level 9, the mean change in diameter across breakup levels is seemingly constant for both cases. This is speculated to be due to a high ratio of coalescence to breakup events in this regime.

One way to quantify the shape of the resulting droplet is to examine its sphericity - a dimensionless quantity that represents the degree of departure from a perfect sphere. Mathematically, sphericity can be calculated as $A_1/A_3$, where $A_1 \geq A_2 \geq A_3$ are the lengths of the three principal axes of an ellipsoidal approximation of the droplet structure. A sphericity of 1, which is its lowest attainable value, indicates a perfect sphere, while larger values indicate irregular shapes. Fig. 5.9 shows a comparison of the sphericity distribution of droplets in the domain. The mean sphericity of all droplet structures is about 5% lower for the electrified droplets after 300 $\mu$s of the simulation, suggesting that they are more spherical in shape.

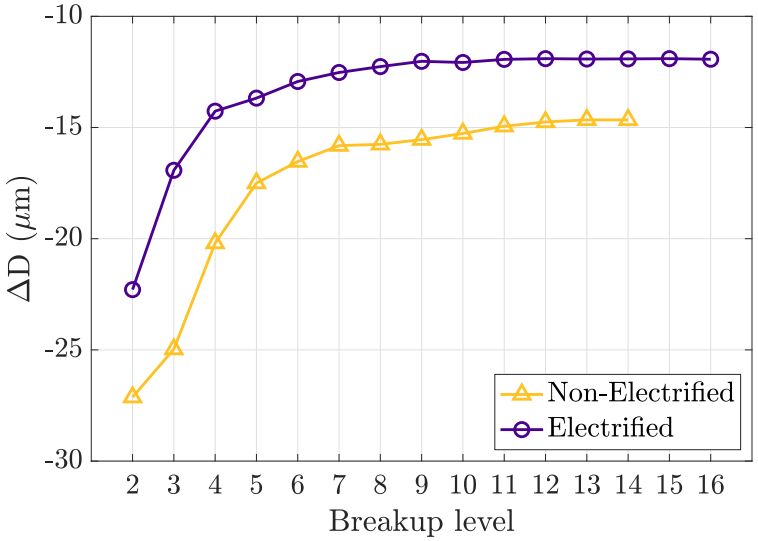



Figure 5.8: Mean change in droplet diameters for successive breakup levels. Here, breakup level 1 is omitted since it corresponds to breakup from the main ligament core.

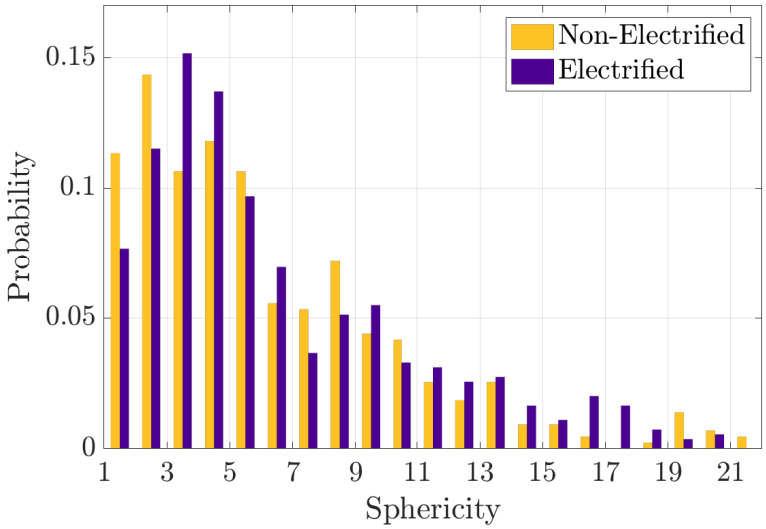



Figure 5.9: Droplet sphericity distribution.

## 5.5 Droplet Velocity Statistics

Analyzing the droplet velocities shows that during breakup, the mean absolute velocity of droplets in the electrified jet is about 3% lower than the non-electrified jet during breakup events. Fig. 5.10 shows that smaller droplets undergo breakup at lower velocities in the electrified jet due to the net reduction in the effective surface tension force. However, larger droplets undergo breakup at greater velocities in the electrified jet. This can be attributed to the presence of charges which imparts an electric force on large droplets. A similar trend is not evident in smaller droplets due to their small size and sensitivity to aerodynamic drag.

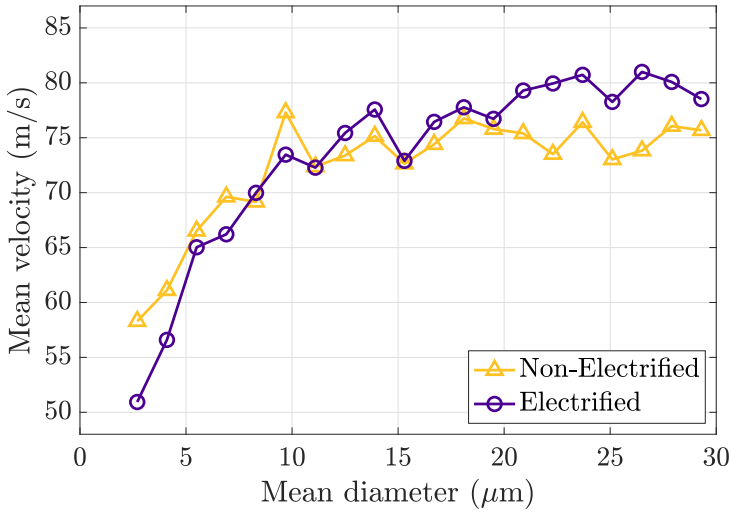



Figure 5.10: Comparing the mean velocity for different droplet sizes.

Additionally, the mean slip velocity magnitude, which is formulated as $|\mathbf{u}_{\text{liquid}} - \mathbf{u}_{\text{gas}}|$, is 16% higher in an electrified setup during breakup events. This suggests that charged droplets undergo breakup at higher slip velocities. Fig. 5.11 highlights that this is true across most droplets sizes. $|\mathbf{u}_{\text{liquid}}|$ is computed as the liquid volume weighted average velocity of cells corresponding to that structure while $|\mathbf{u}_{\text{gas}}|$ is computed as the gas volume weighted average velocity of cells neighboring the interfacial cells of that structure. It is important to note here that this method of calculating the slip velocity is a severe underestimation. Ideally,

the slip velocity is calculated as the local gas velocity without the influence of velocity of the structure itself. While its actual value is challenging to compute, our observation that its magnitude is higher in an electrified jet is a useful statistic which will be discussed in the next section.

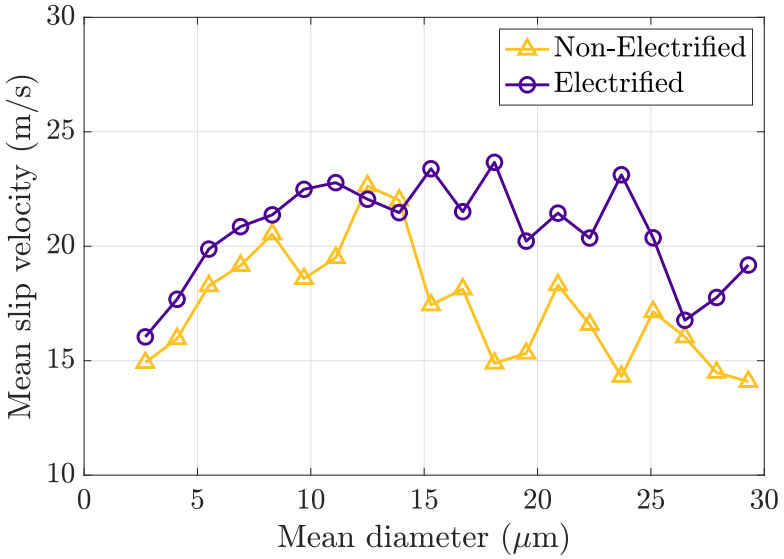



Figure 5.11: Comparing the mean slip velocity for different droplet sizes.

## 5.6 Local Weber Number Analysis

Using the ancestry extraction tool, the local flow field surrounding breakup events is analyzed and the local Weber number ($We_{\text{local}}$) is computed as

$$We_{\text{local}} = \frac{\rho_g U_s^2 L}{\gamma} \tag{5.1}$$

where $\rho_g$ is the gas density, $U_s$ is the slip velocity, $L$ is the characteristic length which is the equivalent spherical diameter of the droplet prior to breakup, and $\gamma$ is the surface tension coefficient. A more detailed explanation of this calculation is provided in Christensen and Owkes [31].

The $We_{\text{local}}$ distribution corresponding to structures prior to breakup is presented in Fig. 5.12. The mean Weber number for all breakup events is about 25% more in an electrified jet, which likely indicates that aerodynamic forces are more actively driving atomization in this system. This follows the findings of the slip velocity which was higher during breakup in electrified droplets. To reiterate, the slip velocity, which is severely underestimated, is squared in Eq. 5.1 to calculate the $We_{\text{local}}$. While the accurate value of $We_{\text{local}}$ is challenging to compute, the general trend that it is higher in electrified setups is a useful finding. Since the $We_{\text{local}}$ is severely underestimated in this formulation, there is sufficient reason to believe that atomization is driven by both aerodynamic breakup and instability growth and is enhanced in electrified setups by the electric force and the presence of charges in the liquid.

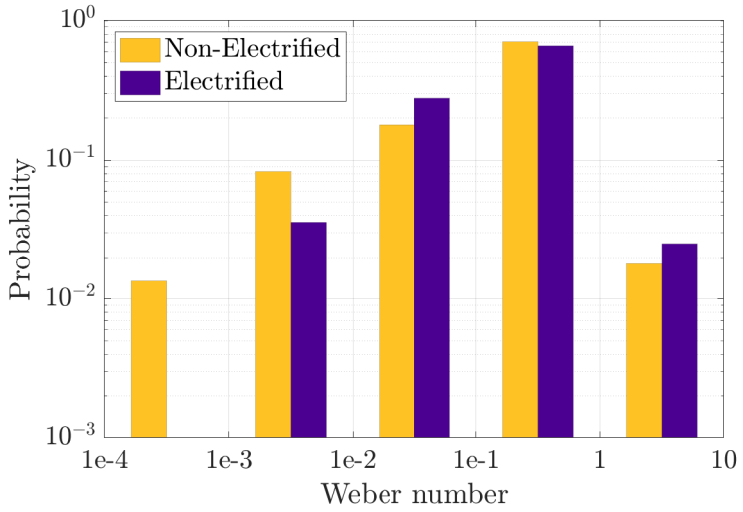



Figure 5.12: Local Weber number distribution associated with all structures. Note the logarithmic scale on the $y$-axis.

## 5.7 Charge Distribution Statistics

Most droplets contain a charge density that is very close to the initial bulk charging value of 2.879 C/m$^3$ (Fig. 5.13). However, since the process of charge migration is included in the model, we also see a distribution of charge densities in the droplets. Compared to the initial charge density (Table 3.1), it is more probable to find a droplet with a lower value of $q$. As charges relax towards the interface of the ligament, there is a localized reduction of $q$ in the bulk of the ligament. A majority of the liquid structures break off the ligament bulk (since a greater liquid volume is present in the bulk than near the interface) to form droplets that contain slightly lower values of $q$ than the initial bulk value. The moderate value of $\mathrm{Re}_e$ (Table 4.1) which is the ratio of the residence time of liquid in the domain to the charge relaxation timescale indicates that the charges have time to relax to some degree, but not enough time to fully relax to the surface. Higher resolution simulations can help better understand the charge relaxation process through the ligament core and the factors affecting the charge distribution in the spray cloud.

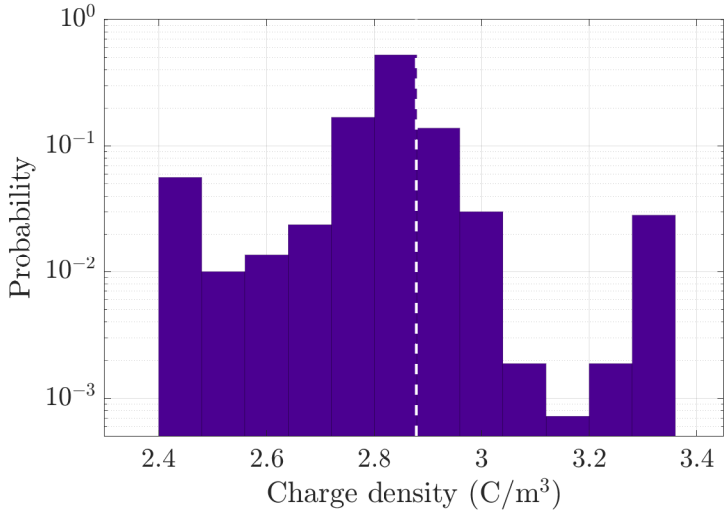



Figure 5.13: Number distribution of $q$ in liquid structres in the domain. The inital bulk value of $q$ is shown as a dashed line. Note the logarithmic scale on the $y$-axis.

Upon closer inspection of the charge distribution in droplets, it is evident that $q$ is generally higher in larger droplets (Fig. 5.14). This can be explained as follows - small droplets are more likely to be formed from the volume of liquid in the bulk of a ligament which, as discussed, contains a lower charge density. Larger droplets tend to break off as long primary ligaments from the main ligament core and therefore will not necessarily have a lower value of $q$.

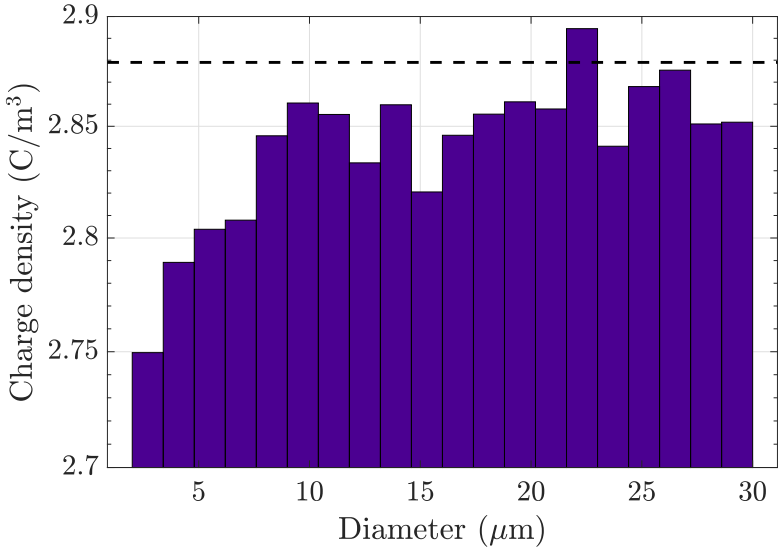



Figure 5.14: Mean $q$ in liquid structures of different sizes. The inital bulk value of $q$ is shown as a dashed line.

The change in $q$ ($\Delta q$) for successive breakup levels also shows a decreasing trend and approaches zero for the deepest breakup levels (Fig. 5.15). Naturally, the change in $q$ during a breakup event is inversely proportional to the change in the droplet sizes (Fig. 5.16).

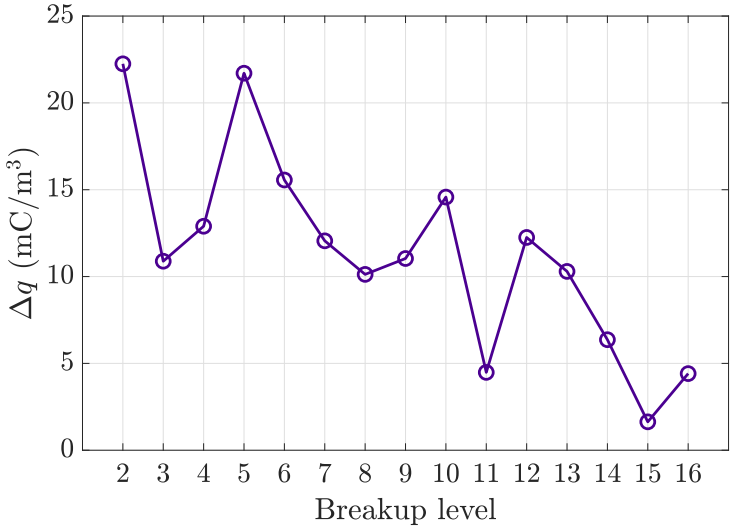



Figure 5.15: The mean change in $q$ between successive breakup levels.

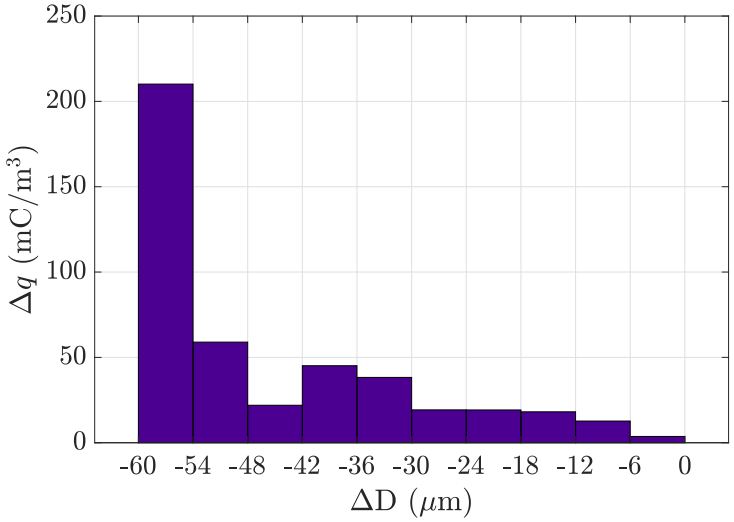



Figure 5.16: The mean change in $q$ corresponding to the change in diameter during a breakup event.

# CHAPTER SIX

# EFFECT OF SHEAR-THINNING FLOWS

In the interest of understanding breakup physics, a similar droplet ancestry focused study was conducted to isolate the effects of non-Newtonian flow behavior in the application of rotary atomization. The shear-thinning property of a fluid can significantly affect its atomization process. Deviations from the a uniform droplet size distribution and spray pattern may lead to reduced coating quality and efficiency [35]. It is important to understand the effects of non-Newtonian behavior on atomizing flows to achieve the desired coating thickness and surface finish quality. By isolating and understanding these effects, more reliable models can be developed to the predict optimal operation of rotary atomizers. Two simulations are performed - one with a Newtonian liquid and one with a non-Newtonian, particularly shear-thinning liquid - in a domain as described in Chapter 3 with parameter values listed in Table 3.1. However, both simulations are conducted in the absence of a background electric field and zero liquid charge density. The two simulations are identical except that the former has a constant liquid viscosity of 0.1 Pa.s. The goal of this study is to isolate and understand non-Newtonian flow effects on the breakup mechanisms. For brevity, only the notable inferences are presented in this section.

## 6.1 Liquid Interface

Fig. 6.1 shows the positions of the liquid interface of the jet at different instances in time as viewed on an $x$-$y$ plane. The sprays look visually similar except for the jet penetration. A detailed comparison based on the extracted statistics follows.

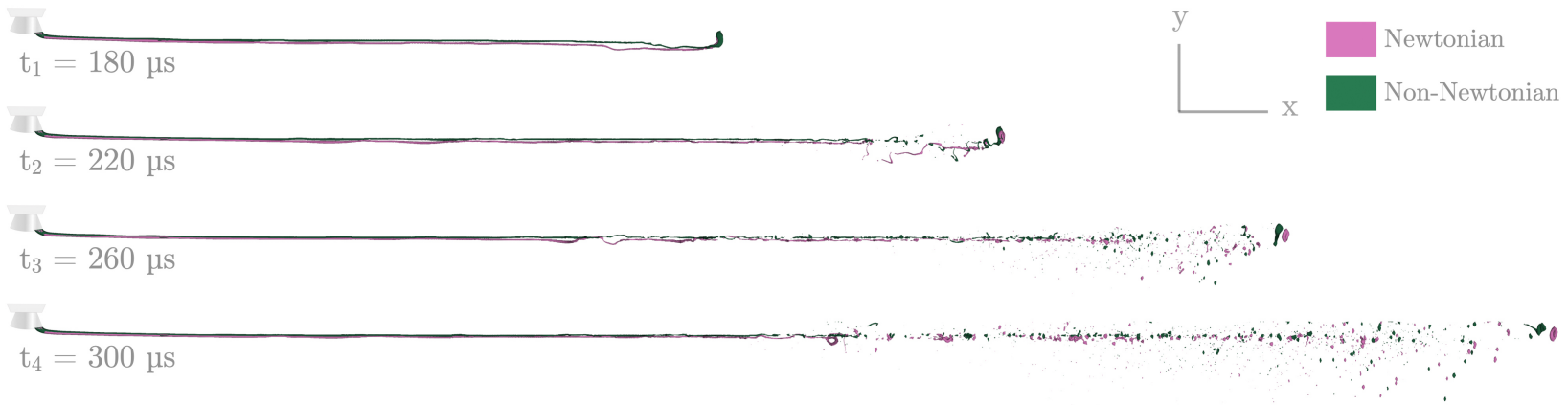



Figure 6.1: Liquid interface positions of a Newtonian (pink) and a non-Newtonian (green) jet at different times as viewed from an $x$-$y$ plane. The nozzle is shown for reference at the top left corner and is not to scale.

## 6.2 Atomization Characteristics

The droplet ancestry statistics extraction tool described in Section 3.4 is employed to extract several atomization statistics related to the droplet size, shape, velocity, and charge density can be extracted and analyzed to gain insights into the effect of shear-thinning behavior of liquid on the atomization process in RBAs. The results are compiled after analyzing 796 liquid structures in the Newtonian domain and 897 liquid structures in the non-Newtonian setup.

Fig. 6.2 shows the time evolution of the number of liquid structures in the domain. The non-Newtonian jet seemingly undergoes breakup sooner and contains 12% more droplets than the Newtonian jet. While secondary atomization is still the dominant regime for breakup, the ratio of secondary to primary droplets in the Newtonian jet is 23% more than that in the non-Newtonian jet.

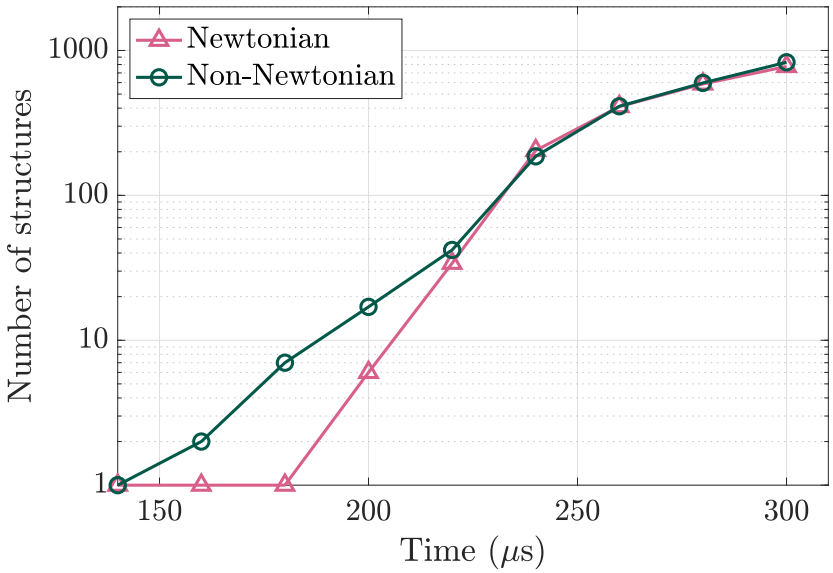



Figure 6.2: The total number of droplets in the domain over time in Newtonian (pink) and non-Newtonian (green) operating conditions in the first 300 $\mu$s of the near-bell atomization simulation. Note the logarithmic scale on the $y$-axis.

The non-Newtonian jet has an effectively larger value of viscosity since it's the same at

high shear rates, but larger at low shear rates. Therefore, the higher viscosity at low shear rates seemingly suppresses instabilities that cause secondary atomization. However, the initial breakup occurs sooner in the non-Newtonian case indicating that the higher viscosity has the opposite effect on primary atomization.

Fig. 6.3 shows the number distribution of the droplets for each breakup level in the simulation. Although the dominant breakup level for both cases is the same (level 4), the non-Newtonian jet, which contains more droplets overall, has a smaller spread in terms of the number distribution of droplets across breakup levels. The deepest breakup level in the Newtonian jet is 18 while it is only 14 for the non-Newtonian case. This further supports the idea that the shear-thinning behavior of the liquid is suppressing secondary atomization. After 300 $\mu$s, the ratio of coalescence to breakup events in the non-Newtonian setup is 8% more than that in the Newtonian case suggesting that more coalescence events occur in the non-Newtonian perhaps due to the increased number of droplets in the domain.

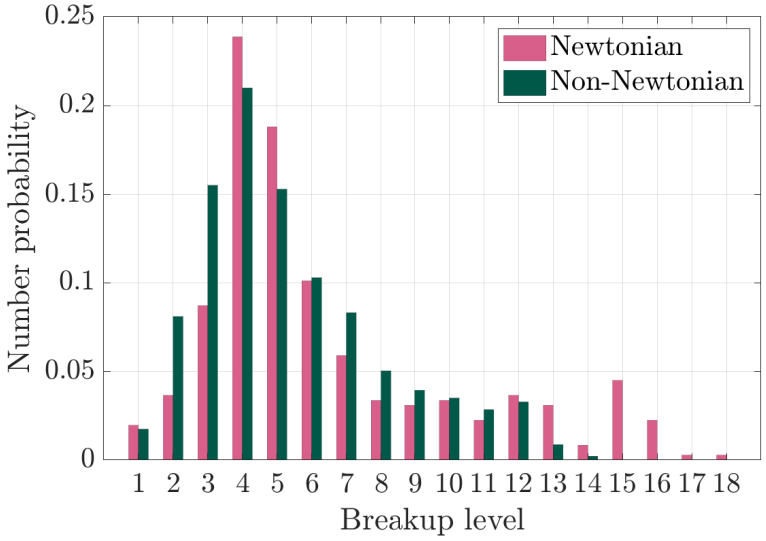



Figure 6.3: The number distribution of droplets that have undergone different breakups levels in Newtonian (pink) and non-Newtonian (green) operating conditions in the first 300 $\mu$s of the near-bell atomization simulation.

## 6.3 Droplet Size Evolution

Fig. 6.4 shows a comparison of the statistically similar diameter distribution of droplets in the domain and the similarity is evident. This indicates that the viscosity does not have a significant impact on the drop size distribution. The drop sizes are likely affected mainly by the aerodynamic and surface tension forces, and not the flow within the liquid. Fig. 6.5 shows the comparison of the mean droplet diameters for each breakup level. Naturally, a trend towards decreasing droplet sizes for deeper breakup levels is observed. However, discrepancies in the behavior between the two cases is non-evident, reiterating that viscosity is not playing a large role in the drop sizes. Fig. 6.6 shows the mean change in diameter of droplets between successive breakup levels. The change in the size of droplets decreases for deeper breakup levels due to the small sizes of the droplets themselves. Sometimes, positive diameter changes are measured due to coalescence events, which increases the droplet size. Interestingly, the non-Newtonian jet has a larger magnitude of the mean change in diameters across all breakup levels.

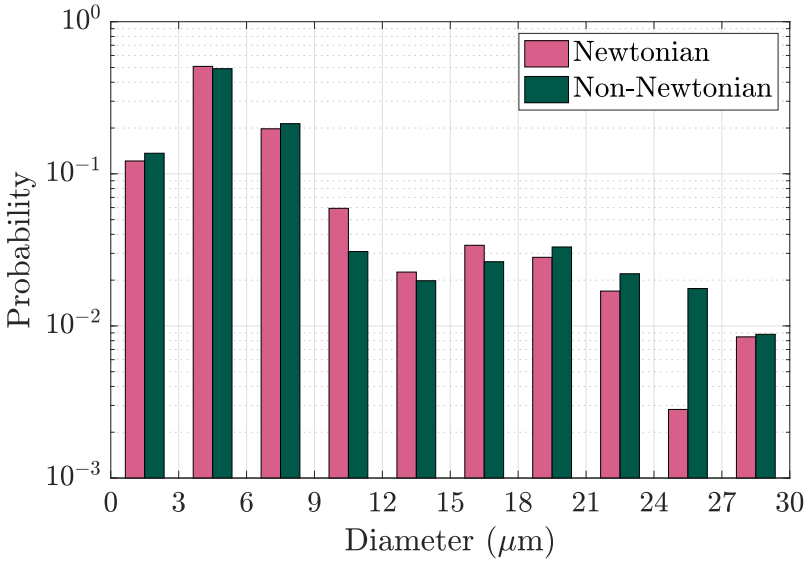



Figure 6.4: Droplet diameter distribution in the simulation.

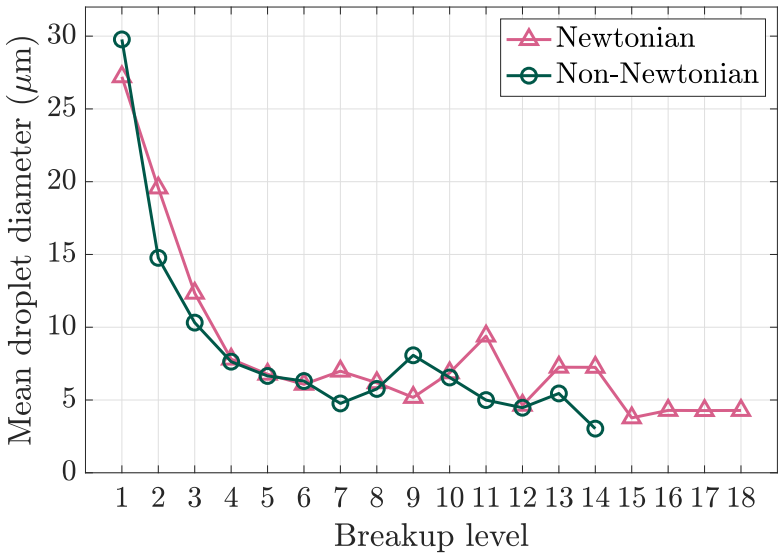



Figure 6.5: Mean droplet diameter for each breakup level in the simulation.

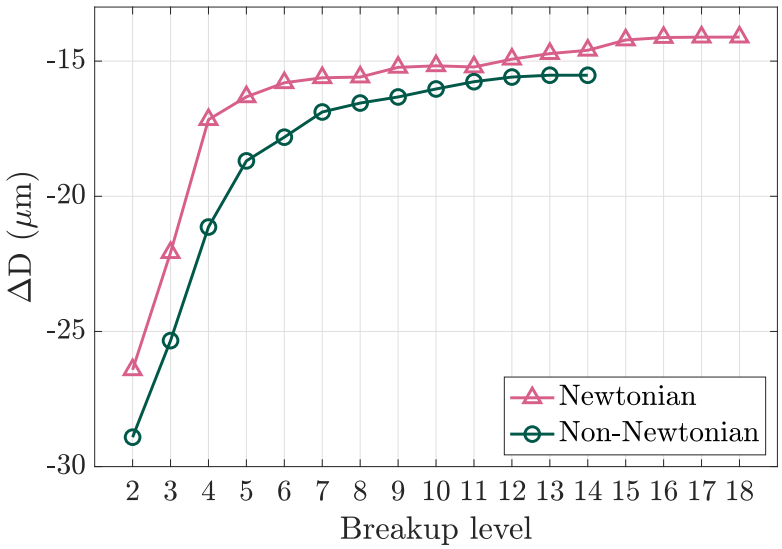



Figure 6.6: Mean change in droplet diameters for successive breakup levels. Here, breakup level 1 is omitted since it corresponds to breakup from the main ligament core.

## 6.4 Viscosity Characteristics

Figure 6.7 highlights that the viscosity in an overwhelming majority of the droplets is very close to the viscosity value for an infinite shear rate which is approximately 0.111 Pa.s (Fig. 2.1). Higher resolution simulations can help better understand the viscosity distribution within the ligament core and the individual droplet structures.

The mean viscosity also shows a decreasing trend during breakup into deeper breakup levels (Fig. 6.8) which suggests that droplets breaking off at deeper breakup levels experience higher shear rates. Consequentially, upon closer inspection of the viscosity in droplets, it is evident that larger droplets are likely to have a higher viscosity value (Fig. 6.9). This is speculated to be due to the fact that larger droplets undergo higher shear by virtue of their higher surface area, whereas small droplets move with the gas flow. The mean viscosity in droplets during breakup increases with the local Weber number (Fig. 6.10). The change in viscosity during breakup for successive breakup levels also shows a decreasing trend and approaches zero for the deepest breakup levels (Fig. 6.11).

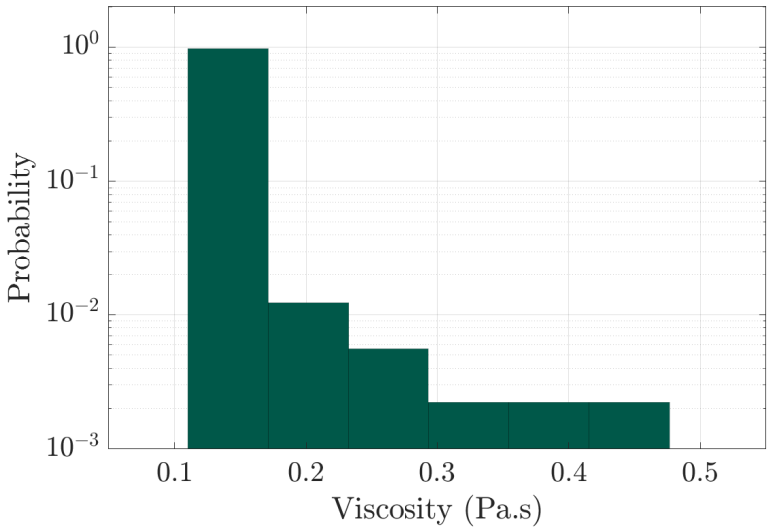



Figure 6.7: Liquid viscosity distribution during breakup events in the first 300 $\mu$s of the simulation.

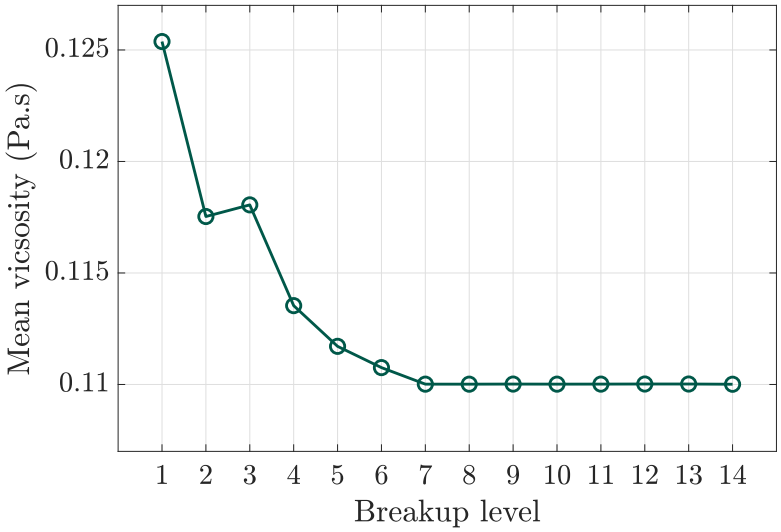



Figure 6.8: Mean viscosity of the parent droplets for each breakup level.

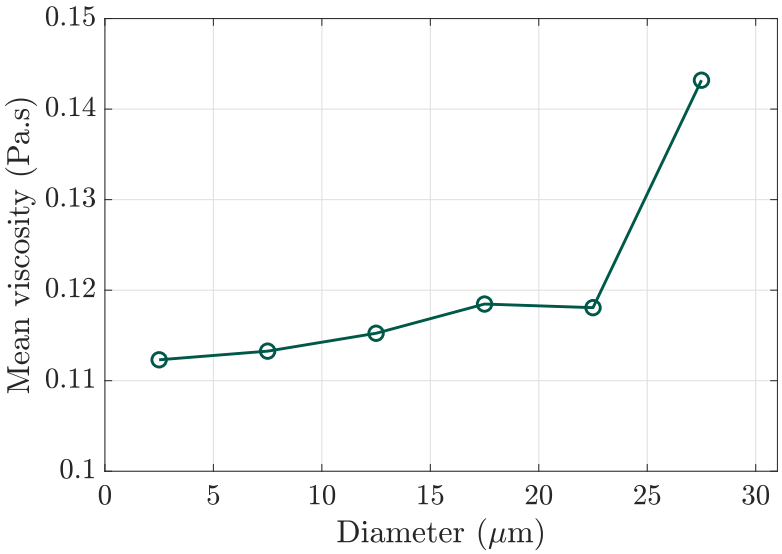



Figure 6.9: Mean viscosity of the parent droplets as a function of droplet sizes.

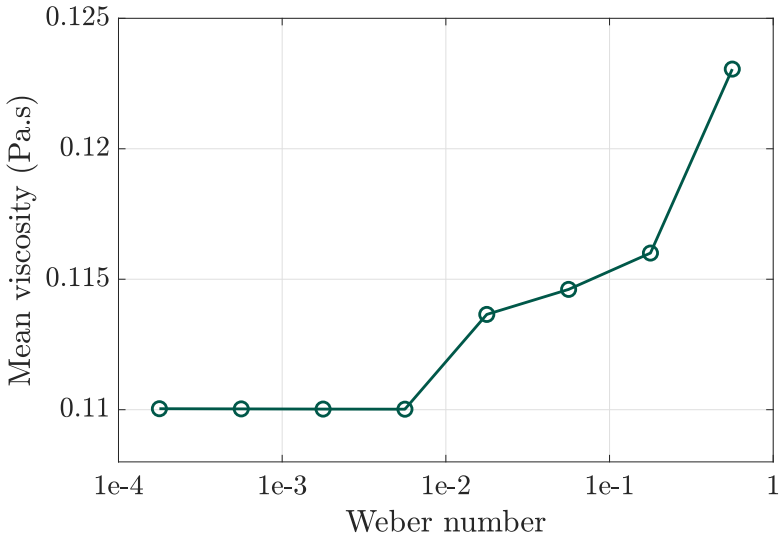



Figure 6.10: Comparing liquid viscosity for a range of local Weber numbers during breakup events in the first 300 $\mu$s of the simulation.

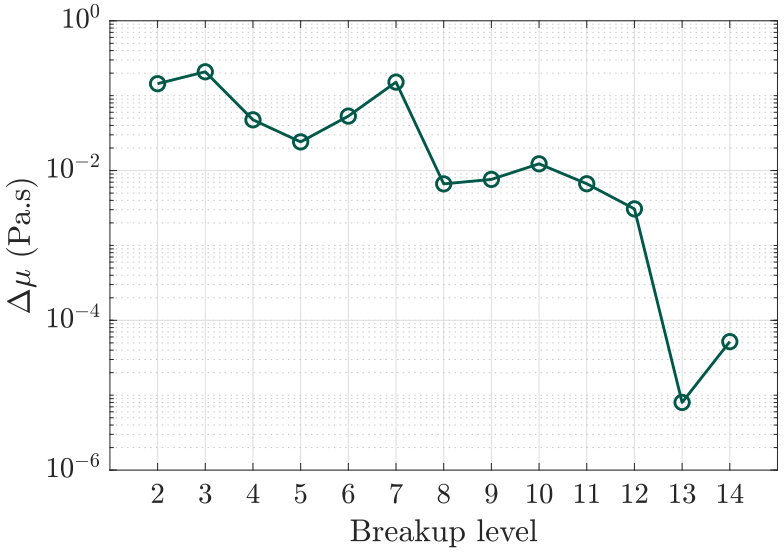



Figure 6.11: The mean change in liquid viscosity between successive breakup levels.

# CHAPTER SEVEN

## CONCLUSIONS AND OUTLOOK

This dissertation contains a detailed discussion regarding the use of numerical methods to simulate and study gas-liquid multiphase flows, particularly atomizing flows in industrial applications. A device called the electrostatic rotary bell atomizer (ERBA) is simulated in this work. ERBAs are popular atomizing devices used in various industries, including automotive painting. Multiple complex physical processes influence the mechanisms driving atomization in the device. The simulations are characterized by an interesting set of physical models -

1. The multiphase gas-liquid flow is modeled using the Navier-Stokes equations, a surface tension force formulation and an interface tracking scheme.
2. The non-Newtonian flow is formulated using a modified power law fit on empirical viscosity values corresponding to shear-thinning automotive paints.
3. The rotating flow is modeled using the centrifugal and Coriolis forces.
4. The electrohydrodynamic processes are formulated using a set of governing equations describing the electric force, electric field, electric potential field, and charge transport (advection, diffusion, and migration). An auxiliary domain called e-Mesh is used exclusively as an electric potential field solver to obtain accurate boundary conditions of electric potential on the flow domain.

Notably, a multi-physics based approach has been incorporated in this work to accurately model the complex atomizing flows in ERBAs.

## 7.1 Atomization Characteristics in Rotary Atomization

In this work, high-fidelity simulations are performed using a numerical model developed to simulate electrohydrodynamic atomization in ERBAs. The simulations are equipped with a droplet ancestry extraction tool that stores droplet and local flow statistics. The extracted statistics are analyzed to provide insights into the breakup mechanisms in an ERBA. This is a cost-effective method to understand atomization and extract information that is challenging to obtain experimentally.

It is found that the presence of the electric field increases jet penetration, spray angle, and droplet spacing due to the effect of the electric force that acts along the radially outward direction. However, the breakup length and the first instance of breakup in time are longer in the electrified jet due to a stabilizing force provided by the electric field on the charged ligament core. However, once breakup begins, the net reduction in the effective surface tension in liquid structures due to the presence of charges accelerates the breakup process leading enhanced secondary atomization in the electrified jet. The total number of droplets, the ratio of secondary to primary droplets, and the ratio of coalescence to breakup activity are all higher when operating in an electric field. Charged droplets seem to undergo breakup at higher slip velocities than uncharged droplets. Most charged droplets contain a charge density that is very close to the initial bulk charging value. While larger droplets generally contain a higher value of charge density, it is more probable to find droplets with charge density values lower than the initial bulk value.

In a separate study conducted in a non-electrified setup to identify the effect of the shear-thinning behavior of liquid paints, it was found that viscosity does not have a significant impact on the drop size distribution. The drop sizes are likely affected mainly by the aerodynamic and surface tension forces. The higher viscosity at low shear rates seemingly suppresses instabilities that cause secondary atomization. However, the initial breakup

occurs sooner in the non-Newtonian case indicating that the higher viscosity has the opposite effect on primary atomization.

## 7.2 Impact of Research Work

Accurate simulations of multiphase flows in engineering applications involving multiple physical phenomena can help create a significant impact on our understanding and the optimization of the processes. Simulations will allow researchers to isolate certain aspects of the flow and identify their effects on the relevant metrics. Simulations also help visualize and measure flows in ways arguably impossible with current experimental methods. In this work, information which is inaccessible to experimental techniques near the bell edge and within the dense droplet cloud has been extracted and analyzed to study the behavior of charged droplets under the influence of a background electric field. Small improvements to the performance of this device can have significant financial and environmental benefits. The findings of this work can help manufacturers choose optimal operating conditions of ERBAs more carefully.

## 7.3 Future Work

The numerical formulation and methodology presented in this dissertation provide a framework that can predict the atomization process in near-bell ERBA flows. However, some aspects in framework and the numerical setup that could benefit from improvements or inclusions are listed below.

1. A parameter study can be conducted to investigate the effect of various operating parameters on the physics of the atomization process.
   (a) The rotation rate strongly affects the droplet size distribution, spray cone angle, and surface coverage.

(b) The flow rate affects the droplet size distribution and the coating thickness.

(c) Liquid viscosity plays an important role in the physics of atomization in how it governs the resistance of flow to shear in atomizing flows. Higher viscosity fluids may have reduced spray coverage and penetration compared to lower viscosity fluids. Liquid viscosity can also impact the surface wetting and coating uniformity.

(d) As seen from the work done in this thesis, the liquid charge density and background electric potential can have a significant impact on the atomization quality in multiple ways.

(e) The size of the bell cup and its distance from target surface can affect the spray pattern in certain regimes of operating conditions.

2. In this work, liquid was injected into the domain through an ellipsoidal inflow with a velocity profile that corresponds to the edge angle of the bell. However, in practice, a thin film of liquid flows out of a flat/serrated bell edge in a more complex way to form ligaments.

   (a) It would be more accurate to simulate a film flowing through serrations at the bell edge instead of modeling an ellipsoidal inflow.

   (b) Different serration geometries and widths can be simulated to better understand the relationship between droplet sizes and bell edge geometries.

   (c) In a bell without serrations, sheet breakup is the primary mode of atomization. There exist formulations currently that can model sheet breakup for atomizing flows. It would be interesting to explore this mode of breakup in ERBAs.

3. The initial charge distribution was assumed to be uniform through the liquid bulk in this work. However, it would be worth exploring a more practical way to impart charge into the liquid phase to improve the accuracy of the predicted atomizing flows [3, 30, 109]. There are two ways of charging paint before it exits the nozzle - 1) direct charging - where the liquid is charged by applying high voltage directly to the rotating

bell of the atomizer [44], and 2) external charging - where droplets are charged using external high voltage emitting electrode needles due to free ions produced from corona discharge at the electrodes [2].

4. A "future work" section in a CFD-based research document is incomplete without the mention of potentially performing simulations on a finer mesh. Higher resolution studies will shed more light on the process of charge redistribution through the ligament core and within the droplet structures.
5. While it is well-known that the presence of charges in a droplet reduces its effective surface tension, a quantitative analysis will be useful. In theory, the electric field, which generates an electrostatic pressure at the interface, alters the distribution of the surface charges and affects the surface tension force. An inclusion to the statistics being extracted could be the electric field magnitude in each structure. This value can be used to compute the electrostatic pressure which can help quantify the effective reduction in the surface tension force due to the presence of charges in the droplets.
6. A feature commonly found in ERBA setups is the shaping air system which is used as a secondary air stream to shape and control the spray pattern. It will be worth performing simulations that include a shaping air setup to make the tool more robust in simulating industrial applications of the device.
7. As an extension to this work, a Lagrangian droplet spray model can be implemented for droplets that do not undergo any further breakup. Once such droplets are identified using appropriate breakup models, the Lagrangian droplet spray model can predict the droplet trajectories, interaction with airflow, and the deposition pattern. In the proposed model, each droplet would be treated as a discrete particle with its own position, velocity, charge and other relevant properties. A strong advantage to this reduced physics model is the elimination of the necessity to solve expensive pressure and electric Poisson equations and focus only on the centrifugal, Coriolis, aerodynamic drag

and electric forces on each discrete droplet structure. Moreover, it would enable the tool to completely model the spraying process from high-fidelity injection to deposition on the target surface - which would make it the first of its kind.

# REFERENCES CITED

[1] The influence of air and liquid properties on airblast atomization. *Journal of Fluids Engineering-transactions of the ASME*, 97(3):316–320, 1975.

[2] The simulation of electrostatic spray painting process with high-speed rotary bell atomizers. part ii: External charging. *Particle & Particle Systems Characterization*, 23(5):408–416, 2006.

[3] Effects of electrode voltage, liquid flow rate, and liquid properties on spray chargeability of an air-assisted electrostatic-induction spray-charging system. *Journal of Electrostatics*, 68(2):152–158, 2010.

[4] *Direct Numerical Simulations of Gas-Liquid Multiphase Flows*. 2011.

[5] Michael B Abbott and David R Basco. *Computational fluid dynamics*. Longman Scientific & Technical Harlow, Essex, 1989.

[6] J. Abu-Ali and S.A. Barringer. Method for electrostatic atomization of emulsions in an ehd system. *Journal of Electrostatics*, 63(5):361–369, 2005.

[7] Adnan Darwish Ahmad, Binit B. Singh, Mark Doerre, Ahmad M. Abubaker, Masoud Arabghahestani, Ahmad A. Salaimeh, and Nelson K. Akafuah. Spatial positioning and operating parameters of a rotary bell sprayer: 3D mapping of droplet size distributions. *Fluids*, 4(3), 2019. ISSN 23115521.

[8] N. K. Akafuah, Kimio Toda, Abraham Salazar, and Kozo Saito. *Automotive Paint Spray Characterization and Visualization*, pages 121–165. Springer Netherlands, Dordrecht, 2013.

[9] Nelson Akafuah, Sadegh Poozesh, Ahmad Salaimeh, Gabriela Patrick, Kevin Lawler, and Kozo Saito. Evolution of the Automotive Body Coating Process — A Review. *Coatings*, 6(2), 2016. ISSN 2079-6412.

[10] Abdullah Alotaibi, Mohmoud Awad, and Ahmed Hamed. Performance of air conditioning system using air cooled condenser with water atomization. *International Journal of Engineering Research and Science and Technology*, 4(1):127–135, 2015.

[11] John David Anderson and John Wendt. *Computational fluid dynamics*, volume 206. Springer, 1995.

[12] Björn Andersson, Valeri Golovitchev, Stefan Jakobsson, Andreas Mark, Fredrik Edelvik, Lars Davidson, and Johan S Carlson. A modified tab model for simulation of atomization in rotary bell spray painting. *Journal of Mechanical Engineering and Automation*, 3(2):54–61, 2013.

[13] Ricardo D Andrade, Olivier Skurtys, and Fernando A Osorio. Atomizing spray systems for application of edible coatings. *Comprehensive Reviews in Food Science and Food Safety*, 11(3):323–337, 2012.

[14] T. Anukiruthika, J.A. Moses, and C. Anandharamakrishnan. Electrohydrodynamic drying of foods: Principle, applications, and prospects. *Journal of Food Engineering*, 295:110449, 2021. ISSN 0260-8774.

[15] ZM Anwar, Ee Sann Tan, R Adnan, and Mohd Azree Idris. Study on atomization characteristics for power generation application. In *IOP Conference Series: Earth and Environmental Science*, volume 16, page 012016. IOP Publishing, 2013.

[16] Pooya Azizian, Milad Azarmanesh, Morteza Dejam, Mehdi Mohammadi, Milad Shamsi, Amir Sanati-Nezhad, and Abdulmajeed A. Mohamad. Electrohydrodynamic formation of single and double emulsions for low interfacial tension multiphase systems within microfluidics. *Chemical Engineering Science*, 195:201–207, 2019. ISSN 0009-2509.

[17] WD Bachalo. Experimental methods in multiphase flows. *International journal of multiphase flow*, 20:261–295, 1994.

[18] Adrian G. Bailey. Electrostatic atomization of liquids. *Science Progress (1933- )*, 61 (244):555–581, 1974. ISSN 00368504, 20477163.

[19] S Balachandar and John K Eaton. Turbulent dispersed multiphase flow. *Annual review of fluid mechanics*, 42:111–133, 2010.

[20] W. Balachandran and A. G. Bailey. The Dispersion of Liquids Using Centrifugal and Electrostatic Forces. *IEEE Transactions on Industry Applications*, IA-20(3):682–686, 1984.

[21] Marcos AS Barrozo, Claudio R Duarte, Norman Epstein, John R Grace, and C Jim Lim. Experimental and computational fluid dynamics study of dense-phase, transition region, and dilute-phase spouting. *Industrial & Engineering Chemistry Research*, 49 (11):5102–5109, 2010.

[22] Jean Berthier and Kenneth A Brakke. *The physics of microdroplets*. John Wiley & Sons, 2012.

[23] Darshak K. Bhuptani and Sarith P. Sathian. Effect of axial electric field on the Rayleigh instability at small length scales. *Physical review. E*, 95(5-1):053115, may 2017. ISSN 24700053.

[24] G. Blanquart, P. Pepiot-Desjardins, and H. Pitsch. Chemical mechanism for high temperature combustion of engine relevant fuels with emphasis on soot precursors. *Combustion and Flame*, 156(3):588–607, 2009. ISSN 00102180.

[25] Victor Boniou, Thomas Schmitt, and Aymeric Vié. Comparison of interface capturing methods for the simulation of two-phase flow in a unified low-mach framework. *International Journal of Multiphase Flow*, 149:103957, 2022.

[26] JP Brill and SJ Arirachakaran. State of the art in multiphase flow. *Journal of Petroleum Technology*, 44(05):538–541, 1992.

[27] Antonio Castellanos. Electrospray and atomization. In *Electrohydrodynamics*, pages 206–212. Springer, 1998.

[28] Fang Chen and Hans Hagen. A survey of interface tracking methods in multi-phase fluid visualization. In *Visualization of Large and Unstructured Data Sets-Applications in Geospatial Planning, Modeling and Engineering (IRTG 1131 Workshop)*. Schloss Dagstuhl-Leibniz-Zentrum fuer Informatik, 2011.

[29] Zhangxin Chen, Guanren Huan, and Yuanle Ma. *Computational methods for multiphase flows in porous media*. SIAM, 2006.

[30] F Chowdhury, M Ray, A Sowinski, P Mehrani, and A Passalacqua. A review on modeling approaches for the electrostatic charging of particles. *Powder Technology*, 389:104–118, 2021.

[31] Brendan Christensen and Mark Owkes. Efficient extraction of atomization processes from high-fidelity simulations. *Computers & Fluids*, 254:105808, 2023. ISSN 0045-7930.

[32] Zémerli Clément, Edelvik Fredrik, Mark Andreas, and Hermanns Oliver. Efficient Numerical Simulation of Spray Painting Processes in Automotive Manufacturing. In *23rd SAE Brasil International Congress and Display*. SAE Technical Paper, 2014.

[33] S. A. Colbert and R. A. Cairncross. A computer simulation for predicting electrostatic spray coating patterns. *Powder Technology*, 151:77–86, 2005. ISSN 0032-5910.

[34] Steven Anthony Colbert. *Numerical simulations of droplet trajectories from an electrostatic rotary-bell atomizer*. PhD thesis, Drexel University, 2007.

[35] P. L. Corbeels, Dwight W. Senser, and Arthur H. Lefebvre. Atomization Characteristics of a high speed rotary-bell paint applicator. *Atomization and Sprays*, 2(2):87–99, 1992. ISSN 1044-5110.

[36] Ian P. Craig, Andrew Hewitt, and Howard Terry. Rotary atomiser design requirements for optimum pesticide application efficiency. *Crop Protection*, 66:34–39, 2014. ISSN 0261-2194.

[37] Joseph M. Crowley. *Fundamentals of applied electrostatics*, volume 1. Wiley, 1st edition, 1986.

[38] ZG Deng, Rui Xiao, BS Jin, QL Song, and He Huang. Multiphase cfd modeling for a chemical looping combustion process (fuel reactor). *Chemical Engineering & Technology: Industrial Chemistry-Plant Equipment-Process Engineering-Biotechnology*, 31 (12):1754–1766, 2008.

[39] Olivier Desjardins, Guillaume Blanquart, Guillaume Balarac, and Heinz Pitsch. High order conservative finite difference scheme for variable density low mach number turbulent flows. *Journal of Computational Physics*, 227:7125–7159, 2008. ISSN 0021-9991.

[40] Olivier Desjardins, Vincent Moureau, and Heinz Pitsch. An accurate conservative level set/ghost fluid method for simulating turbulent atomization. *Journal of Computational Physics*, 227:8395–8416, 2008. ISSN 0021-9991.

[41] N. Dombrowski and T.L. Lloyd. Atomisation of liquids by spinning cups. *The Chemical Engineering Journal*, 8(1):63–81, 1974. ISSN 0300-9467.

[42] Joachim Domnick. Effect of Bell Geometry in High-Speed Rotary Bell Atomization. 2010.

[43] Joachim Domnick and M. Thieme. Atomization Characteristics of High-Speed Rotary Bell Atomizers. *Atomization and Sprays*, 16(8):857–874, 2006. ISSN 1044-5110.

[44] Joachim Domnick, Andreas Scheibe, and Qiaoyan Ye. The Simulation of the Electrostatic Spray Painting Process with High-Speed Rotary Bell Atomizers. Part I: Direct Charging. *Particle & Particle Systems Characterization*, 22(2):141–150, 2005.

[45] Joachim Domnick, Z. Yang, and Q. Ye. Simulation of the film formation at a high-speed rotary bell atomizer used in automotive spray painting processes. 2008.

[46] Peter A. M. Eagles, Amer N. Qureshi, and Suwan N. Jayasinghe. Electrohydrodynamic jetting of mouse neuronal cells. *Biochemical Journal*, 394(2):375–378, 02 2006. ISSN 0264-6021.

[47] MM Elkotb. Fuel atomization for spray modelling. *Progress in Energy and Combustion Science*, 8(1):61–91, 1982.

[48] Kevin R.J. Ellwood and J. Braslaw. A finite-element model for an electrostatic bell sprayer. *Journal of Electrostatics*, 45(1):1–23, 1998. ISSN 03043886.

[49] Kevin R.J. Ellwood, Janice L. Tardiff, and Seyed M. Alaie. A simplified analysis method for correlating rotary atomizer performance on droplet size and coating appearance. *Journal of Coatings Technology and Research*, 11(3):303–309, 2014. ISSN 15470091.

[50] Marjan Enayati, Ming-Wei Chang, Felix Bragman, Mohan Edirisinghe, and Eleanor Stride. Electrohydrodynamic preparation of particles, capsules and bubbles for biomedical engineering applications. *Colloids and Surfaces A: Physicochemical and Engineering Aspects*, 382(1-3):154–164, 2011.

[51] R D Falgout, J E Jones, and U M. Yang. *Pursuing Scalability for hypre's Conceptual Interfaces*. Lawrence Livermore National Laboratory, 2004.

[52] Robert D. Falgout, Jim E. Jones, and Ulrike Meier Yang. The design and implementation of hypre, a library of parallel high performance preconditioners. In *Numerical Solution of Partial Differential Equations on Parallel Computers*, pages 267–294. Springer Berlin Heidelberg, 2006.

[53] Hua-Tzu Fan, Harry Kuo, and Joseph Simmer. Measuring paint droplet size, velocity, and charge-to-mass ratio distribution for electrostatic rotary bell spray simulation. In *ASME International Mechanical Engineering Congress and Exposition*, volume 54921, pages 703–709, 2011.

[54] U. Farook, E. Stride, M. J. Edirisinghe, and R. Moaleji. Microbubbling by co-axial electrohydrodynamic atomization. *Medical & Biological Engineering & Computing*, 45 (8):781–789, 2007.

[55] Ronald P Fedkiw, Tariq Aslam, Barry Merriman, and Stanley Osher. A non-oscillatory eulerian approach to interfaces in multimaterial flows (the ghost fluid method). *Journal of computational physics*, 152(2):457–492, 1999.

[56] John B Fenn, Matthias Mann, Chin Kai Meng, Shek Fu Wong, and Craig M Whitehouse. Electrospray ionization for mass spectrometry of large biomolecules. *Science*, 246(4926):64–71, 1989.

[57] Daniel Fredrich, Erik Weiand, and Andrea Giusti. Electrostatic fields for the control of evaporating charged fuel sprays. *International Journal of Multiphase Flow*, page 104312, 2022. ISSN 03019322.

[58] A. R. Frost. Rotary atomization in the ligament formation mode. *Journal of Agricultural Engineering Research*, 26:63–78, 1981. ISSN 0021-8634.

[59] C. Galitsky and E. Worrel. Energy Efficiency Improvement and Cost Saving Opportunities for the Vehicle Assembly Industry: An Energy Star Guide for Energy and Plant Managers. Technical report, Lawrence Berkeley National Laboratory, University of California: Berkeley, CA, USA, December 2008.

[60] CA Geffen and S Rothenberg. Suppliers and environmental innovation: the automotive paint process. *International Journal of Operations and Production Management*, 2000.

[61] Anisha V Gorty and Sheryl A Barringer. Electrohydrodynamic spraying of chocolate. *Journal of Food Processing and Preservation*, 35(4):542–549, 2011.

[62] J.M. Grace and J.C.M. Marijnissen. A review of liquid atomization by electrical means. *Journal of Aerosol Science*, 25(6):1005–1019, 1994. ISSN 0021-8502.

[63] Holger Grosshans and Miltiadis V Papalexandris. A model for the non-uniform contact charging of particles. *Powder Technology*, 305:518–527, 2017.

[64] Nico Guettler, Philipp Knee, Qiaoyan Ye, and Oliver Tiedje. Initial droplet conditions in numerical spray painting by electrostatic rotary bell sprayers: A framework for optimization of injection model coefficients. *Journal of Coatings Technology and Research*, 17(5):1091–1104, 2020.

[65] Lutz Gödeke, Walter Oswald, Norbert Willenbacher, and Peter Ehrhard. Dimensional analysis of droplet size and ligament length during high-speed rotary bell atomization. *Journal of Coatings Technology and Research*, 18:75–81, 2021. ISSN 1935-3804.

[66] I. Hayati, A. I. Bailey, and Th. F. Tadros. Mechanism of stable jet formation in electrohydrodynamic atomization. *Nature*, 319(6048):41–43, 1986.

[67] Kelli Hendrickson, Gabriel D Weymouth, and Dick K-P Yue. Informed component label algorithm for robust identification of connected components with volume-of-fluid method. *Computers & Fluids*, 197:104373, 2020.

[68] Marcus Herrmann. A parallel eulerian interface tracking/lagrangian point particle multi-scale coupling procedure. *Journal of computational physics*, 229(3):745–759, 2010.

[69] Winslow H Herschel and Ronald Bulkley. Konsistenzmessungen von gummi-benzollösungen. *Kolloid-Zeitschrift*, 39:291–300, 1926.

[70] Andrew J Hewitt. Droplet size and agricultural spraying, part i: Atomization, spray transport, deposition, drift, and droplet size measurement techniques. *Atomization and Sprays*, 7(3), 1997.

[71] J. O. Hinze and H. Milborn. Atomization of Liquids by Means of a Rotating Cup. *Journal of Applied Mechanics*, 17(2):145–153, 04 1950. ISSN 0021-8936.

[72] C. W. Hirt and B. D. Nichols. Volume of fluid (VOF) method for the dynamics of free boundaries. *Journal of Computational Physics*, 39(1):201–225, January 1981.

[73] Moses M. Hohman, Michael Shin, Gregory Rutledge, and Michael P. Brenner. Electrospinning and electrically forced jets. I. Stability theory. *Physics of Fluids*, 13 (8):2201–2220, 2001. ISSN 10706631.

[74] Moses M. Hohman, Michael Shin, Gregory Rutledge, and Michael P. Brenner. Electrospinning and electrically forced jets. II. Applications. *Physics of Fluids*, 13 (8):2221–2236, 2001. ISSN 10706631.

[75] Joseph Hoshen and Raoul Kopelman. Percolation and cluster distribution. i. cluster multiple labeling technique and critical concentration algorithm. *Physical Review B*, 14(8):3438, 1976.

[76] hypre. *hypre*: High performance preconditioners. `https://llnl.gov/casc/hypre`, `https://github.com/hypre-space/hypre`.

[77] Kyoung-Su Im, Ming-Chia Lai, Yi Liu, Nasy Sankagiri, Thomas Loch, and Hossein Nivi. Visualization and Measurement of Automotive Electrostatic Rotary-Bell Paint Spray Transfer Processes. *Journal of Fluids Engineering*, 123(2):237–245, 12 2000. ISSN 0098-2202.

[78] Kyoung-Su Im, Ming-Chia Lai, Sheng-Tao John Yu, and Robert R. Jr. Matheson. Simulation of Spray Transfer Processes in Electrostatic Rotary Bell Sprayer. *Journal of Fluids Engineering*, 126(3):449–456, 07 2004. ISSN 0098-2202.

[79] J.E Dendy J. Black box multigrid. *Journal of Computational Physics*, 48:366–386, 1982. ISSN 0021-9991.

[80] A Jaworek, AT Sobczyk, and A Krupa. Electrospray application to powder production and surface coating. *Journal of Aerosol Science*, 125:57–92, 2018.

[81] Bavand Keshavarz, Eric C. Houze, John R. Moore, Michael R. Koerner, and Gareth H. McKinley. Rotary atomization of newtonian and viscoelastic liquids. *Physical Review Fluids*, 5(3), 2020.

[82] Muhammad Kashif Iqbal Khan, Maarten A.I. Schutyser, Karin Schroën, and Remko Boom. The potential of electrospraying for hydrophobic film coating on foods. *Journal of Food Engineering*, 108:410–416, 2012. ISSN 0260-8774.

[83] Douglas B Kothe and William J Rider. A comparison of interface tracking methods. Technical report, Los Alamos National Lab.(LANL), Los Alamos, NM (United States), 1995.

[84] Agisilaos Kourmatzis and John S. Shrimpton. Electrohydrodynamics and charge injection atomizers: A review of the governing equations and turbulence. *Atomization and Sprays*, 19(11):1045–1063, 2009. ISSN 1044-5110.

[85] M Krafczyk, P Lehmann, O Filippova, D Hänel, and U Lantermann. Lattice boltzmann simulations of complex multiphase flows. *Multifield Problems: State of the art*, pages 50–57, 2000.

[86] Venkata Krisshna and Mark Owkes. High-fidelity simulation of a rotary bell atomizer with electrohydrodynamic effects. In *ICLASS 2021, 15th Triennial International Conference on Liquid Atomization and Spray Systems*, 2021.

[87] Venkata Krisshna, Wanjiao Liu, and Mark Owkes. High-fidelity simulations of a rotary bell atomizer with electrohydrodynamic effects. *International Journal of Multiphase Flow*, 168:104566, 2023. ISSN 0301-9322. doi: https://doi.org/10.1016/j.ijmultiphaseflow.2023.104566.

[88] Maximilian Kuhnhenn, Tórstein V. Joensen, Mads Reck, Ilia V. Roisman, and Cameron Tropea. Study of the internal flow in a rotary atomizer and its influence

on the properties of the resulting spray. *International Journal of Multiphase Flow*, 100:30–40, 2018. ISSN 0301-9322.

[89] Robert J Lang. Ultrasonic atomization of liquids. *The journal of the acoustical society of America*, 34(1):6–8, 1962.

[90] Pierre-Simon Laplace. *Mechanism of the Heavens*. Cambridge Library Collection - Physical Sciences. Cambridge University Press, 2009.

[91] AH Lefebvre, XF Wang, and CA Martin. Spray characteristics of aerated-liquid pressure atomizers. *Journal of Propulsion and Power*, 4(4):293–298, 1988.

[92] F. Lekien and J. Marsden. Tricubic interpolation in three dimensions. *International Journal for Numerical Methods in Engineering*, 63(3):455–471, 2005. ISSN 00295981.

[93] Liya Li and Masaki Sawamoto. Multi-phase model on sediment transport in sheet-flow regime under oscillatory flow. *Coastal Engineering in Japan*, 38(2):157–178, 1995.

[94] PY Liang and MD Schuman. Atomization modeling in a multiphase flow environment and comparison with experiments. In *AIAA, Fluid Dynamics, 21st Plasma Dynamics and Lasers Conference, 21st, Seattle, WA, June 18-20, 1990. 17 p.*, 1990.

[95] Bin Liu, Hengxiang Hu, Lisen Bi, and Panagiotis E Theodorakis. Analysis of the characteristics of the gas–liquid mixed artificial snow-making. *International Journal of Refrigeration*, 149:155–167, 2023.

[96] Thomas Loch, Hossein Nivi, Yi Liu, Ming-Chia Lai, and Kyoung-Su Im. An Experimental Investigation of Spray Transfer Processes in an Electrostatic Rotating Bell Applicator. In *International Body Engineering Conference & Exposition*. SAE International, sep 1998.

[97] JM López-Herrera, Stéphane Popinet, and MA2764018 Herrada. A charge-conservative approach for simulating electrohydrodynamic two-phase flows using volume-of-fluid. *Journal of Computational Physics*, 230(5):1939–1955, 2011.

[98] Wilai Luewisutthichat, Atsushi Tsutsumi, and Kunio Yoshida. Bubble characteristics in multi-phase flow systems: bubble sizes and size distributions. *Journal of chemical engineering of Japan*, 30(3):461–466, 1997.

[99] L. Ma, D. B. Ingham, M. Pourkashanian, and E. Carcadea. Review of the Computational Fluid Dynamics Modeling of Fuel Cells. *Journal of Fuel Cell Science and Technology*, 2(4):246–257, 04 2005. ISSN 1550-624X.

[100] Michael B. Mackaplow, Isidro E. Zarraga, and Jeffrey F. Morris. Rotary spray congealing of a suspension: Effect of disk speed and dispersed particle properties. *Journal of Microencapsulation*, 23(7):793–809, 2006.

[101] Ahmed Mahmoud and M. S. Youssef. Influence of spinning cup and disk atomizer configurations on droplet size and velocity characteristics. *Chemical Engineering Science*, 107:149–157, 2014. ISSN 0009-2509.

[102] A. Mark, Bjorn Andersson, S. Tafuri, K. Engstrom, H. Sorod, F. Edelvik, and J. S. Carlson. Simulation of electrostatic rotary bell spray painting in automotive paint shops. *Atomization and Sprays*, 23(1):25–45, 2013. ISSN 1044-5110.

[103] Vidar Mathiesen, Tron Solberg, Hamid Arastoopour, and Bjørn H Hjertager. Experimental and computational study of multiphase gas/particle flow in a cfb riser. *AIChE journal*, 45(12):2503–2518, 1999.

[104] James E. McCarthy and Dwight W. Senser. Specific charge measurements in electrostatic air sprays. *Particulate Science and Technology*, 23(1):21–32, 2005. ISSN 02726351.

[105] J R Melcher and G I Taylor. Electrohydrodynamics: A Review of the Role of Interfacial Shear Stresses. *Annual Review of Fluid Mechanics*, 1(1):111–146, 1969.

[106] James R Melcher. *Continuum electromechanics*, volume 2. MIT press Cambridge, MA, 1981.

[107] A. J. Mestel. Electrohydrodynamic stability of a highly viscous jet. *Journal of Fluid Mechanics*, 312:311–326, apr 1996. ISSN 00221120.

[108] Paul D Morris, Andrew Narracott, Hendrik von Tengg-Kobligk, Daniel Alejandro Silva Soto, Sarah Hsiao, Angela Lungu, Paul Evans, Neil W Bressloff, Patricia V Lawford, D Rodney Hose, et al. Computational fluid dynamics modelling in cardiovascular medicine. *Heart*, 102(1):18–28, 2016.

[109] B. Mostafaie Maynagh, B. Ghobadian, T. Tavakkoli Hashjin, and M. R. and Jahannama. Effect of electrostatic induction parameters on dropletscharging for agricultural application. *Journal of Agricultural Science and Technology*, 11(3), 2009.

[110] Igari Naoki, Iso Takuro, Nishio Yu, Izawa Seiichiro, and Fukunishi Yu. Numerical simulation of droplet-formation in rotary atomizer. *Theoretical and Applied Mechanics Letters*, 9:202–205, 2019. ISSN 2095-0349.

[111] Ghasem G Nasr, Andrew J Yule, and Lothar Bendig. *Industrial sprays and atomization: design, analysis and applications*. Springer Science & Business Media, 2002.

[112] N. K. Nayyar and G. S. Murty. The stability of a dielectric liquid jet in the presence of a longitudinal electric field. *Proceedings of the Physical Society*, 75(3):369–373, 1960. ISSN 03701328.

[113] William F Noh and Paul Woodward. Slic (simple line interface calculation). In *Proceedings of the fifth international conference on numerical methods in fluid dynamics June 28–July 2, 1976 Twente University, Enschede*, pages 330–340. Springer, 2005.

[114] Shinzi Ogasawara, Masatoshi Daikoku, Minori Shirota, Takao Inamura, Yasuhiro Saito, Kotaro Yasumura, Masakazu Shoji, Hideyuki Aoki, and Takatoshi Miura. Liquid Atomization Using a Rotary Bell Cup Atomizer. *Journal of Fluid Science and Technology*, 5:464–474, 2010.

[115] OICA. World Motor Vehicle Production - 2019 Production Statistics. Technical report, Organisation Internationale des Constructeurs d'Automobiles, 2019.

[116] Stanley Osher and Ronald P Fedkiw. *Level set methods and dynamic implicit surfaces*, volume 1. Springer New York, 2005.

[117] Stanley Osher and James A Sethian. Fronts propagating with curvature-dependent speed: Algorithms based on hamilton-jacobi formulations. *Journal of computational physics*, 79(1):12–49, 1988.

[118] Walter Oswald, Jan Lauk, Lutz Gödeke, Peter Ehrhard, and Norbert Willenbacher. Analysis of paint flow pulsations during high-speed rotary bell atomization. *Coatings*, 9(10):1–9, 2019. ISSN 20796412.

[119] Mark Owkes and Olivier Desjardins. A computational framework for conservative, three-dimensional, unsplit, geometric transport with application to the volume-of-fluid (VOF) method. *Journal of Computational Physics*, 270:587–612, 2014. ISSN 0021-9991.

[120] Mark Owkes and Olivier Desjardins. A mesh-decoupled height function method for computing interface curvature. *Journal of Computational Physics*, 281:285–300, 2015. ISSN 0021-9991.

[121] Mark Owkes and Olivier Desjardins. Consistent and conservative framework for incompressible multiphase flow simulations. In *APS Division of Fluid Dynamics Meeting Abstracts*, pages H7–007, 2015.

[122] Mark Owkes and Olivier Desjardins. A mass and momentum conserving unsplit semi-Lagrangian framework for simulating multiphase flows. *Journal of Computational Physics*, 332:21–46, 2017. ISSN 0021-9991.

[123] Mark Owkes, Eric Cauble, Jacob Senecal, and Robert A. Currie. Importance of curvature evaluation scale for predictive simulations of dynamic gas–liquid interfaces. *Journal of Computational Physics*, 365:37–55, 2018. ISSN 0021-9991.

[124] JD Oxley. Spray cooling and spray chilling for food ingredient and nutraceutical encapsulation. In *Encapsulation technologies and delivery systems for food ingredients and nutraceuticals*, pages 110–130. Elsevier, 2012.

[125] Suhas V Patankar. A numerical method for conduction in composite materials, flow in irregular geometries and conjugate heat transfer. In *International Heat Transfer Conference Digital Library*. Begel House Inc., 1978.

[126] Mohammad Reza Pendar and José Carlos Páscoa. Numerical modeling of electrostatic spray painting transfer processes in rotary bell cup for automotive painting. *International Journal of Heat and Fluid Flow*, 80:108499, 2019. ISSN 0142727X.

[127] Mohammad Reza Pendar and José Carlos Páscoa. Atomization and spray characteristics around an ERBS using various operational models and conditions: numerical investigation. *International Journal of Heat and Mass Transfer*, 161, 2020. ISSN 00179310.

[128] Mohammad-Reza Pendar and José Carlos Páscoa. Numerical analysis of charged droplets size distribution in the electrostatic coating process: Effect of different operational conditions. *Physics of Fluids*, 33(3):033317, 2021.

[129] M Pilch and CA Erdman. Use of breakup time data and velocity history data to predict the maximum size of stable fragments for acceleration-induced breakup of a liquid drop. *International journal of multiphase flow*, 13(6):741–757, 1987.

[130] Stéphane Popinet and Stéphane Zaleski. A front-tracking algorithm for accurate representation of surface tension. *International Journal for Numerical Methods in Fluids*, 30(6):775–793, 1999.

[131] Precedence Research. Automotive Paints & Coatings Market Growth, Report 2020-2027 Automotive. Technical report, Precedence Research, 2019.

[132] Andrea Prosperetti and Grétar Tryggvason. *Computational methods for multiphase flow*. Cambridge university press, 2009.

[133] Pratikkumar Raje and Naresh Chandra Murmu. A Review on Electrohydrodynamic-inkjet Printing Technology. 2014.

[134] R. Ray and P. Henshaw. Evaporation of clearcoat solvents from a rotary bell atomizer and its relationship with bell speed, flow rate, and electrostatic potential. *Journal of Coatings Technology and Research*, 15:41–49, 2018.

[135] Rolf D Reitz and Rm Diwakar. Structure of high-pressure fuel sprays. *SAE transactions*, pages 492–509, 1987.

[136] Ning Ren, A Blum, C Do, and Andre W Marshall. Atomization and dispersion measurements in fire sprinkler sprays. *Atomization and Sprays*, 19(12), 2009.

[137] Sajjad Rezayat and Mohammad Farshchi. Spray formation by a rotary atomizer operating in the coriolis-induced stream-mode injection. *Atomization and Sprays*, 29 (10):937–963, 2019.

[138] William J Rider and Douglas B Kothe. Reconstructing volume tracking. *Journal of computational physics*, 141(2):112–152, 1998.

[139] Clark Rubel and Mark Owkes. Extraction of droplet genealogies from high-fidelity atomization simulations. *Atomization and Sprays*, 29(8):709–739, 2019. ISSN 10445110.

[140] Youcef Saad and Martin H Schultz. Gmres: A generalized minimal residual algorithm for solving nonsymmetric linear systems. *SIAM Journal on scientific and statistical computing*, 7(3):856–869, 1986.

[141] Poozesh Sadegh, Akafuah Nelson, and Saito Kozo. Effects of automotive paint spray technology on the paint transfer efficiency – a review. *Proceedings of the Institution of Mechanical Engineers, Part D: Journal of Automobile Engineering*, 232(2):282–301, 2018.

[142] B. Sanderse, S.P. van der Pijl, and B. Koren. Review of computational fluid dynamics for wind turbine wake aerodynamics. *Wind Energy*, 14(7):799–819, 2011.

[143] D. A. Saville. Electrohydrodynamic Stability: Fluid Cylinders in Longitudinal Electric Fields. *Physics of Fluids*, 13(12):2987–2994, 1970.

[144] D. A. Saville. Stability of Electrically Charged Viscous Cylinders. *Physics of Fluids*, 14(6):1095–1099, 1971.

[145] D. A. Saville. Electrohydrodynamics: The Taylor-Melcher Leaky Dielectric Model. *Annual Review of Fluid Mechanics*, 29(1):27–64, 1997.

[146] Robert I. Saye, James A. Sethian, Brandon Petrouskie, Aaron Zatorsky, Xinyu Lu, and Reza Rock. Insights from high-fidelity modeling of industrial rotary bell atomization. *Proceedings of the National Academy of Sciences*, 120(4):e2216709120, 2023.

[147] Roland Schmehl, Georg Maier, and Sigmar Wittig. Cfd analysis of fuel atomization, secondary droplet breakup and spray dispersion in the premix duct of a lpp combustor. In *ICLASS 2000: 8th International Conference on Liquid Atomization and Spray Systems, Pasadena, CA, USA, 16-20 July 2000*. ILASS, 2000.

[148] S. Schmidt, O. Krüger, K. Göckeler, and C. O. Paschereit. Numerical investigation of the breakup behavior of an oscillating two-phase jet. *Physics of Fluids*, 30(7), 2018. ISSN 10897666.

[149] James Albert Sethian. *Level set methods and fast marching methods: evolving interfaces in computational geometry, fluid mechanics, computer vision, and materials science*, volume 3. Cambridge university press, 1999.

[150] C. Sharma, D. Malhotra, and A. S. Rathore. Review of computational fluid dynamics applications in biotechnology processes. *Biotechnology Progress*, 27(6):1497–1510, 2011.

[151] Patrick Sheehy and Mark Owkes. Numerical study of electric Reynolds number on electrohydrodynamic assisted atomization. *Atomization and Sprays*, 27(7):645–664, 2017. ISSN 1044-5110.

[152] Bo Shen, Qiaoyan Ye, Nico Guettler, Oliver Tiedje, and Joachim Domnick. Primary breakup of a non-Newtonian liquid using a high-speed rotary bell atomizer for spray-painting processes. *Journal of Coatings Technology and Research*, 16:1581–1596, 2019.

[153] M Shirota, Y Hatayama, T Haneda, T Inamura, M Daikoku, Y Saito, and H Aoki. Formation and breakup of ligaments from a rotary bell cup atomizer. In *12th International Conference on Liquid Atomization and Spray Systems, ICLASS 2012*, 2012.

[154] John S Shrimpton. Atomization, combustion, and control of charged hydrocarbon sprays. *Atomization and Sprays*, 11(4), 2001.

[155] John S. Shrimpton and Yossapong Laoonual. Dynamics of electrically charged transient evaporating sprays. *International Journal for Numerical Methods in Engineering*, 67 (8):1063–1081, 2006.

[156] K. Sidawi, P. Moroz, and S. Chandra. On surface area coverage by an electrostatic rotating bell atomizer. *Journal of Coatings Technology and Research*, 18:649–663, 2021.

[157] K. Sidawi, P. Moroz, and S. Chandra. Bell-cup serrations and their effect on atomization in electrostatic rotating bell atomizers. *Experiments in Fluids*, 62(8): 1–16, 2021. ISSN 14321114.

[158] S.D Sovani, P.E Sojka, and A.H Lefebvre. Effervescent atomization. *Progress in Energy and Combustion Science*, 27(4):483–521, 2001.

[159] Vedanth Srinivasan, Abraham J. Salazar, and Kozo Saito. Modeling the disintegration of modulated liquid jets using volume-of-fluid (VOF) methodology. *Applied Mathematical Modelling*, 35(8):3710–3730, 2011.

[160] Ch Stevenin, Y. Bereaux, J. Y. Charmeau, and J. Balcaen. Shaping Air Flow Characteristics of a High-Speed Rotary-Bell Sprayer for Automotive Painting Processes. *Journal of Fluids Engineering, Transactions of the ASME*, 137(11):1–8, 2015. ISSN 1528901X.

[161] Brian P. Stimpson and Charles A. Evans Jr. Electrohydrodynamic ionization mass spectrometry of biochemical materials. *Biomedical Mass Spectrometry*, 5(1):52–63, 1978.

[162] Otmar M. Stuetzer. Magnetohydrodynamics and electrohydrodynamics. *The Physics of Fluids*, 5(5):534–544, 1962.

[163] Hilding Sundqvist and George Veronis. A simple finite-difference grid with non-constant intervals. *Tellus*, 22(1):26–31, 1970. ISSN 0040-2826.

[164] Soma Tatsuya, Katayama Tomoyuki, Tanimoto Junichi, Saito Yasuhiro, Matsushita Yohsuke, Aoki Hideyuki, Nakai Daichi, Kitamura Genki, Miura Masanari, Asakawa Takukatsu, Daikoku Masatoshi, Haneda Toshiki, Hatayama Yohsuke, Shirota Minori, and Inamura Takao. Liquid film flow on a high speed rotary bell-cup atomizer. *International Journal of Multiphase Flow*, 70:96–103, 2015. ISSN 0301-9322.

[165] Geoffrey Taylor. Studies in Electrohydrodynamics. I. The Circulation Produced in a Drop by Electrical Field. *Proceedings of the Royal Society of London Series A*, 291 (1425):159–166, April 1966.

[166] Nikola Toljic, K. Adamiak, G. S.P. Castle, Hong Hsiang Kuo, and Hua Tzu Fan. Three-dimensional numerical studies on the effect of the particle charge to mass ratio distribution in the electrostatic coating process. *Journal of Electrostatics*, 69(3):189–194, 2011. ISSN 03043886.

[167] Gaurav Tomar, Daniel Gerlach, Gautam Biswas, Norbert Alleborn, Ashutosh Sharma, Franz Durst, Samuel WJ Welch, and Antonio Delgado. Two-phase electrohydrodynamic simulations using a volume-of-fluid approach. *Journal of Computational Physics*, 227(2):1267–1285, 2007.

[168] MN Topp and P Eisenklam. Industrial and medical uses of ultrasonic atomizers. *Ultrasonics*, 10(3):127–133, 1972.

[169] G Tryggvason, B Bunner, O Ebrat, and W Tauber. Computations of multiphase flows by a finite difference/front tracking method. i. multi-fluid flows. *Lecture Series-von Karman Institute For Fluid Dynamics*, pages 7–7, 1998.

[170] Grétar Tryggvason, Bernard Bunner, Asghar Esmaeeli, Damir Juric, N Al-Rawahi, W Tauber, J Han, S Nas, and Y-J Jan. A front-tracking method for the computations of multiphase flow. *Journal of computational physics*, 169(2):708–759, 2001.

[171] R.J. Turnbull. Self-acceleration of a charged jet. *IEEE Transactions on Industry Applications*, 25(4):699–704, 1989.

[172] Bret Van Poppel, Olivier Desjardins, and J. W. Daily. A ghost fluid, level set methodology for simulating multiphase electrohydrodynamic flows with application

to liquid fuel injection. *Journal of Computational Physics*, 229:7977–7996, 2010. ISSN 0021-9991.

[173] James Van Strien, Phred Petersen, Petros Lappas, Leslie Yeo, Amgad Rezk, Sara Vahaji, and Kiao Inthavong. Spray characteristics from nasal spray atomization. *Journal of Aerosol Science*, 165:106009, 2022.

[174] Valerio Viti, J. Kulkarni, and A. Watve. Computational fluid dynamics analysis of the electrostatic spray painting process with a rotating bell cup. *Atomization and Sprays*, 20(1):1–17, 2010. ISSN 1044-5110.

[175] Xin Tao Wang, Zhi Ning, and Ming Lü. Linear instability of a charged non-Newtonian liquid jet under an axial electric field. *Journal of Applied Physics*, 126(13):135301, 2019. ISSN 10897550.

[176] Jacob E. Wilson, Stephen W. Grib, Adnan Darwish Ahmad, Michael W. Renfro, Scott A. Adams, and Ahmad A. Salaimeh. Study of Near-Cup Droplet Breakup of an Automotive Electrostatic Rotary Bell (ESRB) Atomizer Using High-Speed Shadowgraph Imaging. *Coatings*, 8(5), 2018.

[177] Wolfgang Wulff. Computational methods for multiphase flow. *Multiphase Science and Technology*, 5(1-4), 1990.

[178] Bin Xia and Da-Wen Sun. Applications of computational fluid dynamics (cfd) in the food industry: a review. *Computers and Electronics in Agriculture*, 34(1):5–24, 2002. ISSN 0168-1699.

[179] T Yamamoto and HR Velkoff. Electrohydrodynamics in an electrostatic precipitator. *Journal of Fluid Mechanics*, 108:1–18, 1981.

[180] Ligong Yang. Numerical simulation of paint spray process. 2006.

[181] Chunde Yao, Zhong He, Huaqing Zhu, Yan Li, and Jianjun Li. The measurement of droplet size distributions from rotary atomizers. *Journal of agricultural engineering research*, 82(4):379–386, 2005.

[182] AJ Yule, JS Shrimpton, AP Watkins, W Balachandran, and D Hu. Electrostatically atomized hydrocarbon sprays. *Fuel*, 74(7):1094–1103, 1995.

[183] Yi Zhu, De-an Zhao, Fa-zhong Li, and De-yuan Kong. Numerical simulation of the gas flow field of electrostatic rotary-bell spray system. In *2010 3rd International Conference on Computer Science and Information Technology*, volume 2, pages 1–4. IEEE, 2010.

# APPENDIX

## A.1 Liquid Surface Profile in a Rotating Tank

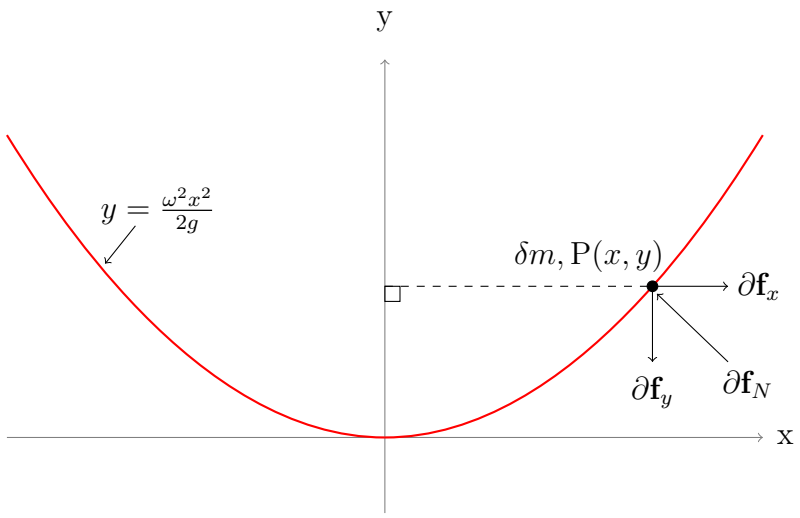



Figure A.1: Analytical solution of the liquid surface (red) in a tank rotating about the y axis with an angular velocity $\omega$ described mathematically by the function $y$

Consider a liquid mass element located at $\mathrm{P}(x, y)$ on the surface of the liquid in a tank rotating about its vertical (y) axis with an angular velocity $\omega$ (Fig. A.1). Centrifugal force, which acts in the x-direction, can be expressed as $\partial \mathbf{f}_x = \delta m \cdot \omega^2 x$. Gravity, which acts in the y-direction, can be expressed as $\partial \mathbf{f}_y = \delta m \cdot g$. $\partial \mathbf{f}_N$ represents the normal force acting perpendicular to the fluid element, which is the resultant of the vector sum of $\partial \mathbf{f}_x$ and $\partial \mathbf{f}_y$. Therefore, it can be seen that the local slope of the surface at point P is

$$\frac{\partial y}{\partial x} = \frac{\partial \mathbf{f}_y}{\partial \mathbf{f}_x} = \frac{\omega^2 x}{g} \tag{A.1}$$

On integrating, this gives

$$y = \frac{\omega^2 x^2}{2g} \tag{A.2}$$

which is the mathematical formulation of the liquid surface in a rotating tank.

## A.2 Trajectory of an Object in a Rotating Frame

Consider an object of mass $\delta m$ on a two-dimensional plane in a reference frame that is rotating counterclockwise with an angular velocity $\omega$ about an axis perpendicular to the plane. The object experiences centrifugal and Coriolis forces. Therefore, according

to Newton's Second Law,

$$\begin{aligned}\delta m\frac{\partial^2\mathbf{r}}{\partial t^2} =&\partial\mathbf{f}_{\text{centrifugal}} + \partial\mathbf{f}_{\text{Coriolis}}\\ =&\delta m(\omega\times\mathbf{r})\times\omega + 2\delta m\frac{\partial\mathbf{r}}{\partial t}\times\omega\end{aligned} \tag{A.3}$$

where $\mathbf{r}(x, y)$ is its position vector. The equation of motion reduces to

$$\frac{\partial^2\mathbf{r}}{\partial t^2} = \omega^2\mathbf{r} + 2\frac{\partial\mathbf{r}}{\partial t}\times\omega \tag{A.4}$$

whose components can be simplified as

$$\frac{\partial x^2}{\partial t^2} = \omega^2 x + 2\omega\frac{\partial y}{\partial t} \tag{A.5}$$

$$\frac{\partial y^2}{\partial t^2} = \omega^2 y - 2\omega\frac{\partial x}{\partial t}. \tag{A.6}$$

Multiplying Eq. A.6 by $i$ and adding it to Eq. A.5 gives

$$\frac{\partial x^2}{\partial t^2} + i\frac{\partial y^2}{\partial t^2} = \frac{\partial^2\mathbf{R}}{\partial t^2} = \omega^2\mathbf{R} - 2i\omega\frac{\partial\mathbf{R}}{\partial t} \tag{A.7}$$

to which the general solution is of the form

$$\mathbf{R}(t) = e^{-i\omega t}\left(C_1 + C_2 t\right). \tag{A.8}$$

Applying initial conditions of $\mathbf{r}(0) = (x_0, y_0)$ and $\frac{\partial\mathbf{r}}{\partial t}|_{t=0} = (u_0, v_0)$ as $\mathbf{R}(0) = (x_0, y_0)$ and $\frac{\partial\mathbf{R}}{\partial t}|_{t=0} = (u_0 + iv_0)$, $C_1$ and $C_2$ can be solved to give

$$\mathbf{R}(t) = e^{-i\omega t}\left[x_0 + u_0 t + i(v_0 + \omega x_0)t\right]. \tag{A.9}$$

Isolating the real and imaginary parts, the equation of instantaneous position is obtained as

$$\begin{aligned}x(t) &= x_0 - (x_0 + u_0 t)\,\cos(\omega t) + t(v_0 + x_0\omega)\,\sin(\omega t)\\ y(t) &= y_0 - (x_0 + u_0 t)\,\sin(\omega t) + t(v_0 + x_0\omega)\,\cos(\omega t).\end{aligned} \tag{A.10}$$